On the Predicted Effectiveness of Climate Change Adaptation Measures for Outdoor Thermal Comfort using CFD

By

Muhammad Zeeshan

(Registration No: 00000241332)

Supervised by:

Dr. Zaib Ali

Department of Mechanical Engineering

School of Mechanical and Manufacturing Engineering

National University of Sciences and Technology (NUST)

H-12, Islamabad 44000, Pakistan

(October 2022)

On the Predicted Effectiveness of Climate Change Adaptation Measures for Outdoor Thermal Comfort using CFD

By

Muhammad Zeeshan

(Registration No: 00000241332)

A thesis submitted to the National University of Sciences and Technology, Islamabad in partial fulfillment of the requirements for the degree of

Doctor of Philosophy in
Mechanical Engineering

Thesis Supervisor: Dr. Zaib Ali

Department of Mechanical Engineering

School of Mechanical and Manufacturing Engineering

National University of Sciences and Technology (NUST)

H-12, Islamabad 44000, Pakistan

(October 2022)

Thesis Acceptance Certificate

Certified that final copy of PhD thesis written by **Mr. Muhammad Zeeshan**, Registration No. **00000241332** of **School of Mechanical and Manufacturing Engineering (SMME)** has been vetted by undersigned, found complete in all aspects as per NUST Statutes/Regulations/PhD Policy, is free of Plagiarism, errors and mistakes and is accepted as partial fulfillment for the award of PhD Degree. It is further certified that necessary amendments as pointed out by GEC members and foreign/local evaluators of the scholar have also been incorporated in the said thesis.

Signature: _____

Name of the Supervisor: <u>Dr. Zaib Ali</u>

Date: _____

Signature (HoD):_____

 Date: _____

<u>Countersigned by</u>

Signature (Principal/Dean)_____

Date: _____

Report of Doctoral Thesis Defence-PhD7 form

Certificate of Approval

This is to certify that the research work presented in this thesis, titled **"On the Predicted Effectiveness of Climate Change Adaptation Measures for Outdoor Thermal Comfort using CFD"** was conducted by **Mr. Muhammad Zeeshan** under the supervision of **Dr. Zaib Ali**.

No part of this thesis has been submitted anywhere else for any degree. This thesis is submitted in the **School of Mechanical and Manufacturing Engineering** in partial fulfillment of the requirements for the degree of Doctor of Philosophy in the field of **Mechanical Engineering**, Department of **Mechanical Engineering, School of Mechanical and Manufacturing Engineering,** **National University of Sciences and Technology, Islamabad, Pakistan.**

Student Name: <u>Muhammad Zeeshan</u>   Signature: _____

Examination Committee:

a) External Examiner 1:   Signature: _____
Dr. Talha Irfan Khan, Assistant Professor
Institute of Space Technology (IST),
Islamabad, Pakistan

b) External Examiner 2:   Signature: _____
Dr. Saif Ullah, Associate Professor
University of Engineering and Technology,
Taxila, Islamabad, Pakistan

c) Internal Examiner: Signature: _____
Dr. Majid Ali, HoD, Associate Professor
Thermal Energy Engineering, USPCASE,
NUST, Islamabad, Pakistan

Supervisor Name: <u>Dr. Zaib Ali</u>   Signature: _____

Name of Dean/HOD: Dr. Emad ud Din   Signature: _____

Authors Declaration

I, Muhammad Zeeshan hereby state that my PhD thesis, titled "On the Predicted Effectiveness of Climate Change Adaptation Measures for Outdoor Thermal Comfort using CFD" is my own work and has not been submitted previously by me for taking any degree from "National University of Sciences and Technology (NUST)" or anywhere else in the country/worldwide.

At any time if my statement is found to be incorrect even after my graduation, the university has the right to withdraw my PhD degree.

Name of the Student: Muhammad Zeeshan

Signature: _____

Date: _____

Plagiarism Undertaking

I, Muhammad Zeeshan, solemnly declare that research work presented in the PhD thesis, titled "On the Predicted Effectiveness of Climate Change Adaptation Measures for Outdoor Thermal Comfort using CFD" is solely my research work with no significant contribution from any other person. Small contributions/help wherever taken have been duly acknowledged and that complete thesis has been written by me.

I understand the zero tolerance policy of the HEC and National University of Sciences and Technology (NUST) towards plagiarism. Therefore, I as an Author of the above titled thesis declare that no portion of my thesis has been plagiarized and any material used as reference is properly referred / cited.

I undertake that if I found guilty of any formal plagiarism in the above titled thesis even after award of PhD Degree, the University reserves the right to withdraw/revoke my PhD Degree and that HEC and the University has the right to publish my name on the HEC / University website on which the names of the students are placed who submitted plagiarized thesis.

Student /Author Signature: _____

Name: _____Muhammad Zeeshan_____

Acknowledgement

Muhammad Zeeshan,

October 2022

Abstract

The urban heat island (UHI) phenomenon has become a major concern for urban sustainability in the wake of global warming and rapid urbanization. This has resulted in increased heat stress and worsened outdoor thermal comfort in urban microclimates. Vegetation, water bodies, and cool materials are one of the most effective strategies to alleviate the adverse effects of rising outdoor temperatures. Computational fluid dynamics (CFD) has established itself as a valuable tool to model various urban physics phenomena and develop climate change and UHI mitigation and adaptation strategies. However, there exist certain numerical modeling aspects which require further insight. In this work, CFD simulations have been performed to analyze the effect of more realistic vegetation modeling parameters. The vegetation modeling parameters include the actual form drag coefficient and the variable tree transpiration rate. In addition to that, thermal comfort effectiveness of different tree species with its various morphological characteristics, cool materials' albedo, and water bodies have also been studied in individual and in combination for a real urban area. The morphological characteristics/parameters include trunk height (HT), crown diameter (CW), crown height (CH), and leaf area density (LAD). The wind flow and heat transfer phenomena are simulated using the unsteady Reynolds-averaged Navier–Stokes (URANS) approach.

The simulations were performed with proposed adaptation measures for a real urban area having hot-humid climatic conditions under heat wave conditions. It has been found that for the studied climatic conditions, the consideration of more realistic values of these parameters can yield significant variation in the determination of cooling potential and flow characteristics of applied vegetation. Of all the morphological characteristics, LAD, crown height, and trunk height are found to be

most influential in providing thermal comfort. Water bodies promotes improved thermal conditions and urban ventilation in spatial direction. Water and vegetation interventions promote the cooling effect by resulting in low ambient air and surface temperature i.e. 0.9 °C and 3.5 °C; 0.3 °C and 3 °C respectively when compared with reference case. Cool materials, when applied simultaneously on both buildings and ground, generate a more pronounced cooling effect than when applied separately on ground or the buildings as it results in a large reduction of air and surface temperature i.e., of 2 °C and 6 °C respectively. Furthermore, the impact becomes more significant for collective application of these adaptation measures. Cool materials when combined with vegetation and water results in large reduction i.e. 2.2 °C and 1.9 °C in air temperature; and 5.9 °C and 9 °C in surface temperature was observed respectively compared to the reference case. For air flow velocity, it is highest for combined cool materials with water with peak effect at the time of highest solar irradiance. The analysis shows that the proposed interventions can effectively decrease surrounding temperature and promote airflow; thereby promoting thermal comfort conditions.

List of Publications

1.   Zeeshan, M., Ali, Z., & Ud Din, E. (2022). Thermal performance prediction of street trees inside isolated open spaces–evaluations from real scale retrofitting project. Journal of Building Performance Simulation, 1-17.

https://doi.org/10.1080/23744731.2022.2040322

2.   Zeeshan, M., & Ali, Z. (2022). Heat Stress Mitigation in urban streets having Hot-Humid climatic conditions: Strategies and performance results from a real scale retrofitting project. Science and Technology for the Built Environment, 1-23.

https://doi.org/10.1080/23744731.2022.2040322

3.   Zeeshan, M., & Ali, Z. (2022). The Potential of Cool Materials towards Improving Thermal Comfort Conditions inside Real-urban Hot-humid Microclimate. Environment and Urbanization ASIA, 09754253221083206.

https://doi.org/10.1177/09754253221083206

4.   Zeeshan, M, Ali, Z, Sajid, M, Ali, M, & Usman, M. Modeling the cooling effectiveness of street trees with actual canopy drag and real transpiration rate under representative climatic conditions, Journal of Building Performance Simulation.

 https://doi.org/10.1080/19401493.2022.2080865

5.   Zeeshan, M, Ali, Z, & Usman, M. Urban Sustainability, in Context of continuous Climate Change, through use of street Water Bodies: Assessment/Feasibility under hot-humid climatic conditions; Journal of water and climate change (Under Review).

Table of Contents

1 Contents

List of Figures

List of Table

List of Abbreviations

Abbreviation	Description
CFD	Computational Fluid Dynamics
HT	Trunk Height
CW	Crown Width
CH	Crown Height
LAD	Leaf Area Density
UHI	Urban Heat Island
URANS	Unsteady Reynold Average Naiver Stokes
UN	United Nation
IPCC	Intergovernmental Panel on Climate Change
RCP	Representative Concentration Pathways
UNFCC	UN Framework Convention on Climate Change
SVF	Sky View Fraction
Ta	Air Temperature
ABL	Atmospheric Boundary Layer
EBM	Energy Building Models
LES	Large Eddy Simulation
DNS	Direct Numerical Simulation
GDP	Gross Domestic Product
PMD	Pakistan Meteorological Department
RTE	Radiation Transport Equation
DO	Discrete Ordinate
CPU	Central Processing Unit
PISO	Pressure Implicit with Splitting Operators
UDF	User Defined Functions
PET	Physiological Equivalent Temperature
RH	Relative Humidity
UTCI	Universal Thermal Climate Index
TMRT	Mean Radiation Temperature

MODIS	Moderate-resolution Imaging Spectroradiometer
TC	Tree Case
CVCP	Constant Volumetric Cooling Power
TDC	Tuned Drag Coefficient
TRCP	Transpiration Rated Cooling Power
AFDC	Actual Form Drag Coefficient
RC	Reference Case
CMG	Cool Material on Ground Only
CMB	Cool Material on Building Only
CM	Cool Material
CMCV	Cool Material with Vegetation
CMCW	Cool Material with Water Bodies
CMVW	Cool Material with Vegetation and Water Bodies
UV	Ultra-Violet
NIR	Near Infra-Red

Chapter-1

Introduction

In this section, the necessity of this research in the context of climate change and rapid urbanization is described. This is then followed by proposed research methodology for getting the desired research aim.

1.1 Urbanization

The continued increase in urbanization in recent years is attributed to all said societal challenges. According to the United Nations (UN) report based on the perspective of global urbanization, a rising trend has been expected in the proportion of world population toward living in urban areas in the course of the 21st Century [1]. In 1950, only 30% of the population was residing in urban areas. This percentage has increased to 57 % in 2022. This would probably reach 70 % by 2050 (Figure 1. 1). The forecasted urban growth in Asia and Africa would acclimate to 90 % in the next three decades with the largest expansion in the developing regions in the world [2]. Moreover, the regions across the globe are also going to urbanize further in coming decades owing to a sharp rise in city developments and transformation of rural areas into urban settlement in pursuit of getting better living standards and conditions [2].
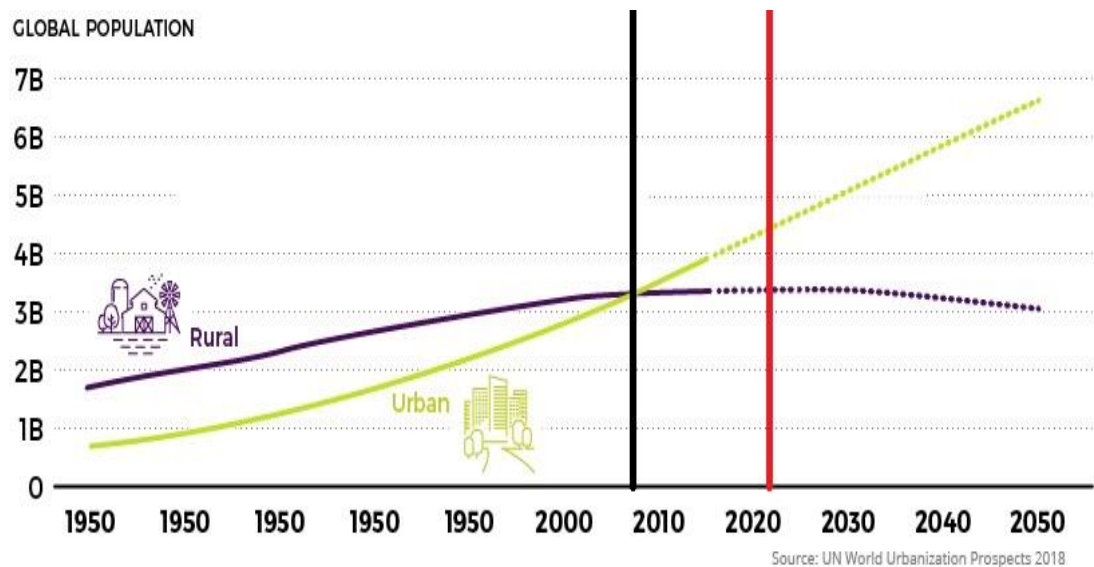
Figure 1. 1: Urbanization Growth, Modified from [3].

Recently developing "Sustainable cities and communities" is one of the fundamental goals of the UN toward sustainable development along with the goal of climate action [4]. Toward aiming at UN goal, research for sustainable settlements and urban physics is increasingly gaining importance and will increase further in coming years.

1.2 Urban Heat Island

To accommodate the uncontrolled population growth during the last half-century, urban areas experienced rapid expansion due to the enhanced use of artificial surfaces in impairment of natural ecosystem [5,6]. Moreover, the urban environment is also getting deteriorated due to high air pollution, low evapotranspiration owing to low levels of green infrastructure and shading, high heat capacity of surface materials, low shortwave reflectivity (characterized by low albedo of building materials), poor ventilation, and anthropogenic heat gains [7,8]. These cause additional trapping of longwave solar radiation inside urban streets as they prevent dispersion of absorbed energy during the daytime; thus affecting the surface energy balance of local urban microclimates. As a result, urban areas experience larger ambient air temperatures compared to the surroundings, giving rise to the urban heat island (UHI) phenomenon [9].
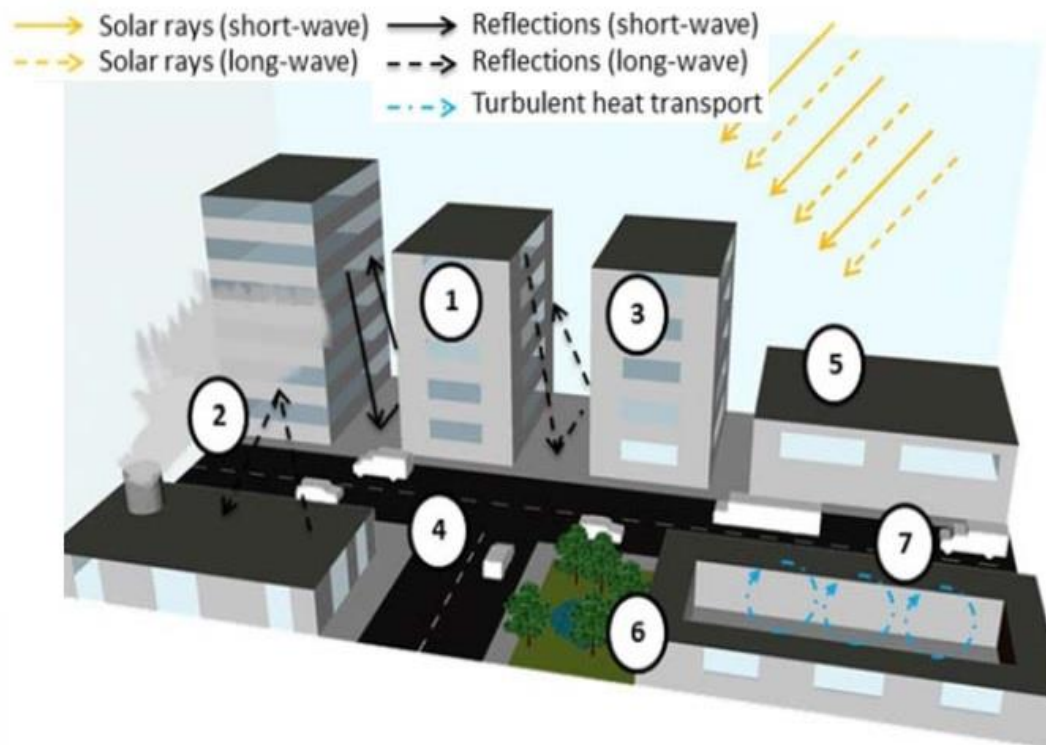
Figure 1.2: UHI in Urban Microclimate [10].

Oke [9] identified the following causes of UHI: During the summers, temperatures in urban centers are 1-6 ºC higher than in the surrounding rural areas [6]. Rural settings tend to shift towards better environments as compared to urban settings where urban canyons, anthropogenic causes, minimal shades of trees, minimal vegetation and plantation, a smaller number of water bodies, and low albedo materials pavements are common as given in Figure 1.2 and Table 1.1 [7]. Oke showed that temperature is somehow related to the density of the urban center, and the temperature increases as the size of the city increases, which creates a severe UHI effect [8]. He also summarized the causes of urban heat island effect which are shown in Table 1.1 [9]. Urban heat island effect is due to less turbulent transport in the narrow streets which eventually affects pedestrian's comfort. It is advised to plant trees and do vegetation on the pavements for the thermal comfort of the pedestrians [9].

The major factors affecting the UHI and causing the thermal anomaly inside urban areas are formulated in Table 1.1. In 1982, Oke summarized the causes of the Urban Heat Island effect which are tabulated below:

Table 1.1: Causes of UHI.

Sr. No	Energy Balance Term responsible for the thermal anomaly	Negative Effects due to energy balance changes
1	Enlarged short wave radiation absorption	Compound reflection and amplified area of surface
2	Increased exposure to sky long-wave radiation	Larger absorption/re-emission
3	Reduced loss of long-wave radiation	Decreased sky-view-factor
4	Anthro-pogenic heat-Source	Building/traffic harms
5	Improved storage of sensible-heat	Intestified thermal-admittance
6	Reduced evapo-transpiration	Enlarged water-proofing
7	Lessened windy transport	Declined wind-speed

1.3 Climate Change and Heat Waves

In recent years, there are two major terms that we have been listening to global warming and climate change. Climate change is attributed to the long-term temperature shifts and changing weather patterns, either because of natural changes in the solar cycles

or due to anthropogenic activities. Temperature anomaly is on the rise as human activity is being increased in this era as shown in Figure 1.2. According to recent assessment reports of Intergovernmental Panel on Climate Change (IPCC) and UN [2,11], human activities are causing an increase in greenhouse gas emissions, owing to a large increase in economic and population growth. This rise in gas emission is further going to exacerbate global warming and climate change, resulting in an increasingly severe and irreversible impact on people and the natural ecosystem. Furthermore, this emission is expected to increase further by 20 % in 2040 (Figure 1.3). This overheating of urban areas further aggravates the effects of climate change which is producing an increase in extreme heatwaves intensity and frequency; sustained thermal discomfort and heat stress; and increased heat-related mortality and morbidity in urban dwellers [12,13]. Moreover, future climate projections suggest further extensive growth rates in urbanization [3] and persistent (scenario-dependent) global warming [11]. This will result in a sharp rise in thermal stress intensity (which has already affected pedestrian thermal comfort in a hot-humid microclimate) that would be difficult to control [14,15]. There is a growing concern for the people, infrastructure, and ecology of microclimates that are at extreme risk from the harmful effects of climate change. It is proved that the developed areas exert negative influence over their microclimate and the thermal discomfort for pedestrians is increased [1].
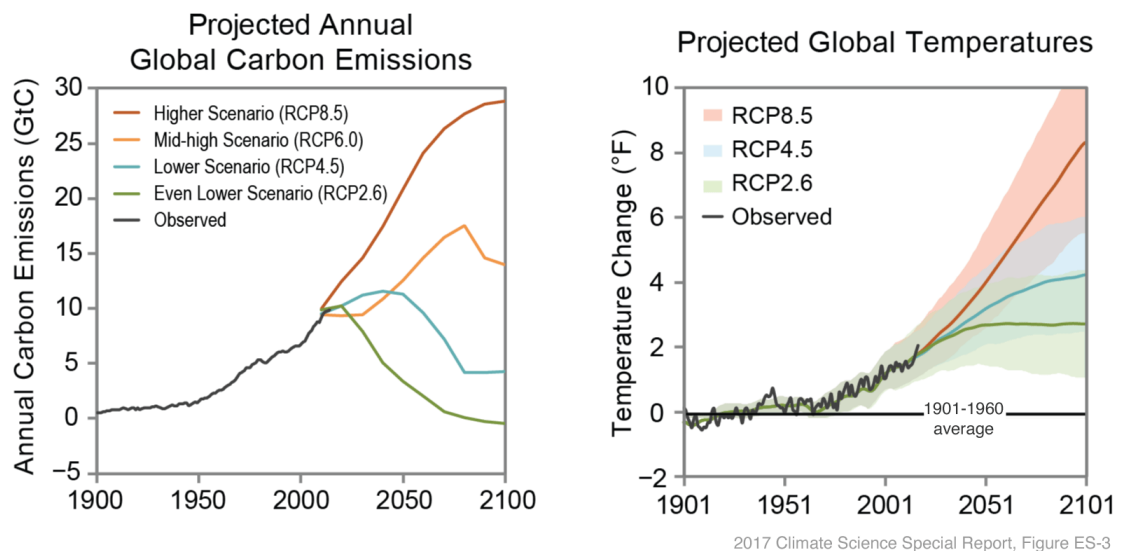
Figure 1.3: Future Projections of Emission and Temperature [4,11].

There has been a significant increase in apparent temperature in Pakistan in recent years due to a large increase in urban density and population growth, the main cause

for a sharp rise in the heat index in Pakistan (Figure 1.4) [16,17] which has impacted the economy and livelihood of people. UHI is the sole reason for June 2015 heatwave in Karachi. According to Pakistan Meteorology Department, the heatwave (June 2015) lasted for five consecutive days with a temperature anomaly of 5.3 ºC to 11 ºC on a diurnal basis. This also impacts the urban energy systems as higher temperature intensifies the electricity demand especially at peak times up to 0.45-12.3% in terms of air-conditioning usage and building quality [18]. It is expected that UHI would afford to cause a severe health risk for the susceptible part of the population in this megacity in wake of increasing global warming and poor coping strategies. Hence, there exists a pronounced interest and serious endeavors toward the adaptation of the cities to the changing climate and the rising outdoor temperatures.
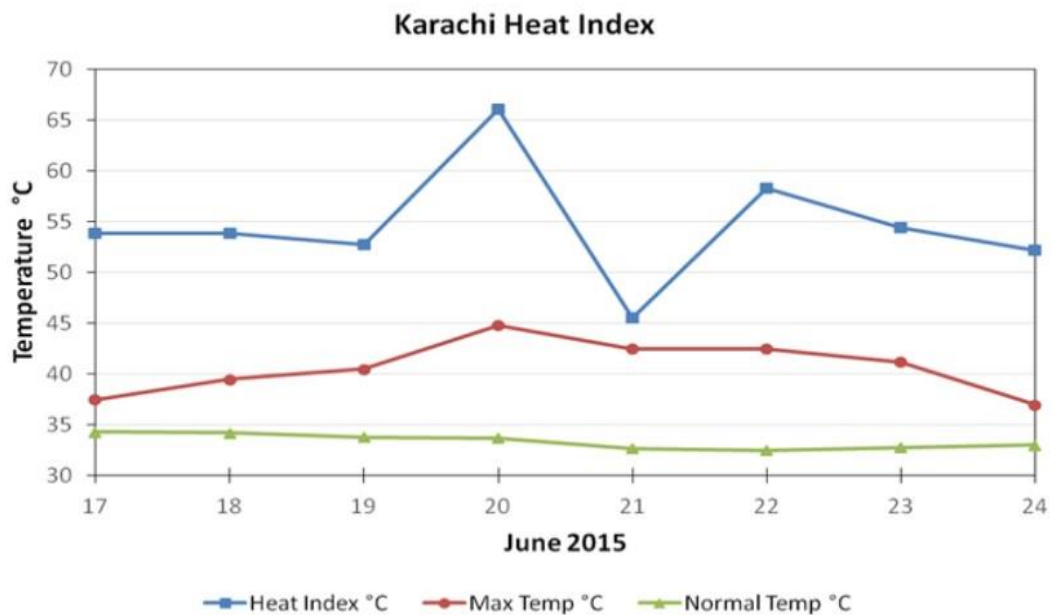
Figure 1.4: Heat Index for June 2015.

1.4 Climate-Resilient Urban Microclimate with Adaptation Measures

Mitigation is a phenomenon by which climate change is restrained through sustained lessoning of greenhouse gas emissions and this reduction must be substantial. However, despite achieving complete mitigation, climate change would persist and continue to grow in proportion with the presence of available gas emissions in the atmosphere. This gives forth to climate change adaptation phenomenon, which refers to "*forecasting the harmful effects of climate change and then compelling the suitable*

actions to lesson or eliminate the adverse effects caused by climate change and/or exploiting the positive opportunities arises by such actions" [19].

The persistent climate change and rapid urbanization demands a dire need for adaptation of urban areas to safeguard the pedestrian against the adverse effects of climate change and global warming. As per UN Framework Convention on Climate Change (UNFCC) report , the evaluation of the effectiveness of adaptation measures toward reducing the negative effects of climate change to acceptable levels is done by performing comparative studies with and without adaptation measures [20,21]. This is usually done by comparing the temperatures of the base case and worst-case scenario incorporated with adaptation measures.

1.5   Research Gap/Problem Statement

The previous studies performed with vegetation only consider steady/constant volumetric cooling power of vegetation which is a function of LAD only. However, the vegetation effect by simulating its transpiration rate by thoroughly considering air humidity produced by transpiration in a high spatial real urban microclimate has not yet been studied. Moreover, vegetation in form of the cuboid porous zone was only modeled with a tuned value of drag coefficient and fixed LAD was only employed thus missing the modeling of canopy shape more realistically and green volume expansion. Furthermore, the studies involving tree species were focused on species performance in the open environment, parks, and generic symmetric canyons having fixed SVF rather than real canyons having variable SVF across asymmetrical canyons and miscellaneous streets orientations as such strongly affect solar access due to shadowing effects and trapping of long wave radiations, increases of humidity and variable wind flow patterns. In addition, the previous studies assess the thermal performance of measures at the pedestrian's height during hot summer conditions [22,23]. However, their effectiveness at different vertical heights in hot humid climates has not been extensively studied which is important for comprehensive analysis of their potential in the surroundings [24]. Moreover, under hot humid conditions, the mitigation potentials are further reduced due to impaired transpiration. Moreover, evaluation of the mitigation effectiveness of these measures' parameters toward modulating outdoor urban environment in isolated open spaces (*i.e.* streets), has not been fully performed. This is due to its exciting nature as there exist huge

temporal variability and spatial heterogeneity in boundary/microclimatic conditions [5]. Moreover, advection and urban geometry have considerable effects on the mitigation effectiveness (temperature reduction) at such locations. This attributes to hot air channeling through these street aisles/canyons from surrounding areas owing to the difference in temperature and pressure [25].

1.6   Techniques for Analyzing Urban Microclimate

The techniques used to analyze the urban microclimate include field measurements, laboratory experiments, and numerical simulations. Various measurement studies have investigated the cooling/ mitigation potential of adaptation measures by studying their important parameters   [26,27]. Despite diverse experimental studies, this approach in a real urban environment can be challenging due to some constraints such as the data gathering at few discrete points, less control over changing weather conditions, and entails high cost [28]. Alternatively, the use of numerical methods such as computational fluid dynamics (CFD) has been gaining popularity [28] as these offer coupled simulations of wind flow, heat, and moisture transfer [29] with controlled boundary conditions. Moreover, the results can be analyzed at all points in the computational domain simultaneously [30]. However, the reliability of the CFD result can be a concern that can be tackled by performing proper validation and verification such as comparison with the experimental data [28]. Since computational fluid dynamics (CFD) has established itself as a valuable tool to model various urban physics phenomena and develop climate change and UHI mitigation/adaptation strategies, attracting researchers and analyst to adopt this method.

1.7   Research Aim

The current study research is aimed at following:

- Developing new parameterization in respect of aerodynamic and thermal effects of urban vegetation.
- Investigating the cooling effectiveness of tree vegetation with implementation of these newly developed parameterization i.e., Actual form drag coefficient and variable tree transpiration rate.
- Quantifying the potential of outdoor climate change adaptation measures toward improving thermal comfort conditions in isolated streets under representative climatic conditions

1.8   Research Objective and Methodology

The methodology adopted for investigating the cooling potential of climate change adaptation measures is illustrated as:
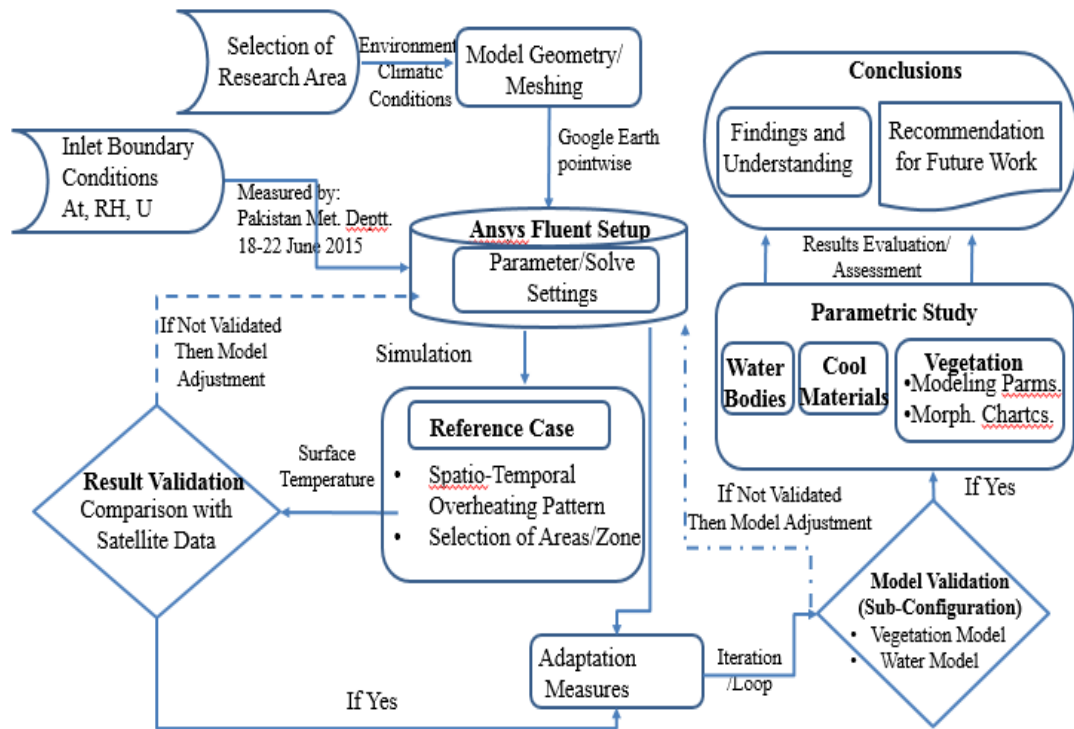
Figure 1.5: Methodology Framework.

The thesis has the objective of developing, validating, and simulating the newly developed parameterization in CFD models for appraising the performance of vegetation with its actual form drag coefficient and transpiration rate in the real urban hot humid microclimate (Figure 1.5). Moreover, the study has further various sub-objectives which are described below:

- To investigate the thermal profile of studied urban area under extreme heat wave conditions and validation of these simulation temperatures with satellite measurements for heatwave period (18-23 June 2015).
- To Identify and prioritize the locations/evaluation zones for incorporation of adaptation measures
- Modeling and verification of CFD models for vegetation and water bodies using a sub-configuration method on a generic model rather than complete urban microclimate. These sub-configured validations carry high fidelity experimental or wind tunnel measurements, approved by an authorized

agencies and organization. The computation settings and parameters used for sub-configuration validation are then incorporated into actual cases having a complex configuration to get realistic results.

- Evaluating the cooling potential of vegetation toward improving thermal comfort inside a real build environment by modeling transpiration rate of vegetation by thoroughly considering air humidity produced by vegetation

- Investigation of the effect of different morphological characteristics of tree species on the improvement of thermal comfort conditions for selection of right species at right place.

- Assessing the cooling potential of cool materials and water bodies toward reducing the UHI intensity inside the studies microclimate

- A thorough investigation of cooling performance of proposed adaptation measures in combination in hot-humid urban microclimate

1.9   Thesis Outline

This thesis is composed of six chapters (Chapter 2-6). The thesis outline is given below:

Chapter 2 consists of a literature review of previous studies carried out on mitigation measures and CFD basics along with numerical settings. The literature review is based upon a review study of journal and conference papers, having focus on the analysis of urban microclimate. Numerical settings and parameters are extracted from this analysis after the development of the CFD model. Moreover, the problem statement along with the research gap is identified.

Chapter 3 presents the methodology adapted to carry out simulations. Moreover, it contains mathematical model for proposed adaptation measures.

Chapter 4 investigates the effect of the street trees in the representative hot-humid urban microclimate by simulating the cooling effect of vegetation by predicting its thermal performance inside real urban hot-humid climates. This is then followed by a performance evaluation of street trees with their various modeling and morphological parameters. The intensity of cooling effect (temperature reduction) convected from the street trees is the main aim of this research after comparing the aforesaid cases.

Chapters 5 gives the performance evaluation of water bodies toward improving thermal comfort conditions inside a real urban hot-humid climate by calculating the

heat flux with respect to the inlet meteorological conditions after evaluating the performance of the developed approach.

Chapter 6 assesses the thermal performance of cool materials (in single/combination) toward improving the thermal comfort of real urban climates.

The conclusions and future recommendations are outlined in Chapter 7.

Chapter - 2

Literature Review

In this chapter, the literature review, entailing the major previous studies, is carried out in the context of urban microclimate. These studies mentioned in this section are solely related to proposed adaptation measures i.e. vegetation, water bodies and cool materials.

2.1 Introduction

To accommodate the uncontrolled population growth during the last half-century, urban areas experienced rapid expansion due to the enhanced use of artificial surfaces in impairment of natural ecosystem [5,6]. Moreover, the urban environment is also getting deteriorated due to high air pollution, low evapotranspiration owing to low levels of green infrastructure and shading, high heat capacity of surface materials, low shortwave reflectivity (characterized by low albedo of building materials), poor ventilation, and anthropogenic heat gains [7,8]. These-all cause additional trapping of longwave solar radiation inside urban streets as they prevent dispersion of absorbed energy during the daytime; thus affecting the surface energy balance of local urban microclimates. As a result, urban areas experience larger ambient air temperatures compared to the surroundings, giving rise to the urban heat island (UHI) phenomenon [9]. This overheating of urban areas further aggravates the effects of climate change which is producing an increase in extreme heatwaves intensity and frequency; sustained thermal discomfort and heat stress; and increased heat-related mortality and morbidity in urban dwellers [12,13]. Moreover, future climate projections suggest further extensive growth rates in urbanization [3] and persistent (scenario-dependent) global warming [11]. This will result in a sharp rise in thermal stress intensity (which has already affected pedestrian thermal comfort in a hot-humid microclimate) that would be impossible to control [14,15].

There has been a significant increase in apparent temperature in Pakistan in recent years due to a large increase in urban density and population growth, the main cause for a sharp rise in the heat index in Pakistan [16,17] which has impacted the economy

and livelihood of people. This also impacts the urban energy systems as higher temperature intensifies the electricity demand especially at peak times up to 0.45-12.3% in terms of air-conditioning usage and building quality [18]. Urban heat mitigation also helps in savings of energy [8,31] as the average total energy load of representative buildings in heating/cooling applications has increased by more than 12% during the last half-century [18]. Hence, there exists a pronounced interest and serious endeavors toward the adaptation of the cities to the changing climate and the rising outdoor temperatures.

In this regard, several adaptation measures have been examined in the past [32–34]. Among the adaptation measures include vegetation [9,35]; water bodies [22]; urban geometry [36,37]; surface materials [38,39] and anthropogenic heat source [33]. The proposed mitigation or adaption measures change the biophysical and aerodynamics attributes of urban surfaces and areas, thus playing a vital role in altering the energy flux between ground and upper surfaces. This redistribution in energy patterns through city-scale convection helps in reducing the UHI intensity [40,41] thus affecting the downscale urban physics [42,43].

Vegetation (street trees) is one of the most commonly used heat stress mitigation strategies as it provides various microclimatic benefits by alleviating solar penetration, creating shade, and through evapotranspiration [32,44–46]. Various studies have investigated the cooling effect and aerodynamics characteristics of trees. In these studies, the influence of a variety of parameters including tree layout, shape, height, species, wake effect has been examined [32,45,47–52]. In these studies, a temperature reduction of maximum of 1.4 °C was found. Almost all these studies were performed by considering steady/constant volumetric cooling power of vegetation which is a function of LAD only. However, Toparlar et al. [47] studied the impact of urban parks by modeling the unsteady performance of vegetation through incorporating temperature-dependent cooling power as a function of leaf transpiration and observed more realistic results. Similarly, Zhang et al. studied the vegetation effect by simulating its transpiration rate by thoroughly considering air humidity produced by transpiration in one apartment complex in South Korea [45]. They proposed implementing this in a high spatial real urban microclimate. Thus, an understanding of more realistic modeling of this parameter in hot-humid urban microclimates is yet quite limited.

In CFD simulations, vegetation is usually modeled as a cuboid porous zone due to the challenging nature of discretizing real complex-shaped tree canopies. This simplified canopy domain results in an inflated volume of the tree structure. This creates a modeling disparity leading to the overestimation of the effective drag coefficient in such CFD simulations. Zeng et al. [53] demonstrated that experimentally measured effective drag coefficients are usually three to four times greater than the CFD calculated drag coefficients (usually around 0.65). In addition, in urban microclimates having a common wind speed range, effective drag coefficients are also expected to be larger than the tuned drag coefficients, introducing a large error in simulating drag effects. Based on these scenarios and experimental results, a drag correction factor coupled with variable LAD along the tree height is required to be employed to model the tree canopy shape more realistically and to consider green volume expansion/inflation. Until now, the drag effect of canopies on the spatially-averaged flow has been the most focused around buildings, which in combination with spatially variable LAD alters the local flow [54]. The actual drag characterized by effective drag coefficient multiplied with spatial variability of LAD (actual form drag coefficient) has not been investigated yet in modeling the cooling effect of vegetation in real urban microclimates; thus its impacts on vegetation source term magnitudes through loss of kinetic energy, wake production, and dissipation rate due to canopy drag has so-far not studied.

In reality, the microclimatic benefits of vegetation such as heat penetration, shade, and transpiration rate are strongly affected by tree species and their morphological characteristics i.e. leaf density, tree height, crown diameter, tree architecture, and proximity to each other [55] alongside its size and shape. Besides these factors, environmental variables (CO_2 concentration, temperature, and soil wetness) and tree physical configuration (leaf shape, color, tree/trunk height, and branch architecture) also affect the vegetation effectiveness [56,57]. This poses a dire need for undertaking research to move out of the generalized tree to site-specific analysis toward thermal stress mitigation and decision-making. Various studies in this regard, both numerical and experimental, have been performed in recent years to observe the impact of species characteristics on thermal comfort. Morakinyo et.al. Studied the impact of various tree species and their configurational parameters on thermal comfort in simple canyons and found a varying cooling effect ranging from 0.3 °C to 1 °C and 0 °C to 2

°C in the daytime and nighttime temperature. They also deduced that leaf area density (LAD), tree crown, and trunk height are the most influential parameters [6]. Saeid Teshnehdel et al. studied the effect of different tree species and tree vegetation cover on microclimate parameters and found a significant reduction of 0.29 °C and 20.04 °C in air temperature (Ta) and mean radiation temperature (Tmrt) with an increase in coverage fraction during summer [58]. The varying cooling potential by species owes its effectiveness to their morphological and structural variability which has not been extensively studied.

Water bodies, in the context of sustainable urban development, have shown significant potential towards alleviating the UHI due to its high thermal and evaporative cooling capacity. Various types of techniques including measurement studies and numerical simulations have investigated the cooling effect and aerodynamics characteristics of water bodies including rivers and ponds [59,60]. Hathway and Sharples documented an average temperature decrease of 1 °C in Sheffield, the UK due to the existence of the river during hot weather conditions [61]. Chen et al. analyzed the cooling effect of a small lake in China using remote sensing techniques and observed an air temperature reduction of 1.3 °C [62]. Another study [63] proposed using water bodies in small patches rather than a large ones to achieve better thermal surroundings owing to greater heat exchange capacity. Furthermore, they found a greater potential with the use of large water volume as wider surface area amplifies the evaporative effect. Syaffli et al. performed an experimental study and found the same observations [64]. Yang et al. performed a numerical study and observed that the presence of a water body greatly affects the temperature of the surrounding, a reduction of up to 2 °C and promoting the wind flow [22]. Runhao et al. conducted a numerical study [65] and found that the landscape descriptors (water body's area, geometry, location, and the surrounding built-up proportions), significantly impact the microclimate surrounding the water bodies. Another numerical study demonstrated a decrease of 2 °C with the use of water at pedestrian height in real urban microclimate [66]. In addition to temperature decrease, water bodies also cause the flow velocity to increase [22]. On the flip side, it results in increased localized humidity, which makes achieving thermal comfort conditions very difficult in hot-humid urban areas as its mitigation potential/effectiveness weakens due to impaired transpiration.

In promoting pedestrian comfort and improving the quality of the outdoor thermal environment, cool/reflective materials have revealed considerable cooling and mitigation potential. This measure has also been widely investigated as they are simple to implement in terms of technology to new and existing buildings, easy to maintain, and has a low cost. Various studies including field experiments [24,67] and CFD studies [23,68,69] have been performed to investigate the thermal performance of cool/reflective materials and other measures. The reason for using the CFD method is its effectiveness in analyzing urban thermal microclimate [47,66]. Georgiakis et al. investigated the effect of cool coatings in their study using the CFD approach and found a decrease in air temperature of up to 1 °C inside a canyon [70]. Sen et al. performed a pavement-canyon CFD model and found a temperature decrease of 0.8 °C to 1 °C with a reflective coating on building and wall and roof, 0.2 to 0.4 °C with reflective pavement, 0.4 - 0.8 °C with reflective roof and walls [71].

No doubt, cool materials have been proved very effective in providing pedestrian thermal comfort through mitigation of urban heat, but It also may sometimes lead to an increased ambient air temperature as a result of trapping of increased solar reflections inside the high dense urban canyons [72]. Moreover, it also affects the pedestrian's radiative exchange with its immediate surrounding (not the scope of this study). This requires an effective and feasible solution for reducing the ambient temperature by counterbalancing the increased reflected solar radiation resulting from the use of high albedos and decreased wind speed due to sharp growth in urbanization. This is accomplished through combining cool materials with other strategies i.e. integrating highly reflective/cool materials with street trees and/or blue landscape in the urban environment owing to their increased mitigation potential in terms of enhanced evaporation by water and tree foliage.

Almost all of the previous studies were focused on species performance in an open environment, parks, and generic symmetric canyons having fixed SVF rather than real canyons having variable SVF across asymmetrical canyons and miscellaneous streets orientations as such strongly affects solar access due to shadowing effects and trapping of long wave radiations, increases of humidity and variable wind flow patterns. Moreover, these studies assess the thermal performance of measures at the pedestrian's height during hot summer conditions [22,23]. However, their effectiveness at different vertical heights in hot humid climates has not been

extensively studied which is important for comprehensive analysis of their potential in the surroundings [24]. Moreover, under hot humid conditions, the mitigation potentials are further reduced due to impaired transpiration. Furthermore, the comparative analysis of results from simulations based on realistic case studies can provide a better understanding of the real contribution and potential limitations of each species and each measure to the overall thermal profile of a place [73]. Thus, a detailed study regarding the evaluation of different tree species and measures in hot humid climates is essential. Moreover, evaluation of the mitigation effectiveness of these measures' parameters toward modulating outdoor urban environment in isolated open spaces (*i.e.* streets), has not been fully performed. This is due to its exciting nature as there exist huge temporal variability and spatial heterogeneity in boundary/microclimatic conditions [5]. Moreover, advection and urban geometry have considerable effects on the mitigation effectiveness (temperature reduction) at such locations. This attributes to hot air channeling through these street aisles/canyons from surrounding areas owing to the difference in temperature and pressure [25].

Chapter-3

Numerical Methods

This section outlines all the details needed to carry out CFD simulations. This includes computation parameters, mesh development, boundary conditions, proposed interventions, and description of case studies. Moreover, necessary numerical settings and important terms/phenomena are discussed in this section

3.1   Theoretical Background

3.1.1   Urban Physics

It deals with the science involved in physical processes of urban microclimate and associated heat and mass transfer phenomenon and their interaction with surrounding elements i.e., flora, fauna, materials, humans, etc. With respect to the urban population, urban physics is aimed at providing a healthy and comfortable surrounding environment, both indoor and outdoor, against climatic and economic constraints. In the wake of rapid urbanization, urban physics has expanded a lot as its understanding is put a significant role in addressing the prevailing societal challenges (e.g., urbanization, health, energy, climate change, etc.) resulting from this rapid urbanization. It has now become the main area of focus of scientists and urban planners.

3.1.2   Urban Scales and Governing Models

Urban microclimates are usually recognized with temporal and spatial scales. Urban physics mainly emphasized a nether most segment of atmospheric boundary layers (ABL) when it concerns vertical spatial scales. This ABL has huge spatial and temporal variability ranging from a few meters to hundreds of kilometers. This height variability depends on the nature of stratification conditions. In case of stable conditions, its height is up to certain meters which prevails to several kilometers upon shadowing of strong unstable conditions of stratifications. The importance of ABL is due to its attribute of turbulence feature. This turbulence in the lower part of ABL has two fundamental differences when compared with studies with wind tunnel testing. First, coupling of turbulences caused by thermal convection and wind shear, and second its direct contact with mean flow caused by earth rotation. Similarly, urban

physics mainly deals with meteorological microscale when it has concerns in horizontal spatial scales covering up to 2 Km regions and mainly involves heat and mass transfer phenomenon. This spatial scale has Lagrangian Rossby numbers greater than 200 or 2 km and less [74]. A pictorial representation of horizontal and vertical spatial scales is depicted in Figure 3.1. A phenomenon like Cyclone and Tropical Cyclone is usually studied at synoptic/macroscale level while thunderstorms, precipitation, cloud formation, and atmospheric radiative characteristics are dealt in the mesoscale level.
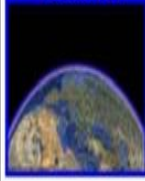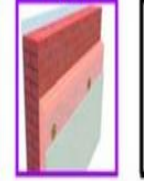
Spatial scale	Global	Mesoscale	Microscale	Building	Component	Material/Human
Distance	< 6500 km	< 200 km	< 2 km	< 100 m	< 10 m	< 1 m
Model cat.	NWP	NWP / MMM	CFD	CFD / BES	BC-HAM	MSM / HTM

Figure 3.1: Urban Scales Urban Scales [75].

A wide range of approaches is being used nowadays to study urban microscales. According to Mirzai [76,77], there are two major categories; observational approaches and numerical approaches. The main advantage of the numerical approach is to undertake a comparative analysis based on different scenarios and results provision for any flow variable in the computational domain. The energy balance method and computational fluid dynamics are two major approaches that fall in the category of the numerical method. CFD has the advantage of resolving flow field at a finer scale and performing simulation with coupled velocity and temperature field when compared with EBM, but it also requires detailed knowledge of boundary conditions for all variables, highly discretized urban geometry, and reasonable computational power.

Moreover, the problems at meteorological microscales are usually tackled with one of the following three methods (Table 3.1).

Table 3.1:Comparison of approaches.

Field Measurements	Wind Tunnel	Numerical Modelling
Capture the real complexity of the problem under study	Can imitate real complexity of problems to certain levels	Have the capability of providing detailed information on the relevant flow variables across the complete domain
Have poor control over boundary conditions because of inherent variable meteorological conditions	Possess a large degree of control over the boundary/test conditions	Can controlled condition in a better way without compromising similarity constraints
Not suitable for design evaluation owing to cost, no. of iterations	Can be used in the evaluation of the design stage	Well adaptable for design evaluation at an earlier stage
Perform only point measurements	Can perform measurements at certain points only	The resulting data have larger resolutions owing to measure whole domain
Intermediate cost	Entails high cost comparatively	Low cost
No similarity constraints as perform experiments on the true object	Required adherence to similarity criteria when testing at a reduced scale	Depending on the model scale, similarity constraints of certain boundary conditions
Provide most accurate results as compared to rest of techniques	Accurate upon control of boundary conditions	Accuracy of CFD is an important matter of concern thus requires validation against experimental results

The main models used in this spatial scale are terms as CFD models which used boundary condition data from mesoscale. In microscale, the thermal, wake, and large-scale turbulence is explicitly modeled while some part of turbulence is parameterized. This parametrized turbulence part is strongly a function of the CFD approach such as steady or unsteady Reynolds Averaged Navier Stokes (RANS/URANS), large eddy simulation (LES), and hybrid URANS/LES. Keeping in view the pros and cons of

each approach, the appropriateness determination of one approach is not straightforward.

3.2   Turbulence Modeling Approaches

In solving all types of flow problems, no single turbulence model is declared superior or universal. This is because of certain factors involved in the selection of the turbulence model. These factors are flow physics, the presence of established practices for problems, the accuracy level required, the available computational resources, and available time for conducting simulation. Thus, these factors should be considered before making an auspicious model choice for the application.

There are three types of approaches used to model turbulence:

DNS (Direct Numerical Simulation) - This solves time-dependent equations for turbulence with no approximation and resolves all scales both in time and space. It requires a fine grid and smaller steps thus requiring a high computational cost.

RANS (Reynolds Averaged Navier Stokes) - This is the most economic and widely used approach for modeling real urban flows. This reduces the resolution requirement to several orders as the equations are time or ensemble averaged. The detail lost or compromised during the averaging process is again fed into the governing equations to achieve the required level of accuracy. A typical example of such a model is k-epsilon and *k-w* models along with their modifications. These models simplify the problem to solutions of two additional transport equations and employ turbulent viscosity for computing the Reynolds stress. Reynold stress model is another example of RANS which solve six independent Reynold stress equation along with the E or W equation.

SRS-LES (Large Eddy Simulation) - This is based on the numerical resolution of the large turbulence scales and the modeling of small scales. The industrial problems having fluctuating flow physics or free shear flows are usually solved with this approach. In this approach, time dependent equations are filtered over the grid sizes of the computational cells to remove very fine time and length scales thus reducing the information which is fed back into the turbulence model. This is comparatively more expansive than RANS. Captures the largely separated and unsteady flow regions such as behind the blunt bodies. Comparison is given in Table 3.2.

Table 3.2:RANS vs LES - Possibilities and Limitations [75,78].

RANS	URANS	LES	HYBRID LES/URANS
Navier stokes' equation is time averaged. Model all scales of turbulence	Navier stokes equation is ensemble-averaged, thus including partial derivative in equation Requires high spatial resolution	NS equations are filtered in space i.e., eliminating small turbulent eddies only. Model small scale motion of the flow while solving large scale motions. Thus, reducing error introduced by turbulent modeling	Employs URANS in the near-wall region and LES in the rest of domain as near walls small turbulent eddies resolving with LES becomes expensive
Resolve only mean flow structures	Simulates only the turbulence statistics despite turbulence itself	Able to resolve turbulence at a large scale	Resolve turbulence at large scale in far region and model in near wall region
Most appropriate for steady flows	Most appropriate option when the unsteadiness is pronounced and deterministic	Appropriate when (approach flow) ABL has high turbulence e.g., anisotropy of turbulent scalar fluxes	Appropriate when (approach flow) ABL has high turbulence, For high Reynolds number flows
Relatively inferior in physical modeling	Relatively inferior in physical modeling	Superior performance owing to resolving a huge part of unsteady turbulence	Superior Performance
Results in comparatively low data outputs	Simulates temporal changes in flow fields	Results in greater data outputs since the boundary conditions at the inlet are resolved both in time and space	Results in greater data outputs
Requires relatively low computational resources	Requires relatively low computational resources	Requires high computational resources/cost	Requires moderate computational resources/cost
Can model nearly all urban physics phenomena with sufficient success	Adapted for practical applications	Not used so frequently owing to lack of its quality assessment in practical applications and best practice guidelines	Ideal for all industrial applications

3.3 RANS Equations

It provides an economical approach to solving complex industrial flows. It models turbulence as fluctuations in steady, average flow fields. Since these fluctuations cover a wide fetch of length and time scales, making exact solution indispensable as result in exceeding computational demands than the available source carrying scaled mesh.

Flow is generally of two types which are laminar and turbulent. Laminar flows usually require steady treatment while turbulent flows are modeled with transient treatment. The urban flows are generally turbulent so it will be the main focus of our study. The turbulent flow within the urban region is modeled with RANS.

$$\frac{\partial \rho}{\partial t} + \frac{\partial (\rho u_i)}{\partial x_i} = 0 \qquad (3.1)$$

$$\frac{\partial (\rho u_i)}{\partial t} + \frac{\partial (\rho u_i u_j)}{\partial x_j} = -\frac{\partial p}{\partial x_i} + \frac{\partial}{\partial x_j}\left[v\left\{\frac{\partial (u_i)}{\partial x_j} + \frac{\partial (u_j)}{\partial x_i} - \frac{2}{3}\delta_{ij}\frac{\partial (u_i)}{\partial x_i}\right\}\right] + \frac{\partial}{\partial x_j}\left(-\rho\overline{u_i u_j}\right) \quad (3.2)$$

3.4 Flow Physics and Appropriate Governing Equations

The selection of basic equations describing flow physics greatly impacts the modeling uncertainties and errors. The very first step is to access the nature/type of treatment required for the application. The second step is to determine the feasibility of solving the relevant equations with respect to a particular type of flow keeping in view the computational resources as it has the largest impact on the modeling error and uncertainties. Based on this assessment, the decision is made whether to use the governing equations in their original form or require simplification. The airflow model is described by the following equations.

3.4.1 Continuity Equation

The fluid transfer while conserving mass is represented by the continuity equation. This equation also provides useful information about the behavior of fluids while moving into the conduits and is mathematically described as

$$\frac{\partial \rho}{\partial t} + \frac{\partial \overline{u_i}}{\partial x_i} = 0 \qquad (3.3)$$

Where

$$\overline{u_i} \text{ cartesian component of the velocity vector } \frac{m}{s1}$$

3.4.2 Momentum Equation

As per Newton's second law, the change in momentum due to change in velocity is mathematically represented by

$$\frac{\partial \bar{u_i}}{\partial t} + \bar{u_j}\frac{\partial \bar{u_i}}{\partial x_j} = -\frac{1}{\rho}\frac{\partial \bar{p}}{\partial x_i} + \frac{\partial}{\partial x_j}\left[(v + v_t)\left(\frac{\partial \bar{u_i}}{\partial x_j} + \frac{\partial \bar{u_j}}{\partial x_i}\right)\right] + \delta_{i3g}\beta(\bar{T} - T_a) - \frac{2}{3}\frac{\partial k}{\partial x_i} + \frac{1}{\rho_a}S_{u_i}$$

$$(3.4)$$

Where

g is the gravity acceleration and S_{u_i} momentum local source terms

3.4.2.1 Boussinesq's Approximation

This is the simplest approach for solving the turbulent stresses as in eq 2 and assumes that shear stresses vary linearly with mean strain rate (velocity gradients) and isotropic turbulent viscosity. For in-compressible RANS flow, it is mathematically described as

$$-\rho u_i' u_j' = u_t \left(\frac{\partial u_i}{\partial x_j} + \frac{\partial u_j}{\partial x_i}\right) - \frac{2}{3}\rho k \delta_{ij} \quad (3.5)$$

δ_{ij} is the Kronecker delta.

$$\delta_{ij} = \{0 \quad if \ i \neq j\}$$

$$\{ 1 \quad if \ i = j \}$$

$$u_t = \rho C_\mu \frac{k^2}{\varepsilon}$$

3.4.3 Energy Equation

The energy equation is based on first law of thermodynamics. For moving fluid, the rate of change of energy inside fluid element is equal to net flux of heat into element and rate of work done on element due to body and surface forces. Mathematically, 3 D unsteady conservation equation of energy is described as:

$$\frac{\partial \bar{T}}{\partial t} + \bar{u_j}\frac{\partial \bar{T}}{\partial x_j} = \frac{\partial}{\partial x_J}\left[(D_T + D_{Tt})\frac{\partial \bar{T}}{\partial x_j}\right] + \frac{1}{\rho_a c_p}S_T \qquad (3.6)$$

Where

S_T $heat\ local\ source\ terms$ and D_T $thermal\ diffusivity$

3.4.4   Conservation of Humidity Equation

For flow involving humidity, a species conservation equation based on conservation of moisture is solved. The humidity equation is represented as

$$\frac{\partial \bar{q}}{\partial t} + \bar{u}_j \frac{\partial \bar{q}}{\partial x_j} = \frac{\partial}{\partial x_J}\left[(D_q + D_{qt})\frac{\partial \bar{q}}{\partial x_j}\right] + \frac{1}{\rho_a} S_q \qquad (3.7)$$

Where

D_q mass diffusivity and ρ is the density $kg/m3$

3.4.5   Turbulent Energy Equation

For flow involving turbulence, additional transport equations of turbulent kinetic energy and dissipation rate is solved in addition to continuity and momentum equations and are given below:

$$\frac{\partial \bar{k}}{\partial t} + \bar{u}_j \frac{\partial \bar{k}}{\partial x_j} = \frac{\partial}{\partial x_J}\left[\left(v + \frac{v_t}{\sigma_k}\right)\frac{\partial k}{\partial x_j}\right] + P_k + G_k - \varepsilon + \frac{1}{\rho_a} S_k \qquad (3.8)$$

Where S_k models the generation of turbulence kinetic energy due to mean velocity gradient.

3.4.6   Energy Dissipation Equation

$$\frac{\partial \bar{\varepsilon}}{\partial t} + \bar{u}_j \frac{\partial \bar{\varepsilon}}{\partial x_j} = \frac{\partial}{\partial x_J}\left(\left(v + \frac{v_t}{\sigma_\varepsilon}\right)\frac{\partial \varepsilon}{\partial x_j}\right) + C_{1\varepsilon}\frac{\varepsilon}{k}(P_k + G_k) - C_{1\varepsilon}\frac{\varepsilon^2}{k} + \frac{1}{\rho_a}S_\varepsilon \qquad (3.9)$$

Where

ε $e$missivity of external surface and α dissipation rate of turbulent kinetic energy . Where S_ε models the generation of turbulence.

$$P_k = \frac{v_t}{2}\left(\frac{\partial u_i}{\partial x_j} + \frac{\partial u_j}{\partial x_i}\right)^2$$

$$G_k = -\frac{v_t}{c_p}g\beta\frac{\partial T}{\partial x_j}\delta_{i3}$$

β thermal expansion coefficient $k - 1$

$$v_t = C_u\frac{k^2}{\varepsilon}$$

Where v_t is turbulent viscosity.

3.4.7 Modeling of Turbulence

Two types of techniques are used to model turbulence in urban physics: first-order closure scheme and second-order closure scheme [78]. The former scheme employed Boussinesq's eddy viscosity. This is most adapted to simulate urban physics. The latter works on modeling Reynolds stress. Our main concern is associated with the former technique i.e., first-order closure scheme. This employs two equations which are k-$e$psilon or k-w. These two-equation models are most widely used in industrial applications [78]. k- epsilon is stable and numerical robust, but k-w is more accurate in resolving boundary layer behaviors as refined near-wall mesh and for adverse pressure gradients application. This study employs the k - $epsilon$ model owing to their wider application in engineering applications with the economy, robustness, and sufficient level of accuracy. On the flip side, these models are highly insensitive to adverse pressure gradients and boundary layer separation.

To model turbulence, the standard κ-ε model is being employed as it is the most economical in computation (space and time) even though it overestimates the transverse mixing. The basic equation for this model is given below:

$$\frac{\partial(\rho k)}{\partial t} + \frac{\partial(\rho u_i k)}{\partial x_i} = \frac{\partial}{\partial x_j}\left[\left(v + \frac{v_t}{\sigma_k}\right)\frac{\partial k}{\partial x_j}\right] + (G_k) + G_b + S_k - \rho\varepsilon - Y_M \quad (3.10)$$

$$\frac{\partial(\rho\varepsilon)}{\partial t} + \frac{\partial(\rho u_i\varepsilon)}{\partial x_i} = \frac{\partial}{\partial x_j}\left[\left(v + \frac{v_t}{\sigma_\varepsilon}\right)\frac{\partial\varepsilon}{\partial x_j}\right] + C_{1\varepsilon}\frac{\varepsilon}{k}[(G_k) + C_{3\varepsilon}G_b] + S_\varepsilon - \rho C_{2\varepsilon}\frac{\varepsilon 2}{k} \quad (3.11)$$

Where $C_{1\varepsilon} = 1.44$, $C_{2\varepsilon} = 1.92$, $C_v = .09$, $\sigma_k = 1.0$, $\sigma_E = 1.3$

Keeping in view the cons of the standard K-ε model, the Realizable K-ε model is being used as it accurately predicts spreading rates of jets (planer and round) and provide superior performance for wider flows involving separation and layers with an adverse pressure gradient, etc.; and is mathematically described below:

$$\frac{\partial(\rho k)}{\partial t} + \frac{\partial(\rho u_i k)}{\partial x_i} = \frac{\partial}{\partial x_j}\left[\left(v + \frac{v_t}{\sigma_k}\right)\frac{\partial k}{\partial x_j}\right] + (G_k) + G_b + S_k - \rho\varepsilon - Y_M \quad (3.12)$$

$$\frac{\partial(\rho\varepsilon)}{\partial t} + \frac{\partial(\rho u_i\varepsilon)}{\partial x_i} = \frac{\partial}{\partial x_j}\left[\left(v + \frac{v_t}{\sigma_\varepsilon}\right)\frac{\partial\varepsilon}{\partial x_j}\right] + \rho C_1 S\varepsilon - -\rho C_2\frac{\varepsilon 2}{(k+\sqrt{V\varepsilon})} + C_{1\varepsilon}\frac{\varepsilon}{k}C_{3\varepsilon}G_b + S_\varepsilon$$

$$(3.13)$$

$$\text{Where } C_1 = \max[0.43, \frac{\text{n}}{\text{n}+5},]$$

$$\text{n} = Sk/\varepsilon$$

$$S = \sqrt{2S_{ij}S_{ij}}$$

$$v_t = \rho C_v \frac{k2}{\varepsilon}$$

$$C_v = \frac{1}{A_0 + A_s \frac{kU*}{\varepsilon}}$$

$$U*= \sqrt{2S_{ij}S_{ij} + \overline{\Omega_{ij}\Omega_{ij}}}$$

$$\overline{\Omega_{ij}} = \Omega_{ij} - 2\varepsilon_{ijk}A\mathrm{w}_k$$

$$A_s = \sqrt{6.\,Cos\,\phi},\ A_0 = 4.04,\quad \phi = \tfrac{1}{3}Cos^{-1}(\sqrt{6W})$$

$$W = S_{ij}S_{jk}S_{ik}/S^{-3},\ S^{-3} = \sqrt{S_{ij}S_{ij}}\,,\ S_{ij} = \tfrac{1}{2}(\frac{\partial(u_i)}{\partial x_j} + \frac{\partial(u_j)}{\partial x_i})$$

Where $C_1 = 1.44$, $C_2 = 1.9$, $\sigma_k = 1.0$, $\sigma_E=1.2$

$$\frac{\partial(\rho u_i)}{\partial t} + \frac{\partial(\rho u_i u_j)}{\partial x_j} = -\frac{\partial p}{\partial x_i} + \frac{\partial}{\partial x_j}[v\{\frac{\partial(u_i)}{\partial x_j} + \frac{\partial(u_j)}{\partial x_i}\frac{\partial}{\partial x_j}\left[(v + v_t)\left(\frac{\partial \overline{u_i}}{\partial x_j} + \frac{\partial \overline{u_j}}{\partial x_i}\right)\right] +$$

$$\delta_{i3g}\beta(\overline{T} - T_a) - \frac{2}{3}\frac{\partial k}{\partial x_i} + \frac{1}{\rho_a}S_{u_i} \quad (3.14)$$

3.5   Mathematical Modeling

3.5.1   Modeling the Effects of Vegetation

Following source/sink terms (equations $4.1 - 4.3$) are added to the transport equations of momentum, turbulence kinetic energy, and turbulence dissipation rate respectively to account for vegetation effects on airflow as provided by authors [79–81]:

$$S_{U_i} = -\rho c_{d,cfd}(LAD)U_i U \qquad\qquad (3.15)$$

$$S_k = \rho c_{d,cfd}(LAD)(\beta_P U^3 - \beta_d UK) \qquad (3.16)$$

$$S_\varepsilon = \rho c_{d,cfd}(LAD)\tfrac{\varepsilon}{K}(C_{\varepsilon4}\beta_P U^3 - C_{\varepsilon5}\beta_d UK) \quad (3.17)$$

Where ρ, U denote the air density and velocity magnitude respectively. β_d and β_p are the coefficients having a value of 5.0 and up to 1 respectively. U_i and K refer to the velocity in I direction and turbulence kinetic energy while $C_{\varepsilon4}$ and $C_{\varepsilon5}$ are empirical coefficients, and their value is 0.9. C_d is the coefficient of drag of the tree canopy and its tuned value adapted by authors [32,47]. LAD is the leaf area density value and its

value is 3.0 and is taken from [82] for common tree species named Guaiacum Offinate, Azadirachta Indica, and Peltophorium Paterocarum present in the studied microclimate. Another tree named Bauhinia Blakeana is explored for its high LAD i.e., 4.41 m^2/m^2 (with its spatial variability 0, 0.17, 0.30, 0.52, 0.87, 1.27, 1.28, 0.03, 0 respectively along its height from 1 to 9 m.

Table 3.3: Canopy characteristics.

Parameter	1	2	3
Canopy			
Shape	Spherical	Paraboid	Cone
F value	0.52	0.79	0.29

Thus to model the tree canopy shape more realistically, a drag correction factor coupled with variable LAD along the tree height is employed [53] and is defined as

$$C_{d,cfd} = F.C_{d,exp} \qquad (3.18)$$

Where F, is the corrective factor. For paraboid-shaped, cone-shaped, and spherical-shaped canopy trees, the values as per reference [53] are tabulated in Table 3.3.

3.5.2 Transpiration Heat Absorption and Water Release of Vegetation

As noted, transpiration heat absorption and water release of vegetation are normally modeled simplistically by heat convection or via porous zones. In this work, the energy source term is incorporated in the porous zone which is well-validated [32,47] and is given as

$$P_c = C_P m' \Delta T \frac{1}{V} \qquad (3.19)$$

Where P_c is the volumetric cooling power, C_P is the specific heat capacity of air; m' is the mass flow rate; ΔT is the temperature change of porous zone, and V is the volume of the vegetation.

In addition to the energy source term, the species transport model is used to model transpirational water release in the canopy area by incorporating a water source term into the humidity equation to reflect the humidity increase by vegetation [74]. The water source for simulating the transpiration heat release is

$$S_w = R_w \ LAD \qquad (3.20)$$

Where S_w is the H₂O (vapor) source and R_w the water release rate (g/m². d). The average transpiration rate of medium-class trees is in the range of R_w=810 gm^{-2}.d^{-1} [83]. In practical situations, this transpiration rate varies with leaf temperature in addition to certain other parameters as reported by Mo et al. in which the SPSS analysis results showed that the heat correlation coefficient between leaf temperature and plant transpiration rate is 0.9 and the corresponding regression equation is

$$Y = -2.226 + 0.108TL \qquad (3.21)$$

Here Y is the transpiration rate (mmol·m^{-2}·s^{-1}) and TL is the leaf temperature in °C which is the same as the canopy cell temperature. Therefore, equation (3.21) is applied to obtain more reasonable results of temperature as it governs both energy and H₂O source. Hence R_w is replaced with Y in equation 3.20. This novel approach to vegetation modeling which considers aerodynamic, thermal, and humidity effect is applied by incorporating user-defined functions (UDFs).

The same source terms (Equations (3.15)–(3.17)) were used in the previous studies to model the effect of vegetation on flow (e.g., [32]. In the study by [32], the vegetation model using these terms for the flow properties was validated with the measurement data from [84]. The cooling effect of the vegetation was validated with another set of measurement data from an earlier study [85] considering steady-state simulations. In this study, the unsteady behavior of vegetative cooling has been considered as a time-dependent volumetric cooling power (Pc) (W/m^3) has been assigned to the computational cells belonging to the tree crowns and is as follow:

$$ET_{eq,h} = R_h / \lambda \rho \qquad (3.22)$$

$$P_c = ETP \rho \lambda_{wh} LAD \qquad (3.23)$$

$$ETP = (0.0252T_i - 0.078)ET_{eq,h} \qquad (3.24)$$

Where $ET_{eq,h}$ (m/h) is the equivalent hourly evapotranspiration, Rh (MJ/m^2/h1) is the incoming hourly solar radiation per unit area, λ is the latent heat of vaporization, ρ is the density of water. ETP is the potential evapotranspiration (m/h), T_i is the temperature at hour t, λ_{wh} (Wh/kg) is the latent heat of vaporization in 'Watt hour' terms.

$$\alpha_{shaded} = \alpha_{open}(1 - SF) \qquad (3.25)$$

α_{shaded} is the solar absorptivity of the ground surface below trees, α_{open} is the solar absorptivity of the ground surface if not covered with trees. SF is the shading factor, with an average value of 0.88 [86]. As from the mathematical relation, SF determines the amount of solar radiation absorbed/reflected by the tree, and (1-SF) denotes the amount of radiation transmitted through tree foliage.

3.5.3 Modeling the Effects of Water Bodies

The governing equations for various heat transfer processes that involve heat exchange through water evaporation are given as follows:

The radiation equation in two vectors r, s can be viewed as a field.

$$\nabla \cdot (I_\lambda(\vec{r}.\vec{s})\vec{s}) + (\alpha_\lambda + \sigma_s)I_\lambda(\vec{r}.\vec{s}) = \alpha_\lambda n^2 I_{b\lambda} + \frac{\alpha_s}{4\pi}\int_0^{4\pi} I_\lambda(\vec{r}.\vec{s})\phi\left(\vec{s}.\vec{s'}\right)d\Omega' \qquad (3.26)$$

Where, $\vec{r}$, $(\vec{s})'$, $\vec{s}$ are the radius, scattering, and steering vector; σ_s, α_λ, n^2 are the scattering, absorption, and refraction coefficients, m^{-1}. σ, T, I_λ, $I_{b\lambda} = \sigma.T^4/\pi$ is the Stefan-Boltzmann constant in W/ (m^2.K^4), local temperature in °C, radiation intensity in W/m^2, and black body radiance in Planck function, K^4 respectively. ϕ and Ω are the phase function and solid angle in radiation.

The process for heat exchange through the water bodies involves three phenomena which are heat transfer through radiation, convection, and evaporation to the surrounding air. The total heat exchange ϕ_n (W/m^2) on the water surface can be expressed as follow:

$$\varphi_n = \varphi_s + \varphi_a - \varphi_b - \varphi_e - \varphi_c \qquad (3.27)$$

Where φ_s, φ_b, φ_e, φ_c and φ_a refers to solar shortwave radiation absorbed by water surface, water upward longwave radiation, evaporative heat dissipation, the convection heats, and incoming longwave radiations in W/m^2 respectively. Mathematically, these quantities can be described by the following equations:

$$\varphi_s = I(1 - \gamma) \qquad (3.28)$$

$$\varphi_a = 1(1 - {}^{Y}{}_a)\varepsilon_{ac}\sigma(273 + t_w) \qquad (3.29)$$

$$\varphi_b = \varepsilon_w\sigma(273 + t_a) \qquad (3.30)$$

$$\varphi_e = f(w_z)(e_a - e_w) \qquad (3.31)$$

$$\varphi_e = 0.47f(w_z)(t_a - t_w) \qquad (3.32)$$

Where, I is the averaged solar radiation available at the studied location, computed using radiation equations and is 164.6 W/m². ^{Y}, $^{Y}{}_a$, ε_{ac} refers to the reflectivity of water to solar shortwave radiation, to the atmospheric longwave radiation, and the atmosphere. The respective values of these are 0.1, 0.03, and 0.97. t_a, t_w and W_z denotes the air temperature at the height of 2 m above the water surface, water temperature, and wind velocity at the reference height and is expressed in °C and m/s. $f(w_z) = 9.2 + 0.46Wz^2$ e_a and e_w are the air saturated vapor pressure and evaporation pressure of air near water, expressed in mmHg. The resulting heat flux calculated from Equations 3.27-3.32 is implemented as UDF across the water zone.

3.5.4 Surface Energy Balance

Cool materials are characterized by their high reflectivity to solar radiation and their increased emission rate. These are implemented from a design or retrofitting point of view since these may influence the urban climate and city thermal performance. According to Oke [9], the surface energy balance equation is

$$Q* + Q_F = Q_H + Q_E + \Delta Q_S \qquad (3.33)$$

Where Q^*, Q_F, Q_H, Q_E and ΔQ_S refers to net all wave radiation flux density, anthropogenic heat flux density due to combustion, turbulent flux densities of sensible and latent heat, and net heat storage. The net all wave radiation flux density is expressed as follow:

$$Q* = R_{SWi} - R_{SWo} + R_{LWi} - R_{LWo} \qquad (3.34)$$

Where R_{SWi} is the incident short wave radiation, R_{SWo} is the upward short wave radiation and is equal to $= \alpha R_{SWi}$ with α the albedo coefficient indicating the reflection of incoming radiation and is the ratio of radiosity to irradiance and R_{LWo} is the upward longwave radiation and is computed from $R_{LWo} = \varepsilon.\sigma.T_o^4$ with ε as surface thermal emissivity.

σ the Stephen-Boltsman constant whose value is $5.67*10^{-8}$ W/ (m².K⁴) and T_o the surface skin temperature and R_{LWi} is the incident of longwave radiation.

3.5.5 Estimation of Energy Savings

Total diurnal saving of energy by street trees ($\Delta Q_{h,t}$) is calculated from mean cumulative 3D temperature reduction (cooling effect/heat reduction=$\Delta T_{h,t}$) for a daytime period over a certain vertical height and is given by

$$\Delta Q_{h,t} = cm\Delta T_{h,t} \quad (3.35)$$

$$\Delta T_{h,t} = \int_{t_1}^{t_2} \int_0^h (G(h,t) - R(h,t)).dh.dt \quad (3.36)$$

$$m = \rho.s$$

Where ρ,s $c,m,$ $t1,$ and $t2$ are the air density, size of green coverage, specific heat capacity, the mass of air, the start time of day, and the end time of day respectively. $G(h,t)$ and $R(h,t)$ is the average temperature at reference height during daytime with street trees and without street trees. h is the reference height which is taken as 20 m. It is selected as being greater than the tallest tree in the domain having a stable temperature gradient. It is not fixed as it is selected at the mean building height in some studies [87] or pedestrian height [88].

3.5.6 Apparent Temperature

To demonstrate the accurate and effective cooling impact of vegetation, a simple bioclimatic index named apparent temperature was used. This index represents actual thermal comfort conditions as it is also a function of vapor pressure, relative humidity, velocity, and air temperature [89]. Mathematically this is defined as:

$$T_A = T_a + 0.348(VP) - 0.7U + 0.70(\frac{Q}{V+10}) - 4.25 \quad (3.37)$$

$$VP = \frac{RH}{100}6.105exp^{(17.27 \times T_a//(237.7+T_a))} \quad (3.38)$$

Where T_A and T_a are apparent temperature and dry bulb temperature in °C, VP is the vapor pressure, U is the wind velocity and RH represents the relative humidity. Q is the net radiation absorbed per unit area of the body surface in W/m^2

The index has already been adopted by Mo et al. 2018 [83] to show the vegetation effectiveness toward thermal comfort improvement. Since the FLUENT model cannot give information of globe and/or mean radiation temperatures which are used to compute all comprehensive bioclimatic thermal comfort indexes such as PET and UTCI, the reason for using a simple bioclimatic index named apparent temperature.

3.6   Numerical Setting

Unsteady Reynolds Averaged Navier Stokes equations (URANS) with the "realizable *k*-epsilon" turbulence model [90] was adopted to solve the governing equations of flow variables. The simulations have been performed using Ansys FLUENT 16.2 [78]. This solver is used as a widely validated CFD tool and its application for evaluation of mitigation effectiveness of different measures in local microclimate in a three-dimensional environment with reasonable accuracy [32,47]. Simulations have been carried out according to the best practice guidelines for urban flow CFD simulations [91,92].
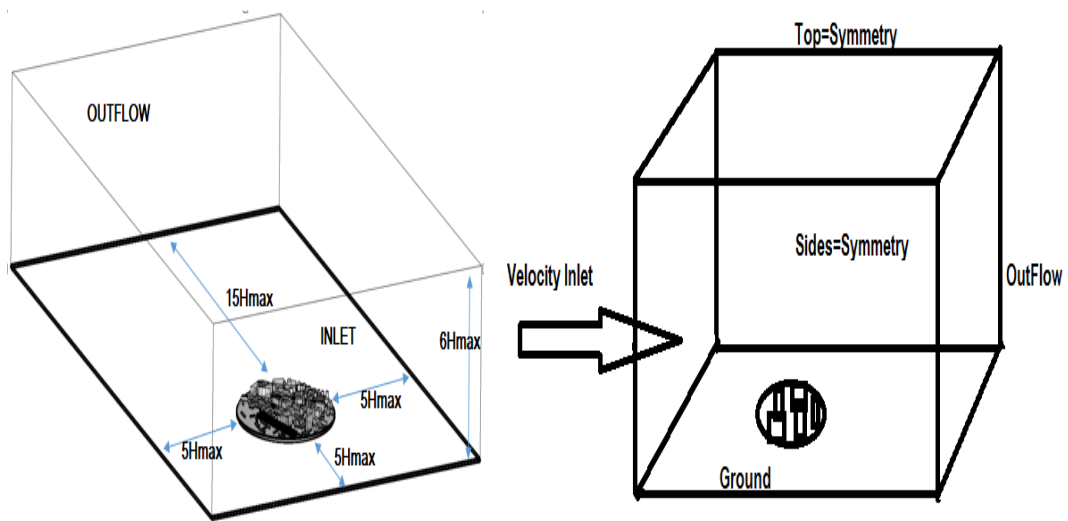
Figure 3.2: a) Computational domain.

3.7   Computational Domain

The actual physical boundary in the computation domain is represented by its bottom side. Among the remaining sides of the computational domain, the top and side boundaries are non-physical thus these are usually placed at a marginal distance from the explicitly modeled area to avert any artificial acceleration of flow that can occur due to these contracted boundaries. The computational domain was computed according to CFD best practice guidelines and have dimensions of 1700 m ×1100 m ×360 m (L × W × H) [75] and is depicted in Figure 3.2 (a). The computational domain consists of an inner, circular subdomain of diameter 500 m which consists of explicitly resolved buildings and street geometry to align it according to prevalent wind direction in the computational model. The highest building has a height H_{max}=60m. All the boundaries except the outflow are placed at a distance of $5H_{max}$ from the inner circular subdomain. The outflow is placed at a distance $15H_{max}$ from the inner circular

subdomain [91]. Moreover, the blockage ratio of building elements in the streamwise direction is kept at less than 3% [75,92]. The other part of the computational domain was modeled implicitly, i.e. by imposing equivalent sand grain roughness heights, estimated based on the updated davenport roughness classification and depicted in Figure 3.5 (b).

The urban geometry is modeled based on the available data on reliable sources, endeavoring to create a realistic model and dimensions of buildings elements with respect to each other for performing simulation in the representative urban microclimate. Moreover, some elements (cars, obstacles, trees) are modeled implicitly by incorporating suitable aerodynamic roughness values. These elements (obstacles) when modeled in their present form, might influence the airflow at local levels but their effect is insignificant at global levels. Moreover, the effect of other elements (trees, cars) is incorporated through modified absorbance and reflectance at the ground.

3.8   Computational Grid

A high-quality computational grid offers the advantages of reducing the discretization error and offering convergence for second-order discretization schemes. To ensure the high-quality grid, the mesh has been generated using Pointwise, V 2018 [93] according to best practice guidelines [75] having overall good resolution and high quality of mesh metrics terms. The mesh was first created on the building surfaces, ground, sides of the computational domains. While creating the surface mesh, 10 cells at least are used on each building's sides using a stretching ratio of 1.2. The building within the region of interest has a high resolution where geometrical detail as small as 1 m edge length is modeled explicitly. The surface mesh consists of 21,617 triangular elements and 732,365 quadrilateral elements. Surface grid extrusion technique named T-Rex was adapted to create volume mesh. The resulting grid (basic) is composed of 23.1 million cells.

3.8.1 Mesh Independence Results
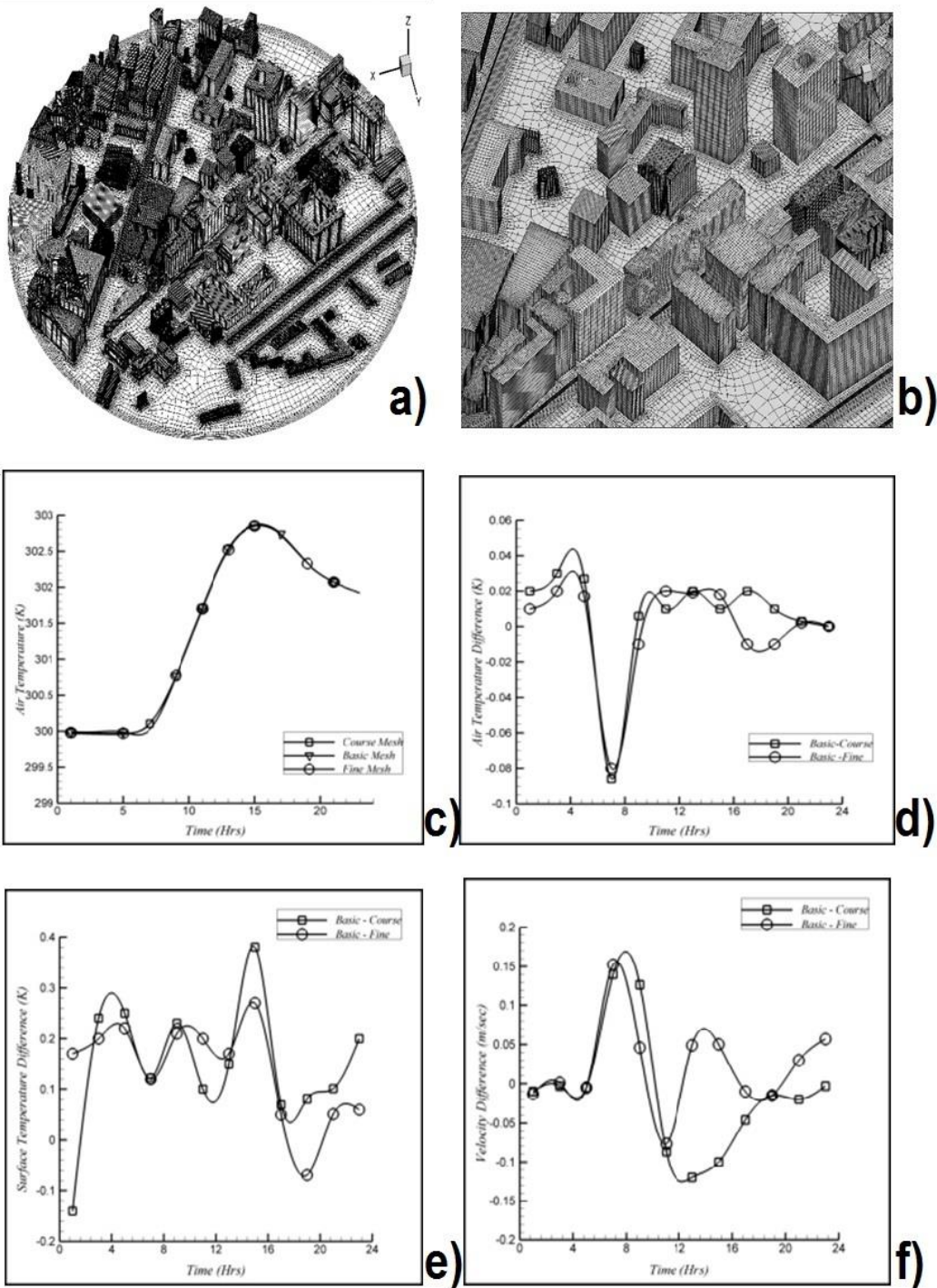
Figure 3.3: (a) Mesh for the circular subdomain, buildings, grounds, and vegetation zones. (b) enlarged view of mesh. Mesh independence study results (c) air temperature (d) air temperature difference (e) surface temperature difference (f) velocity difference.

The mesh has been generated using Pointwise V18 [93] according to best practice guidelines [75]. The mesh was first created on the building surfaces, ground, sides of the computational domains. While creating the surface mesh, 10 cells at least are used

on each building's sides using a stretching ratio of 1.2. The building within the region of interest has a high resolution where geometrical detail as small as 1 m edge length is modeled explicitly and is shown in Figure 3.3 (a and b). The surface mesh consists of 21,617 triangular elements and 732,365 quadrilateral elements. Surface grid extrusion technique named T-Rex was adapted to create volume mesh. The resulting grid (basic) is composed of 23.1 million cells.

Three successive refined meshes have been used to perform grid independence analysis named as coarse, basic, and fine meshes. A refinement factor of 1.2 was applied which resulted in 19.0 million, 23.1 million, 27.1 million cells respectively. The average air, surface temperatures, and velocity are considered as performance indicator variables for this grid-sensitivity analysis and corresponding results are shown in Figure 3.3 (c - f) as twenty-four hourly averaged data. The finest mesh did not show much improvement in results as compared to the finer mesh. Therefore, the basic mesh was selected for the analysis.

3.9   Boundary Conditions

Imposing apposite boundary conditions is very necessary as it directly influences the appropriate determination of aerodynamic roughness length and inlet profiles for flow variable and turbulence. The selection of inlet/outlet boundary conditions varies depending on prevalent wind flow direction. To compensate for the varying wind direction, a circular subdomain, surrounding the implicitly modeled buildings, is rotated inside the rectangular domain. The computational domain has symmetry boundary conditions at its top and lateral directions where the gradient of all variables is equal to zero. The buildings and ground are treated as a wall for which the thermal and radiation values are tabulated in Table 3.4. The reflectivity for these opaque surfaces can be assessed from relation $\alpha+\rho=1$ with α being the absorptivity.

Symmetry boundary conditions are used on the sides of computational domain as the physical geometry of interest and flow/thermal patterns have mirror symmetry. Moreover, they have been used as zero-shear slip wall modeling on these planes i.e., zero flux of all flow variable. Moreover, there is no convective/diffusion flux at such planes i.e., zero normal velocity and zero normal gradient of all variables. Outflow boundary conditions are used at outlet as flow velocity and pressures conditions are not available prior solving the flow. Fluent will automatically extrapolate information from interior thus have no impact of the upstream flow. Outflow boundary conditions

are used to model zero-diffusion flux of all flow variables and overall mass balance correction. A limitation of such boundary conditions is that they cannot be used with compressible flow or to model variable density. For outflow conditions to be used, it must be ensured that flow should be fully developed means that flow profiles in unchanging in the flow directions.

For modeling of incompressible flow. It should be ensured that velocity inlet should be placed at enough distance from the solid obstructions to avoid it to cause non-uniform inflow stagnation properties.

Table 3.4: Thermal and radiation conditions for simulating urban microclimate flow [47,94].

	Material	Heat Transfer Coefficient W.m^{-2}. K^{-1}	Free Stream Temperature (K)	Radiation Temperature (K)	Thickness (m)
Building Wall	Brick/ limestone/ insulation	0.5	296	296	0.15/.15/.05
Building Roof	Brick	0.5	296	296	0.35
Ground Shaded	Earth with Concrete	0.15	283	283	10
Foliage	Porous material	Via System Coupling			Canopy Width
Ground Non-shaded	Earth	Via System Coupling			10

Free stream and radiation temperatures govern the building's internal thermal conditions. For ground, it represents the temperature at depth of 10 m. Based on a study by Richards and Hoxey [95]; the following profiles for mean wind speed, turbulence kinetic energy, and turbulent dissipation rate are incorporated at the inlet through a user-defined function (UDF).

$$U(z) = \frac{U^*}{K} \ln \left[\frac{z+z_0}{z_0} \right] \qquad (3.39)$$

$$k(z) = \frac{U^{*2}}{\sqrt{C_U}} \qquad (3.40)$$

$$\varepsilon(z) = \frac{U^{*3}}{K(z+z_0)} \qquad (3.41)$$

Where $U^* = K.\dfrac{U_{ref}}{\ln\left[\frac{h_{ref}+z_0}{z_0}\right]}$

where Z, Z_0, K, U^*, U_{ref}, and C_μ denote the vertical position above ground, the aerodynamic roughness length, generally equal to = 0.5 or 0.1 m, the Von Karman constant equal to 0.42, the friction velocity, the reference wind velocity at reference height and model constant usually equal to 0.09. The dominant wind direction for a particular day is only simulated. These profiles have been selected since they apply to a wide range of turbulence models and their suitability to model ABL [75,91,92].

The ground with trees is modeled implicitly as a 10 m thick earth layer. A heat flux of zero value is assigned at 10 m depth. The streets insides circular subdomain are modeled with 0.5 m concrete and 9.5 m earth material. Building walls were modeled implicitly with a thickness of 0.35 m having properties of combined brick/insulation/limestone. These walls are treated as air-conditioned spaces having 24 °C temperatures during summertime. Three-dimensional conduction equations are enabled for all wall-type boundaries to cater heat transfer through these boundaries. The material properties are given in Table 3.5. It is pertinent to mention that material properties for all building elements and ground surfaces are the same due to a lack of detailed information. Clearly, this can affect the accuracy of the results.

Table 3.5: Material specifications and components used in this study[47,96].

Material	Density Kg.m^{-3}	Specific Heat J.Kg. K^{-1}	Thermal Conduct-ivity W.m.K^{-2}	Absorptivity (-)	Emissivity (-)
Earth Non-Shaded	1400	1000	1.3	0.75	0.93
Brick with insulation and limestone	2000	900	0.8	0.8	0.91
Earth with Concrete	1600	300	1.5	0.75	0.85
Foliage*[97]	700	2310	0.173	0.75	0.983
Earth Shaded	1400	1000	1.3	0.15	0.93
Water	1000	4187	0.569	0.9	0.95
Limestone	1090	1.3	908	Not a Surface Material	
Insulation	50	0. 03	1200	Not a Surface Material	-

3.10 Thermal Model

3.10.1 Natural Convection

Natural convection was modeled through Boussinesqs approximation, for which gravitational acceleration was defined along the vertical axis as -9.81 m/s^2. The flow involving natural convections are also termed buoyancy-driven flows as density as a function of temperature occurs under influence of the force of gravity which induces flow. Two methods can be used to model natural convection in FLUENT: first, by putting density as a function of temperature, and second, through Boussinesq approximation for small temperature difference in the computation domain. The latter approach was used as it affords faster convergence than the former one. The thermal expansion coefficient is set to 0.0034 1/K. These settings cause the airflow to be affected by convection.

3.10.2 Conduction

Conduction in the wall in the normal direction is modeled in this solver through an energy equation turned on. However, modeling of conduction in planer direction is modeled through shell conduction i.e., by imposing the thermal resistance to heat transfer across the wall thickness. Shell conduction can be applied to walls and junctions.

3.10.3 Radiation

It is modeled in FLUENT with/without participating medium through five radiation models which are given below

- Discrete Transfer Radiation Model
- P1 Radiation Model
- Rossland Model
- Surface-to-Surface
- Discrete Ordinate Model

In addition to radiation, a solar load model is also imposed to simulate the effect of solar radiation. The P1 radiation model [32,47] along with the solar ray tracing model was used to model the solar irradiation and radiative transfer. In the solar load settings, the solar calculator is configured according to the mesh orientation and real urban area coordinates for the sun direction vector. A sunshine factor of 1.0 was selected in the radiation model as the weather was clear and sunny during the studied heatwave period. The longitude and latitude values of 67.11 °N and 34.8607 °E respectively

define the center of our study area. The time zone of the area is +5 Greenwich Mean Time. The general mathematical expression for radiative transfer equation for any medium at position r in direction s is:

$$\nabla.\left(I_\lambda(\vec{r}.\vec{s})\vec{s}\right) + (\alpha_\lambda + \sigma_s)I_\lambda(\vec{r}.\vec{s}) = \alpha_\lambda n^2 I_{b\lambda} + \frac{\propto_s}{4\pi}\int_0^{4\pi} I_\lambda(\vec{r}.\vec{s})\phi\left(\vec{s}.\vec{s'}\right)d\Omega' \qquad (3.43)$$

Where, $\vec{r}$, $(\vec{s})'$, $\vec{s}$ are the radius, scattering, and steering vector; σ_s, α_λ, n^2 are the scattering, absorption, and refraction coefficients, m^{-1}. σ, T, I_λ, $I_{b\lambda} = \sigma.T^4/\pi$ is the Stefan-Boltzmann constant in W/ (m^2.K^4), local temperature in °C, radiation intensity in W/m^2, and black body radiance in Planck function, K^4 respectively. ϕ and Ω are the phase function and solid angle in radiation.

In this study, two radiation models were used.

1. P-1 Radiation model by integrating out the directional dependence in RTE, This results in a diffusion equation in incident radiation. It was applied to solve the RTE in an easy manner using comparative small CPU demand. on the flip side, it considers all surfaces as diffuse and overestimates radiation fluxes from localized heat sources. On the other hand, the DO model was adopted to include the effect of transparency and specular surface, and wavelength-dependent transmission but it affords large CPU demand. Radiation modeled by considering all surfaces as gray, having some spectral emissivity and absorptivity, having no dependence on wavelength.

P-1 radiation model is employed to model the worst-case scenario. The worst-case scenario is always interested in urban microclimate study as previously mentioned in studies. The major limitation of this study or CFD tool is of Fluent, which ignore emitted longwave radiation from porous zone to surrounding buildings.

3.10.4 Solar Irradiance Modeling

In FLUENT, the solar load model is employed to ascertain radiation effects caused by rays of the sun entering the domain. Solar ray tracing is an efficient and practical approach for applying heat sources into the energy equation, outweighing the DO irradiation [78]. The second approach for this model is performing the simulation with solar load mode means to deploy sun location for a given time, position and day into the sky through using this model, transmission from the sun can be determined through wall boundaries for given coordinates.

The algorithm for solar ray tracing is applied for the prediction of energy sources caused by the direct illumination of the sun. The setting of this model in numerical setting is done through the sun position vector and radiation parameters for the beam. thus, calculated heat flux on wall boundaries resulting in incident radiations. This flux is added into the energy equation as a source term. This heat source is incorporated into computation cells adjoining each other in the following patterns: shell conduction, solid and fluid cells. This order can be replaced through text-user commands to include this heat source directly at the adjacent fluid cells. Direct radiation is modeled with two spectral bands to cater to different materials properties in opaque bodies in infrared and visible bands while a single hemispherical band is employed for diffuse radiation. Absorption and transmissivity coefficients used in the FLUENT solver setting are only for normal sun rays and these are then computed by solver to consider the effect of radiation for any angle of incidence. The scattering fraction coefficient incorporates the material reflectivity effect and thus caters to the inclusion/exclusion of radiant amount from the domain. The P1 radiation model is coupled with solar ray tracing to cater for surface emissivity effects. the shading effect is counted with the Barycentric coordinate formula where the quad-tree refinement factor is adjusted with mesh size depending on CPU capacity required to calculate the solar load.

3.11 Roughness Parameters

Since in the vertical spatial scale, the urban physics has interest up to the nethermost part of ABL, thus it becomes important to correctly model it in the computational domain to obtain more realistic and meaningful simulation results. This can only be accomplished by specifying the correct roughness parameters. Z_o is, therefore, set at 0.03 for both buildings and ground in the circular subdomain while its value is 0.5 to 1 for outer rectangular ground. There are five spatial areas where the roughness is usually specified (Figure 3.4) which are described below:

Area 1: The region located upstream of the computational domain. This is very important from a roughness perspective as it directly ascertain the inlet profiles for velocity and turbulence. The estimation of roughness for this area is appraised from a fetch of 5-10 km. This distance of $5 - 10$ km is the least distance for which the ABL can be able to adjust to underlying terrain roughness. Davenport roughness classification applies to the selection of aerodynamic roughness length.

Area 2: The region located upstream of the explicitly modeled area inside the computational domain. This is an implicitly modeled area as the buildings are intentionally removed as being out of interest. This offers the advantage of using lesser computational resources. Davenport roughness classification applies to the selection of aerodynamic roughness length.

Area 3: The ground portion of the explicitly modeled area represents buildings and obstacles. However, small-scale topological features are usually omitted such as sidewalks, fences, trees, etc hence modeled implicitly. To incorporate the true effect of these small-scale topological features, two approaches are usually used; first by increasing the aerodynamic roughness values from Davenport roughness classification and second by incorporating source or sink terms in the equation of fluid flow and turbulence.
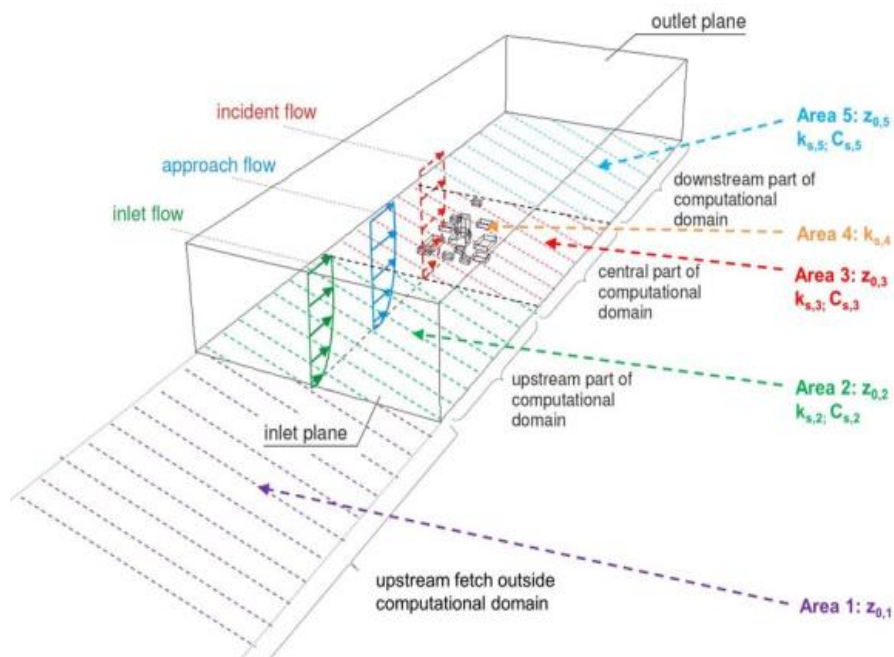
Figure 3.4: Roughness Length.

Area 4: The element surfaces of an explicitly modeled area comprising of building facades and roofs and structures present inside the computational domain. The roughness of these surfaces is attributed to sand-grain roughness height

Area 5: The region located downstream of the explicitly modeled area located inside the computational domain. This has the least important as having the limited effect of upstream aerodynamic disturbance of downward located topological features.

The aerodynamic roughness length of area 1, area 2, area 3, and area 5 is estimated using Davenport roughness classification while equivalent sand-grain roughness height is estimated in area 4 only. The area 1 roughness length affects the inlet profile and turbulence parameters thus it should be carefully estimated. Moreover, there are a couple of ways to mode area 3 as it is always modeled implicitly; first by increasing the aerodynamic roughness length and second by incorporating a source or sink terms in the CFD equations for flow and turbulence. The second approach is usually adopted as roughness length determination is not too straightforward.

The Z_o value at the inlet is chosen according to the distribution given in Figure 3.5 (b). This distribution depends on the direction of the wind, which is necessary for obtaining a horizontal homogeneous boundary layer flow.
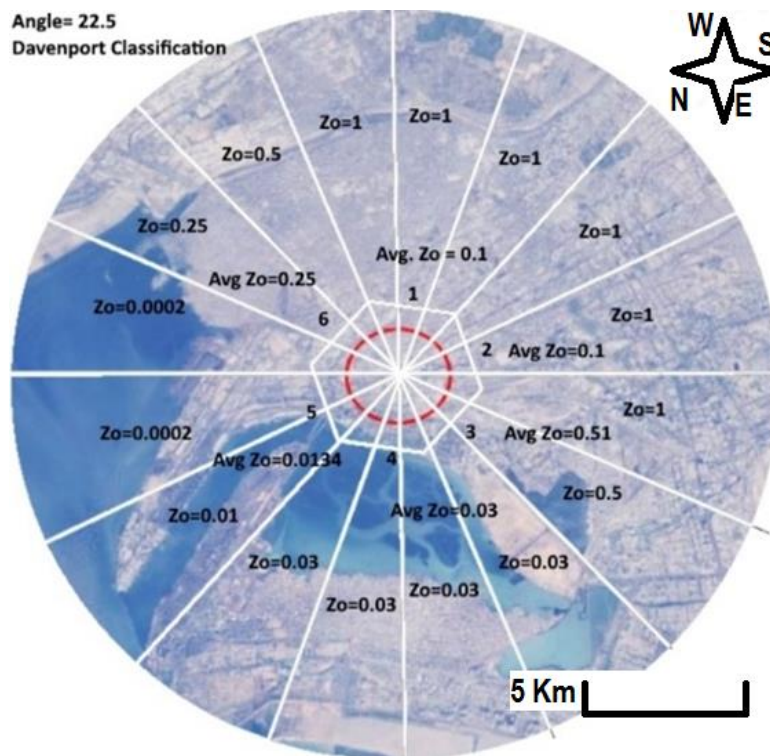
Figure 3.5: Roughness Distribution.

The specification of roughness values is according to landscape description and the detailed distribution of both terms are explicated in Table 3.6 below:

Table 3.6: Roughness Values as per Davenport Classification.

Z0 (m)	Landscape description
0.0002 Sea	Lake or open sea, flat plain covered with snow, beige desert/concrete land tract up to a few kilometers
0.005 Smooth	Land tract with no glaring hurdles and vegetation e.g., beaches, ridge less packed ice and landscaped covered with snow
0.03 Open	Plainland has slight vegetation with separated obstructions having a distance of 50 x the height of hurdles e.g., airports runway area, grazing land but with no windbreaks.
0.10 Roughly open	Plowed area with frequent small crops, temperate broad land with irregular hurdles with spacing equal to 20 obstacles height (e.g., small hedges, line tree rows, separated farms)
0.25 Rough	Fresh "young" countryside with heightened crops, and dispersed obstacles being separated at a horizontal distance of 15 x obstacle height (e.g., yards of the vine, high denser shelterbelts)
0.50 Very rough	"Old" cultivated countryside possessing huge groups of obstructions at a relative distance of 10 x hurdle height e.g., huge farms, forest). Also characterized with a low large, vegetated landscape covered with bushes, newly developed dense forest.
1.0 Closed	A landscape covered with smooth large obstructions having similar-size open spaces, e.g., developed forests or cities.
≥ 2.0 Chaotic	Centre hub of large cities, having low-rise/high-rise buildings.

3.12 Other Computational Setting

The finite volume method in conjunction with the URANS equations employing a "realizable k-epsilon" turbulence model [90] has been employed for CFD simulation. This turbulence model is a prominent model used to model turbulence at an industrial scale and heat transfer simulation. It is also stable and numerical robust, offering compromised results over robustness and accuracy. The second-order discretization scheme was employed for resolving equations of the mean flow, turbulence, and

energy so that the artificial/numerical diffusion caused by using the first-order discretization scheme can be avoided to reduce truncation errors.

The meteorological parameters (humidity, dry bulb temperature of air), obtained from Pakistan Meteorological Department, along with wind velocity and pressure are imposed at the inlet and outlet boundaries of the computational domain. The effect of these parameters is considered through enabling thermal modeling, species transport modeling and continuity equations. Moreover, the free stream temperature and radiation temperature are imposed at building walls and ground to enable building internal conditions and ground bottom conditions.

Turbulence phenomenon is present everywhere in CFD and is significantly influenced by wall boundaries since such locations have viscosity dominant zone thus having large gradient to solution variables. Thus, turbulence at such viscosity-affected zones is required to be modeled which can be tackled using two approaches: one by integrating the turbulence to the wall, but it requires high computational power as resolving the viscosity affected regions are required that all surface be meshed down to the wall encompassing viscous sublayer, and second through the use of suitable wall function. But for securing results accuracy with the latter approach, the first cell center should be placed in the log-law region ($30<y+<300$. Moreover, computational resources are also significantly reduced since wall function acts as a bridge between the wall and fully developed regions, putting no need to resolve the boundary layers i.e reducing the mesh size. The wall boundaries are equipped with the standard wall function, devised by Launder and Spalding [98] along with modification in terms of sand-grain-based roughness (Cebeci and Bradshaw) to solve the fluid wall interaction on these boundaries [99].

To a couple, the pressure-velocity flow fields, the PISO algorithm with neighbor correction was used, as it is highly recommended for transient flow calculations with larger timestep. For transient formulation, the Bounded Second-Order Implicit scheme is used for improved accuracy along with better stability. A time step of 900 seconds was used for unsteady simulations. Convergence was obtained with scaled residuals up to 10^{-5} for all variables except continuity 10^{-4} at the end of each time step.

3.13   Measurement/Evaluation Locations

From simple airflow analysis results, the large surface temperatures have been observed in isolated streets, thus these zones (1st, 2nd, and 3rd zones) in the urban area have been selected for retrofitting mitigations (Figure 3.6). Another reason for mapping three zones is to observe the vegetation effect in denser building areas and spacious areas having different building configurations since the density of vegetation acts as a barrier to wind flow which affects the aerodynamic performance of trees [100,101]. The 2nd and 3rd zone consists of a single tree arrangement along their length while the 1st zone consists of two layers of trees since the available space is quite large. To monitor the effect of vegetation in the wake of the vegetation zone, two zones along the direction of wind were selected. One is in the wake of the 1st zone (plane (A) while the other zone is behind the 3rd zone (plane B). Only one plane is perfectly aligned with the vegetation zone. The only reason for mapping two zones is to monitor the vegetation effect in denser building areas and spacious areas. These two planes are located at 1.5 m in height.

The choice of location for the water/vegetation zone is realistic owing to the availability of space at these locations and the presence of the UHI effect. True simulations were carried out under worst-case scenarios as having conditions of high temperature, humidity, and solar irradiance. For study purpose, three streets are marked with eight monitoring points to account for variable sky view fraction (SVF) of urban area.
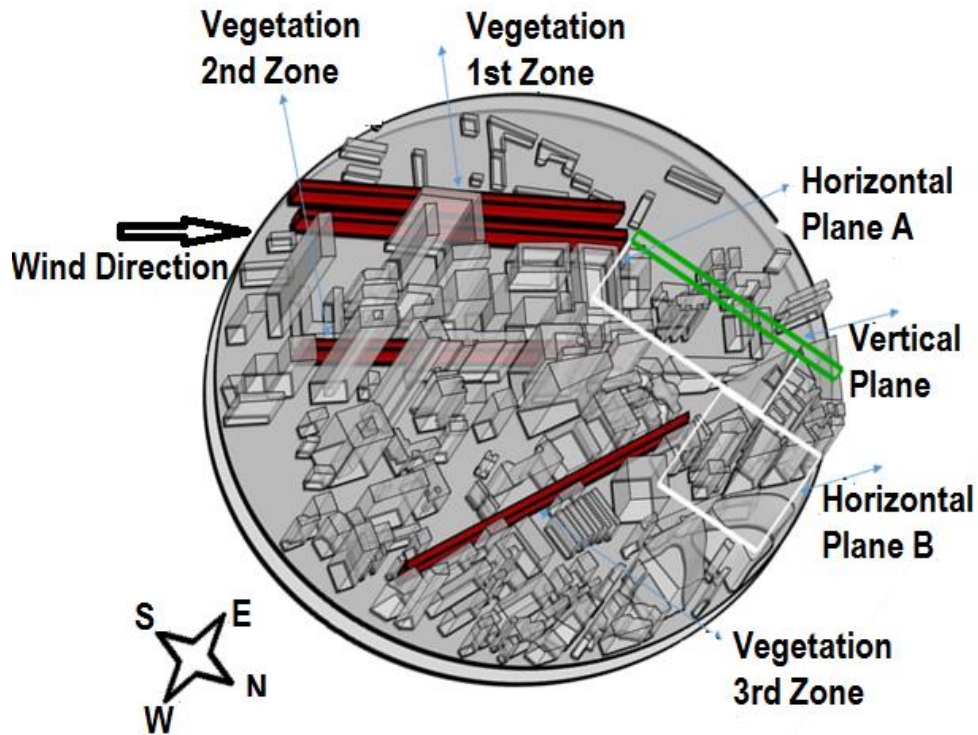
Figure 3.6: Representation of vegetation zones highlighted in red color; representation of horizontal cross-sectional/wake planes highlighted in white color.

3.14 Evaluation Parameters

In all the urban microclimate studies, there are four major parameters which are given below:

- Air temperature
- Surface Temperature
- Wind Velocity
- Therma comfort Index – Apparent Temperature

Air temperature values are accessed at pedestrian height (1.5 m Height) and surface temperature is evaluated over the entire circular domain.

3.15 Description of Study Area

This study focuses on evaluating the mitigation potential of various adaptation measures in single (isolated) streets located in the central area of Karachi, Pakistan. The studied urban area is Pakistan's premier industrial and financial center with estimated GDP of 164 million US dollars. I. I. Chundrigar Road (McLeod Road), is selected as being the spine of Pakistan's largest financial center, since all major financial organizations are headquarters beside this road; and for its repute of being

declared as "Pakistan's Wall Street". It is also the 12th most densely populated urban area in the world [102]. It covers a land area of 3780 km^2 and has around 15.5 million population. Rapid expansion in terms of built density and population has been observed during the last couple of decades. This city has experienced a major increase in heat index and heatwaves in the wake of urbanization [20]. The Koppen Climate Classification subtype for this climate is "Bwh". The city enjoys a tropical climate encompassing warm winters and hot summers. Moreover, the city has considerable variation in climate across the year. The humidity levels usually remain high in the summer months due to the evaporation of seawater.
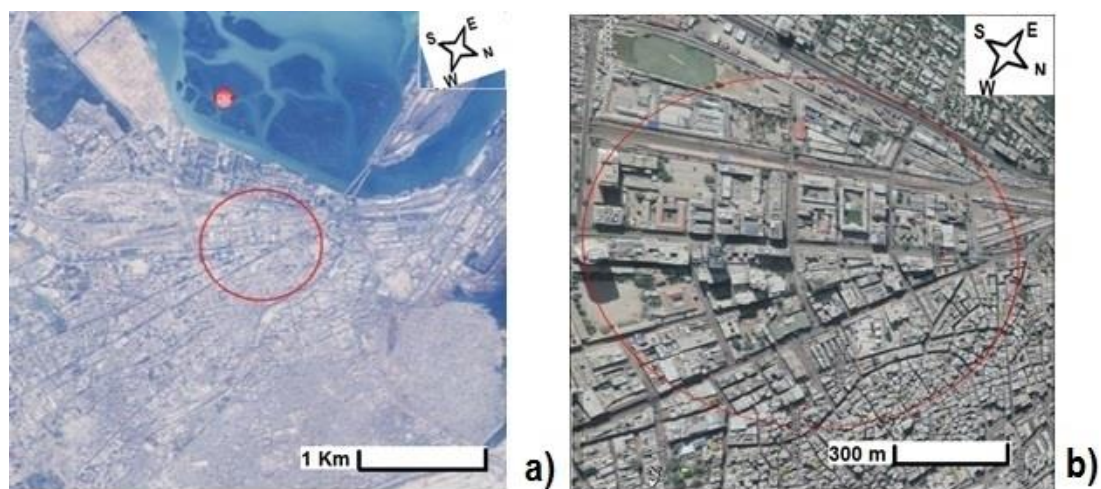
Figure 3.7:((a) Location of urban microclimate understudy in Karachi, Pakistan (b) Aerial view of the area with surroundings, red circle encompassing the modeled zone.

The urban area of 'I. I Chundrigarh is characterized by a hot and humid climate in summer and is one of the hottest regions in Karachi, Pakistan on the summer days, where a combination of extreme summer temperature and high humidity levels caused high thermal stress. Moreover, the high dense morphology with tall buildings limits the ventilation. The average annual precipitation, humidity and temperature is 6.88 in, 55% and 32.9 °C respectively. This study area is modeled in CFD as circular subdomain having radius 500 m: thus covering an area of 0.785 km^2. It many tall buildings, offices, and residential complexes possessing low SVF with 10 m to 110 m high buildings with their average height of 30 m. A view of this study area is shown in Figure 3.7 (a and b). The climatic parameters (air temperature, relative humidity, solar radiation, wind speed, and pressure) are measured on an hourly basis at

observatory, located 4 km away from studied location by Pakistan Metrology Department (PMD) for the heatwave period 2015, and are given at Appendix-A. The air inlet temperature and humidity of 20 °C and 8 g/kg respectively were used.

3.16 Summary

This chapter entails all the details related to the performance of CFD studies, followed by diverse studies performed in the field of urban physics with different mitigation measures. In the numerical method section, numerical settings, boundary conditions, and material properties are discussed. Moreover, the detail of the study area is elaborated. the focus of this literature review is on vegetation modeling parameters along with their different morphological characteristics. The research gap came out that the effect of vegetation has not so far been studied extensively by considering their transpiration rate and actual form drag coefficient. At the end of this section, the selection of evaluation zones and evaluation parameters are enumerated.

Chapter-4

Effectiveness of Vegetation

4.1 Introduction

This chapter deals with the effectiveness of street trees with their various modeling and morphological characteristics. No doubt, thermal comfort conditions can be improved by reducing air temperature and surface temperature with the integration of street trees into the urban environment by providing various microclimatic benefits through alleviating solar penetration [103], creating shade [104], and through evapotranspiration [32,45]. However, trees, depending on their morphological characteristics, have the variable potential for the regulation of thermal comfort. A more realistic and accurate consideration of actual form drag coefficient and variable tree transpiration rate (vegetation modeling parameters) can improve the quality of computational fluid dynamics (CFD) simulation results. In this work, computational fluid dynamics (CFD) simulations using unsteady Reynolds-averaged Navier–Stokes (URANS) equations have been performed to analyze the cooling effect/ intensity of vegetation with its four morphological characteristics and two modeling parameters for the heatwave period (18-22 June 2015) in a hot humid urban environment. These morphological characteristics include trunk height (HT), crown diameter (CW), crown height (CH), and leaf area density (LAD). The thermal comfort conditions are examined at pedestrian height by evaluating four climatic parameters: the reduction of ambient air temperature, surface temperature, and apparent temperature; the alteration of airflow velocity. The vegetation model used is only validated using the sub-configuration method rather than performing an experimental method. The results are then compared for the vegetation case, open-space case, and built case. The study shows that consideration of more realistic values of these parameters yields significant variation in the determination of cooling potential and flow characteristics developed by applied vegetation.

This section comprises three subsections which are:

A.   Vegetation Case, Built Case, and Open Space Case

B.   Effect of Vegetation Modeling Parameters

C.   Effect of Different Morphological Characteristics

The cooling effect is analyzed in the form of contours at pedestrian height (h=1.5) and as 24-hourly average data. The results are presented as averaged data rather than maximum and minimum values as it has been observed from previous studies that single-lined trees have a localized effect on lowering the temperature in hot humid microclimates [105,106]. This average data is averaged over the whole circular domain. Moreover, the cooling effect is also analyzed at certain evaluation points, located on or near vegetation zones in the urban streets to exactly evaluate the effectiveness of the tree species at diverse SVF locations.

4.2 Validation Studies

The validation studies are usually carried out to determine the extent to which the simulated model can be a precise depiction of the real world from point of view of model application [107]. It refers to the process of quantifying the uncertainties in numerical method, encompasses input uncertainties and quantification of physical uncertainties [108,109]. The input uncertainties can be assessed through uncertainty analysis or sensitivity analysis while physical uncertainty can be evaluated by undertaking a comparison of CFD results with high-quality experimental data. The correct determination of uncertainties values for numerical errors is compulsory for conducting a meaningful validation study [109].

In urban, the Sub-configuration method is usually adopted for validation for cases where experimental data is not available or cannot be conducted. This method of comprising of splitting of actual configuration into smaller divisions possessing some or all of features of this actual configuration. High-quality experimental data is available publicly online for generic sub-configurations and is usually used in CFD simulation [110–112]. The set of computational parameters and settings which gives accurate simulation results for the sub-configuration method is then used for actual simulation of the real-world problem [75,107]

4.2.3   Reference Case and Surface Temperature Validation

The unmitigated scenario is modeled without proposed interventions to simulate the existing conditions and used as a reference case and for subsequent assessment for identification of Spatio-temporal overheating patterns thus considered in the selection of areas for implementation of mitigation measures. Fifteen different unsteady cases (Tabulated in Appendix-A) were modeled based on the prevalent wind, humidity, and temperature conditions for the heatwave period (18-22 June 2015). It is pertinent to mention that wind gusts have not been modelled explicitly, since the data provided by Pakistan Meteorological Department was provided on hourly averaged values, thus ignored instantaneous wind gusts.

The results of the reference case are validated against the Moderate-resolution Imaging Spectroradiometer (MODIS) satellite data [113] as has been widely adapted to validate simulation results in urban microclimates [47,114]. The evaluation is made at three different times of the day, as shown in Figure 4.1 (a, b, and c), and then averaged to obtain a single value over the region. Such averaging procedure has already been adopted in some previous studies [47]. From the surface temperature contours, the highest temperature is present along these single streets, especially at times of high solar irradiance. The maximum temperature of the ground exceeds 50 °C due to the proliferation of impervious surfaces which causes an increase in thermal discomfort in such areas because of emitted infrared radiations and increased air temperature owing to the convective process. The lowest temperature is observed in the building shadowing area and building facades around 40 °C which is due to shorter solar access at these locations.

Temperature is the main performance indicator in urban studies. In an unmitigated scenario, the surface temperature is simulated, and a comparison is made with satellite measurements. The highest surface temperature inside the street of the circular domain is found to be around 50 degrees. This temperature increase with increased solar irradiance is observed in this scenario. Moreover, the highest temperature is also observed at buildings located beside these streets owing to the high solar absorptivity of these buildings' surfaces. Another reason for the high surface temperature at buildings walls is the presence of lowers wind velocity (low convection), resulting from surrounding building elements, and causing low air circulation at building

facades. Moreover, FLUENT calculates surface temperature on buildings, based on incoming radiations by taking sunrays as vector and their deflections through space. Moreover, the building shadings effect causes a drop in surface temperature at the street adjoining these buildings as clearly manifested from Figure 4.1. Higher surface temperature exerted forces of convection of air resulting in a higher temperature at surfaces resulting from the smaller transfer of heat if lesser air velocity is present.

In validation of surface temperature, buildings are not considered as all buildings have the same heated surface made up of the same material (white-coated and black-coated surfaces are heated up to the same levels). Moreover, a balance between results reliability and computational time is made by modeling an approximate model of the realistic scenario.
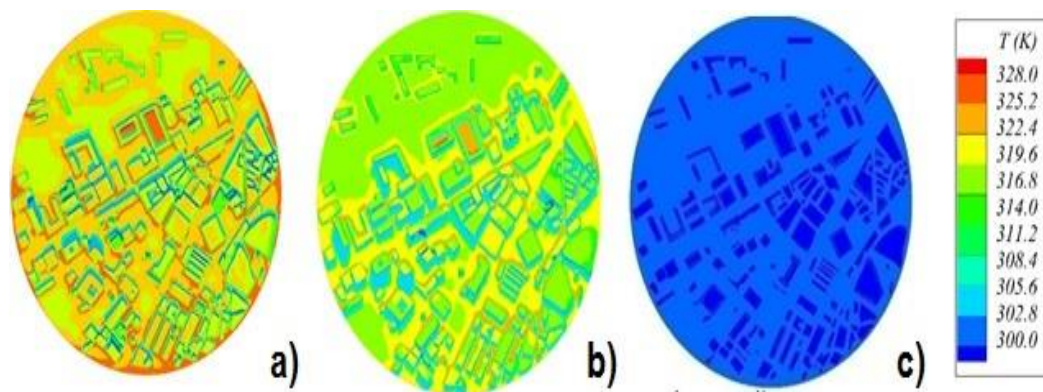
Figure 4.1: Contours of surface temperature, 19 June 2015 (a) for 11 00 (b) for 15 00 (c) for 2300 hrs.

The satellite imagery database MODIS monitors the diurnal surface temperature with up to 1.1 km temporal resolution. Since the MODIS represents only a single value for any moment for the interesting location; thus minimum, maximum and standard deviated values of this surface temperature cannot be extracted. This is the main reason for making the comparison in terms of spatially averaged surface temperature only. To measure the satellite surface temperatures for a specific coordinate location, an HDF file from the online MODIS database is used and temperature measurements are extracted using QGIS 2.18 [113].
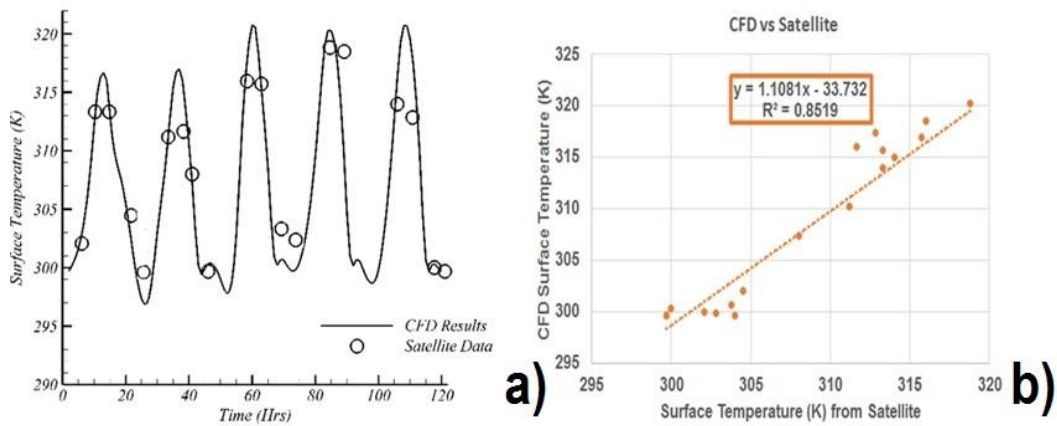
Figure 4.2: a) Comparison of surface temperatures between CFD and satellite measurements for the heatwave period (18-22 June 2015) b) regression analysis.

Figure 4.2 (a and b) shows the comparison between the CFD results and experimental data. It can be observed that a good agreement exists between the surface temperatures of the two approaches as R^2 (correlation statistics) value is quite close to 1. However, there exists some deviation at 12 hours and 60 hours of the heatwave period 2015 where the maximum deviation between the two data is 3.4 °C and 2.0 °C respectively.

This difference could be due to the following assumptions as explained in similar studies [32,47]:

• The emittance of the planer conduction for the building as CFD simulation was only conducted with one-dimensional conduction. As the temperature change is more susceptible on the ground surface, thus affects the average surface temperature and causes of the difference.

• The other main reason for the difference is the averaged value based on hourly data which might not be reasonably true for generating correct results, especially at the time of high wind and DBT hourly variation.

• The absence of thermal stratification of the atmospheric boundary layer (ABL) in the CFD simulation can also deviate from the flow field results.

• The modeled simulation domain only represents 10-15 % of the location while the satellite imagery data represent a single value for the entire location.

This suggests that the proposed numerical settings are reasonably accurate/reliable for appraisal of the cooling capacity of mitigation measures.

4.2.4 Validation of the Vegetation Cooling Model

The transpirational cooling effect of vegetation on air temperature is usually modeled by using a cooling power-based source or sink term in the canopy area. The measurements data of [85] was taken as reference (Figure 4.3)). Shshua-Bar measurement results have been used for comparison since it has been employed by [32,47] to validate the transpiration cooling power. Another reason for using this study was ease in replicating the boundary/modeling conditions. He examined the vegetation effects on the microclimate for constructed, semi-enclosed courtyards with various vegetation types and arrangements. For this validation, steady-state simulations were performed and compared with the measurement data. The comparisons have been made for 7th July 2007 in terms of averaged data. The courtyard discretization contains a structured mesh of 0.15 m edge comparable to the one used in [85]. On the outer walls of the buildings, an unstructured grid was applied with a gradual increase in cell sizes toward the boundaries of the domain resulting in a total of 1.9 M cells (Figure 4.3 (b)).

A realizable K-ε turbulence model was used to perform steady-state RANS simulations. Solar irradiation and the radiative transfer were modeled using solar ray tracing and the P1 radiation model. The simulation used input parameters such as velocity and temperature as mentioned in [85]. The no-slip condition was imposed on the ground and building wall and assigned an aerodynamic roughness length Zo=0.3 m. Thermal and radiative properties tabulated in Table 3.5: Material specifications and components used in this study[47,96]. were incorporated at the inflow and wall boundaries. The aerodynamic effects of trees inside the courtyard were incorporated by employing the transport equation of momentum, turbulent kinetic energy, and turbulence dissipation rate via UDF. Moreover, the volumetric cooling power of vegetation was provided as a source term to the porous zone cells which also varies with leaf area density. At the inflow boundary, a vertical profile for mean velocity, K, and ε was employed as given in equations 3.39 – 3.41. Outlet pressure was prescribed on the outflow side and symmetry boundary conditions on top and lateral sides.
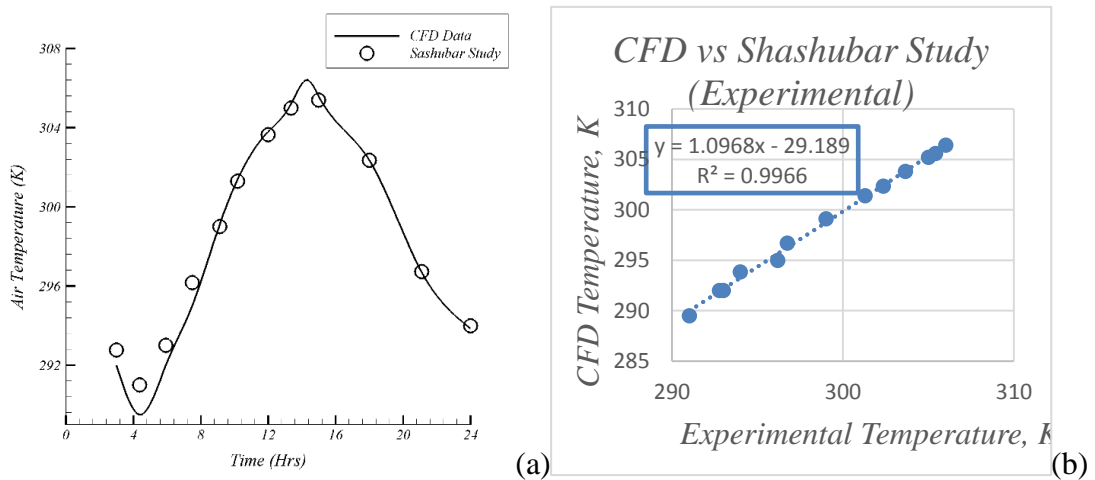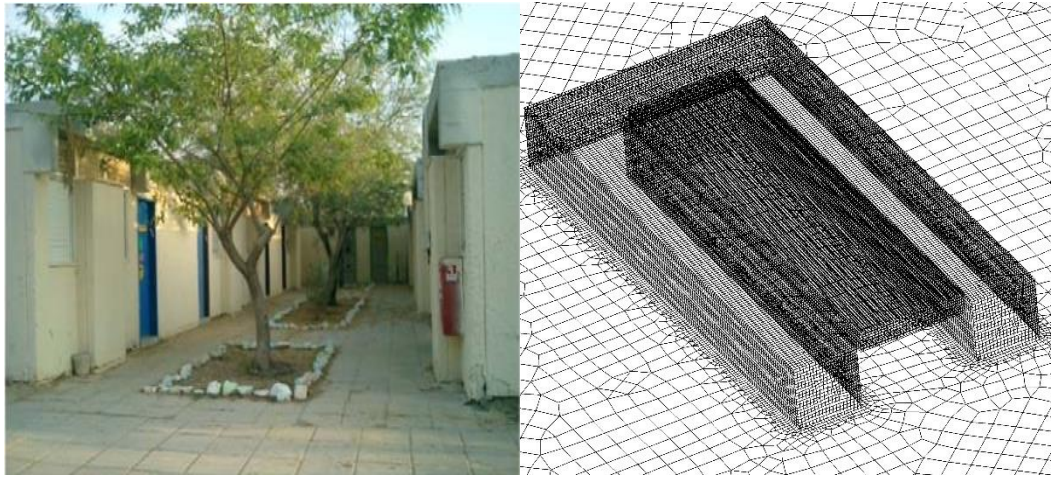
Figure 4.3: (a) Area of interest b) meshed model c) comparison of air temperature between CFD and Shashubar study (d) Regression analysis, CFD vs Shashubar [85].

Figure 4.3 (c) shows the comparison of simulation results and measurement data for the bare courtyard for cooling power P_C= 750 W/m^2 which indicates that air temperature exhibited a fine relationship between the measurement and CFD results as also clear from regression analysis between the simulation and measurement in Figure 4.3(d) where R^2 value is quite close to 1. It is evident from the graphs that CFD predicted values are slightly more than the measurement data. The maximum difference of 1.5 °C exists between the two results for 750 W/m^2 cooling power at 03 AM which is 0.5 °C at 3 PM during sunshine hours.

From both the validation studies, where a reasonable agreement is obtained, it is thus obvious that CFD can predict the urban microclimate accurately. The results of CFD can therefore be exploited to identify the problem areas and appraise the impact of mitigation measures.

4.3 Base Case for Vegetation (CVCP/TDC) - TC1

Returning to the main case of this study, the base case for vegetation "Constant Cooling Power/Tuned Drag Coefficient (CVCP/TDC), TC1"is first simulated by modeling constant volumetric cooling power along with tuned drag coefficient without incorporating any transpiration source of the vegetation into the canopy zone. The results of this case were presented in terms of air temperature contours and its difference. A comparison of these results was made with simple airflow calculations to determine the effectiveness of this intervention (vegetation).

A simple representation of air temperature at three instances of the 19 June 2015 is shown in Figure 4.4 (a-c). Moreover, the contours of an air temperature difference between the base case and the case with applied vegetation are shown in Figure 4.4 (d to f), depicting the intensity of the cooling effect. This effect is quite prominent near vegetation zones owing to the presence of large moisture content and tree shading. There still exists a certain level of cooling of open spaces from Figure 4.4 (d and e) which is usually attributed to higher wind velocities, resulting in swift lowering of the surface temperature because of the large spatial exchange of heat. This slight cooling presence is also owing to lesser absorptivity of open area which further lowers the solar radiation absorption on wall-type surfaces. The cooling effect reverses at nighttime and is replaced with warming in the vicinity of the vegetation zone as shown in Figure 4.4 (f).
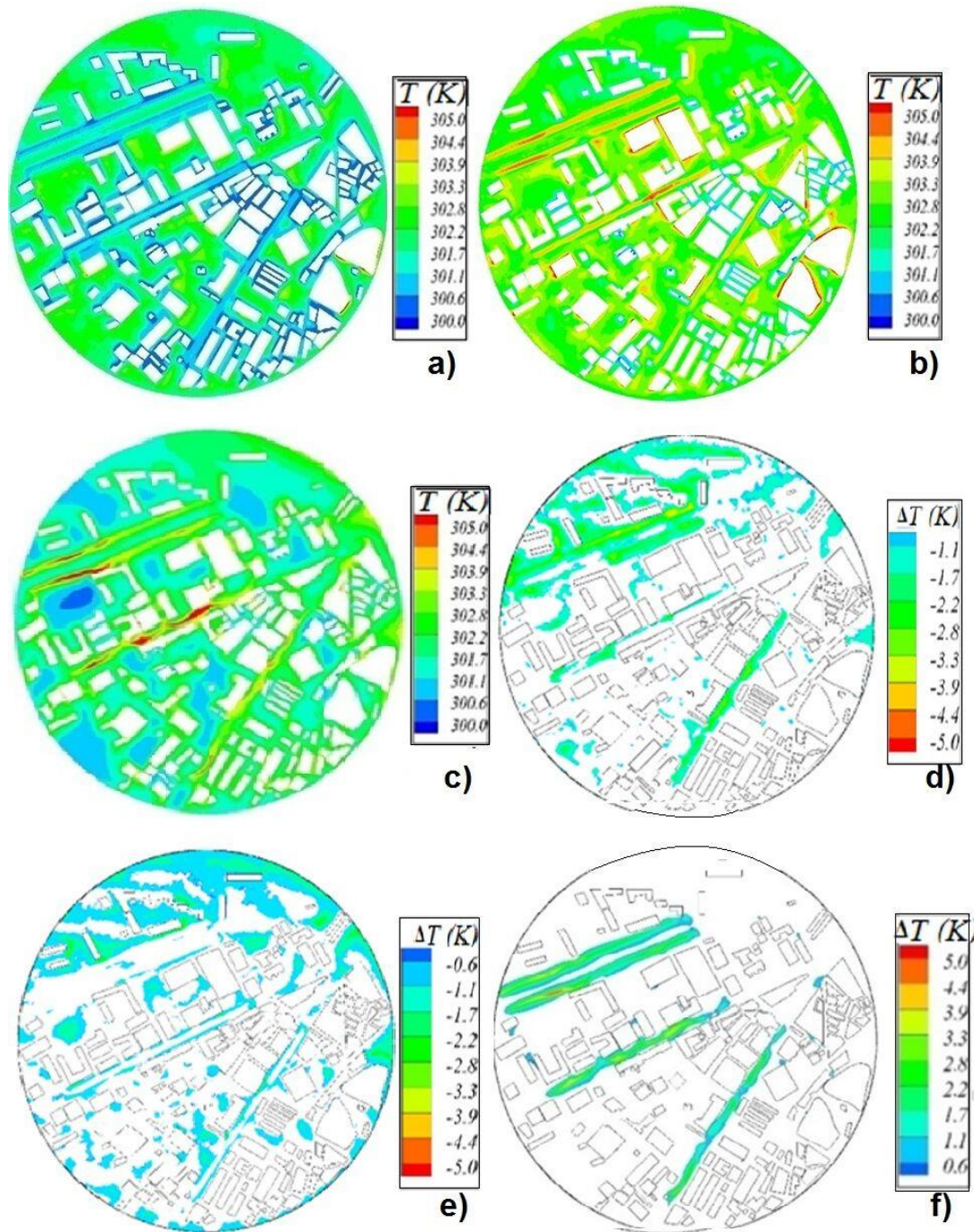
Figure 4.4: Contours of air temperature, 19 June 2015 at z=1.5 m. (a) for 1100 LST (b) for 1500 LST (c) for 2300 LST.

4.4 Vegetation Case, Built Case, and Open-Space Case

The effectiveness of vegetation is examined by carrying out a separate simulation with representative vegetation zones and settings mentioned in section 3.3.

A.   Base case with open space i.e., without representative vegetation and buildings (open-space case) (section 4.1)

B.	Open Space replaced with representative buildings (built case) (section 4.2)

C.	Open Space replaced with representative vegetation (Vegetation case) (section 4.2)

Then a separate simulation was run for the built case where the isolated streets open space was replaced with the representative buildings having equivalent height as of vegetation porous zone. In all the studied cases, the anthropogenic heat sources were eliminated owing to the lack of complete details over the studied domain. The results of all three cases were calculated and compared with each other to appraise their potential for improving/degrading climatic conditions.

4.4.1 Twenty-Four Hourly Distribution

Figure 4.5 (a) shows that applied vegetation (vegetation case) provides a large ambient air temperature decrease when compared with built case and open-space case. The cooling potential is at its peak at midday when the sun is overhead. The air temperature increases gradually without planting vegetation from 7 AM to 2 PM then gradually decreases after reaching a peak of 30 °C at 2 PM. After the intervention of vegetation, the air temperature trends follow the pattern as that of open-space case results but with reduced magnitude. It is quite clear that air temperature reduction of 1.2 °C occurs with vegetation case when compared with built case and this maximum difference occurs in the early afternoon. On the contrary, a reduction is of 0.7 °C only with vegetation case as compared to open-space case.

Figure 4.5 (b) shows that the largest surface temperature decrease occurs with the vegetation case. A reduction of about 4.0 °C in surface temperature occurs with the inclusion of vegetation as it results in low heat admittance by reducing the accumulation of solar energy in the urban area. From the 24-hourly results in Figure 4.5 (b), it is quite clear that a surface temperature reduction of 0.9 °C occurs with the vegetation case minus built case and this maximum difference occurs in the early afternoon.

The graph in Figure 4.5 (c and d) shows the average flow velocities and actual apparent temperature reduces with the addition of vegetation. A maximum reduction of apparent temperature is 1.4 °C when vegetation replaces the buildings while it is 0.6 °C when it replaces the open spaces. It is evident from Figure 4.5 (d) that the vegetation case provides improved thermal conditions while the build case causes it

to worsen under representative climatic conditions when compared with the open space case.
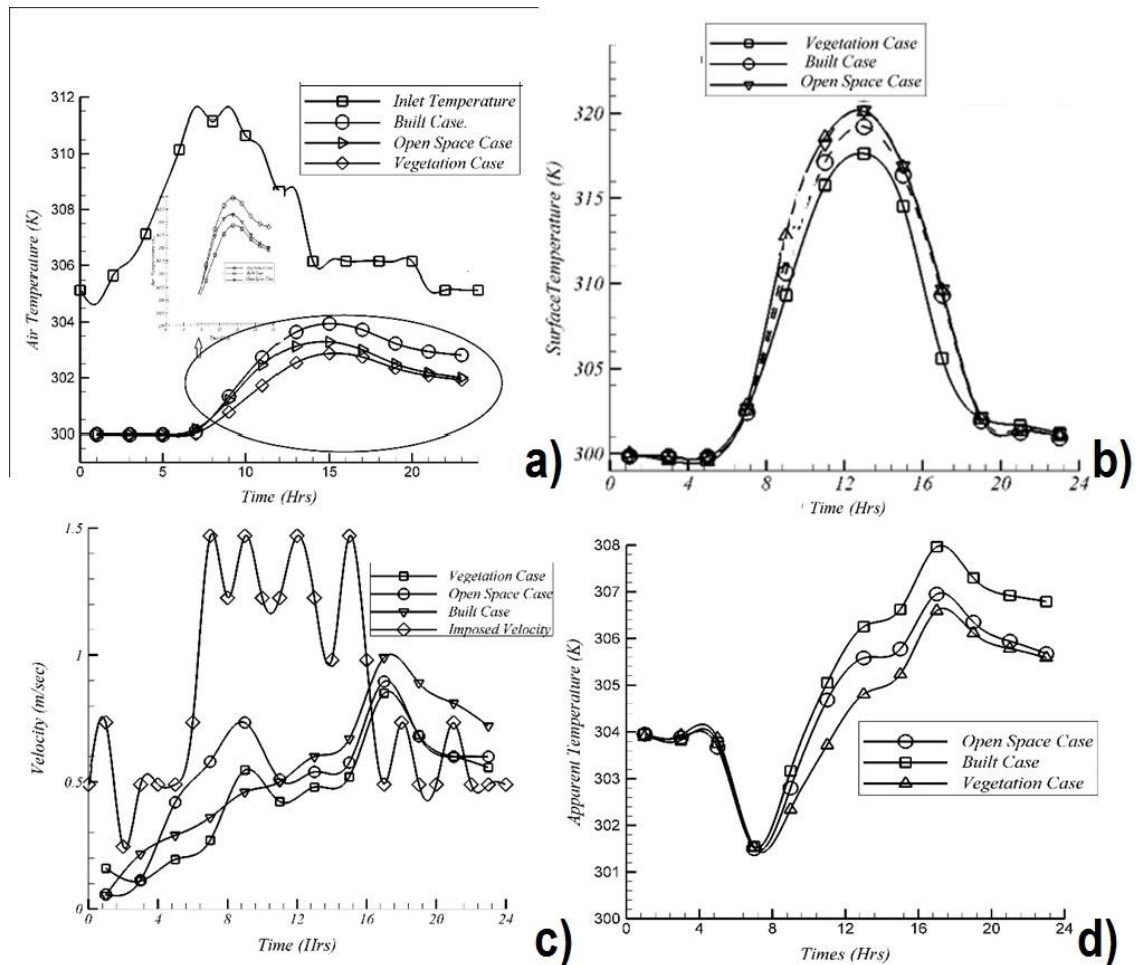
Figure 4.5: 24 hourly distribution of three cases in terms of (a) air temperature (b) surface temperature (c) flow velocity (d) apparent temperature.

4.4.2 Spatial Distribution of cooling effect

The contours of air temperature for the vegetation case illustrating the cooling effect at both planes are portrayed in Figure 4.6 (a and b). This effect is quite prominent near to vegetation zone and in the region surrounded by buildings, owing to low wind velocities. This cooling effect is spread over the larger area in a built case (buildings replaced with vegetation) as compared to the open-space case. There still exists a certain level of cooling with a case of open space which is usually attributed to higher wind velocities, resulting in swift lowering of the surface temperature because of the large spatial exchange of heat. This slight cooling presence is also attributed to lesser absorptivity of open area which further lowers the solar radiation absorption on wall-type surfaces. vegetation cooling effect prevails to larger wake distance at plane A as

it is quite in-line with vegetation zones and vegetation is replacing the buildings (Figure 4.6) while no difference in terms of temperature reduction is observed at plane B showing the highly localized effect of vegetation (Figure 4.6 (d to f)).
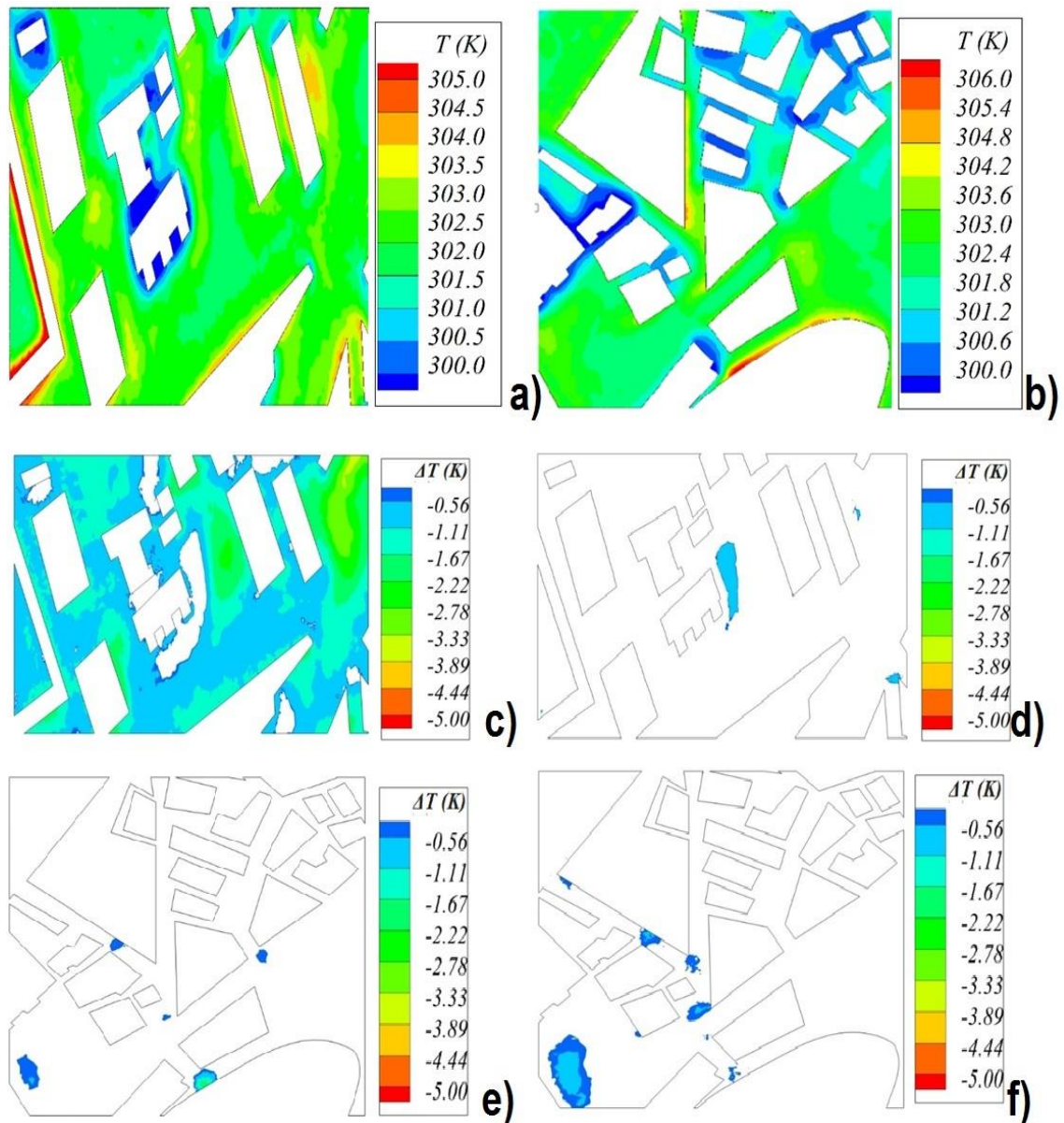
Figure 4.6: Contours of air temperature for vegetation case at Z=1.5 m for 1500 LST, 19 June 2015 (a) plane A (b) plane B. Contours of the air temperature difference between (c) vegetation case and built case, plane A. (d) vegetation case and an open-space case for plane A. (e) vegetation case and built a case for plane B. (f) vegetation case and an open-space case for plane B.

4.4.3 Night Distribution of Cooling Effect- Warming Effect

The distribution of cooling effect during the night is investigated by examining the result of aforesaid cases at pedestrian height and along the wind direction. The nighttime effects of vegetation are monitored at 21 00 LST. The cooling effect reverses

at nighttime and is replaced with a warming effect close and in the vicinity of the vegetation zone as shown in Figure 4.7. This effect however appears when open space is replaced with representative vegetation. The result is represented in the whole domain as the difference between the two cases (Figure 4.7) since no appreciable difference in representative wake planes (Plane A and Plane B) has been observed at nighttime. At nighttime, cooling power becomes zero for all scenarios and all such cases receive the same amount of solar irradiance. The warming effect has an intensity of about 2.0 °C.
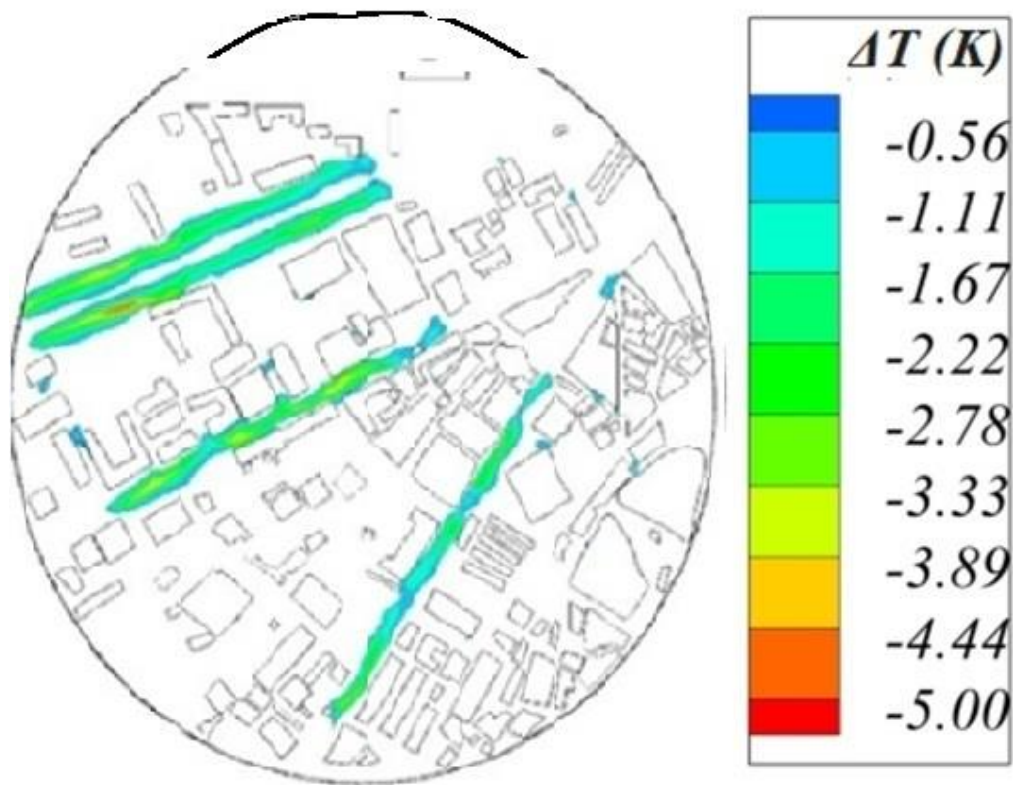
Figure 4.7: Night distribution of cooling effect at Z=1.5 m for 2100 LST, open space case minus vegetation case.

4.4.4 Spatial Distribution of Flow Velocity

The distribution of flow velocity at both the wake plane is portrayed in Figure 4.8 (a and b). The wind accelerated at open spaces behind the wake of vegetation zone while it diminishes in the vicinity of confined spaces due to the drag effect of buildings. From velocity contours in Figure 4.8 (c to f), a difference prevails over the greater wake area when the representative vegetation replaces the representative buildings at both planes A and B. However, when open space is replaced with representative

buildings, velocity reduction is somewhat low as compared to the first scenario. Since the representative buildings and vegetation have a slimline arrangement which causes a very slight difference in their effect on flow velocity owing to the low drag of these imposed elements. The intensity of the former one is however greater by 0.1 m/s.
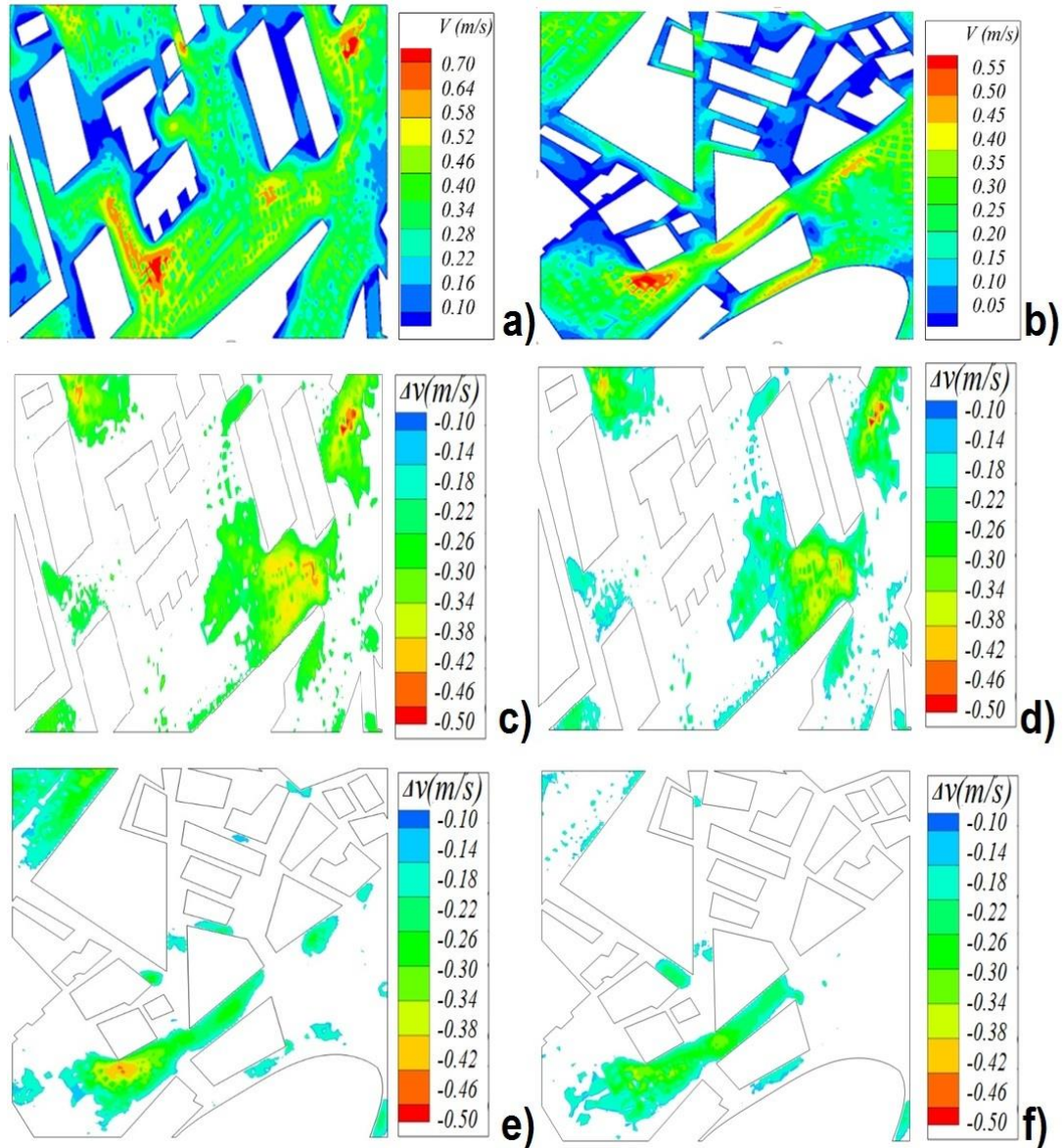
Figure 4.8: Horizontal distribution of flow velocity at Z=1.5 m for 1500 LST, 19 June 2015. (a) contours of flow velocity for vegetation case, plane A (b) contours of flow velocity for the vegetation case, plane B (c) contours of velocity difference between the vegetation case and built case for plane A (d) contours of velocity difference between the vegetation case and open-space case (e) contours of velocity difference between the vegetation case and built case for plane B (f) contours of velocity difference between the vegetation case and open-space case for plane B.

4.5   Effect of Vegetation Modeling Parameters

To evaluate the effectiveness of the mitigation measures toward UHI alleviating and to improve the urban thermal environment for pedestrians, tree vegetation with its two modeling parameters "Constant Cooling Power (CVCP) vs Transpirational Cooling Power (TRCP) and Actual Form Drag Coefficient (AFDC) vs Tuned Drag Coefficient (TDC)" were explored, numerically implemented, and evaluated in solver, and results were compared with the reference case. Simulations have been carried out according to the best practice guidelines for urban flow CFD simulations [91,92]. In this regard, four cases tabulated in Table 4.1 were studied. A simple case "Reference Case (RC) without incorporating any bioclimatic interventions was first simulated to model the existing condition. After this, a base case with vegetation is modeled by incorporating constant cooling power and tuned drag coefficient. Next, the simulations are performed with two vegetation modeling parameters i.e., "transpirational rate" and "actual form drag coefficients" to analyze the cooling effect of the street trees for 19th June 2015. These parameters are incorporated through UDF in vegetation source terms according to the relations, described in Equations 3.18 – 3.22. The impact of the vegetation transpiration rate can be simulated by incorporating water release in the canopy area in addition to the variable volumetric cooling power, controlled by real transpiration rate and canopy zone temperature. The two volumetric cooling powers "TRCP and CVCP" are assigned to cells of the vegetation zone according to the relations 8 to 10. All study cases are tabulated in Table 4.1.

Table 4.1: CFD Simulation Cases.

Sr. N	Scenario	Materials	Modeling Parameter	Case Name
1	Reference Case	None	None	CR
2	Vegetation Case	Vegetation	Tuned drag coefficient/Constant cooling power	TDR/ CVCP/ TC1
3	Actual form drag coefficient	Vegetation	Actual drag effect	AFDC
4	Transpiration rated cooling power	Vegetation	Vegetation transpiration rate	TRCP

Figure 4.9 (a) shows that vegetation modeled with actual form drag coefficient provides the largest reduction in ambient air temperature when compared with the

SAF case without vegetation. This is then followed by TRCP and CVCP. The cooling potential is at its peak at midday when the sun is overhead. The air temperature increases gradually without planting vegetation from 7 AM to 2 PM then gradually decreases after reaching a peak of 30.25 °C at 2 PM. After the inclusion of vegetation, the air temperature trends follow the pattern of the SAF results but with reduced magnitude owing to its ability to block sun shortwave radiation. The reduction produced by the AFDC, TRCP, and TDC is 1.2 °C, 0.9 °C, and 0.4 °C respectively compared to a SAF case. A reduction of about 4.0 °C in surface temperature occurred with the inclusion of vegetation (Figure 4.9b). The greatest reduction was observed with TRCP followed by AFDC.
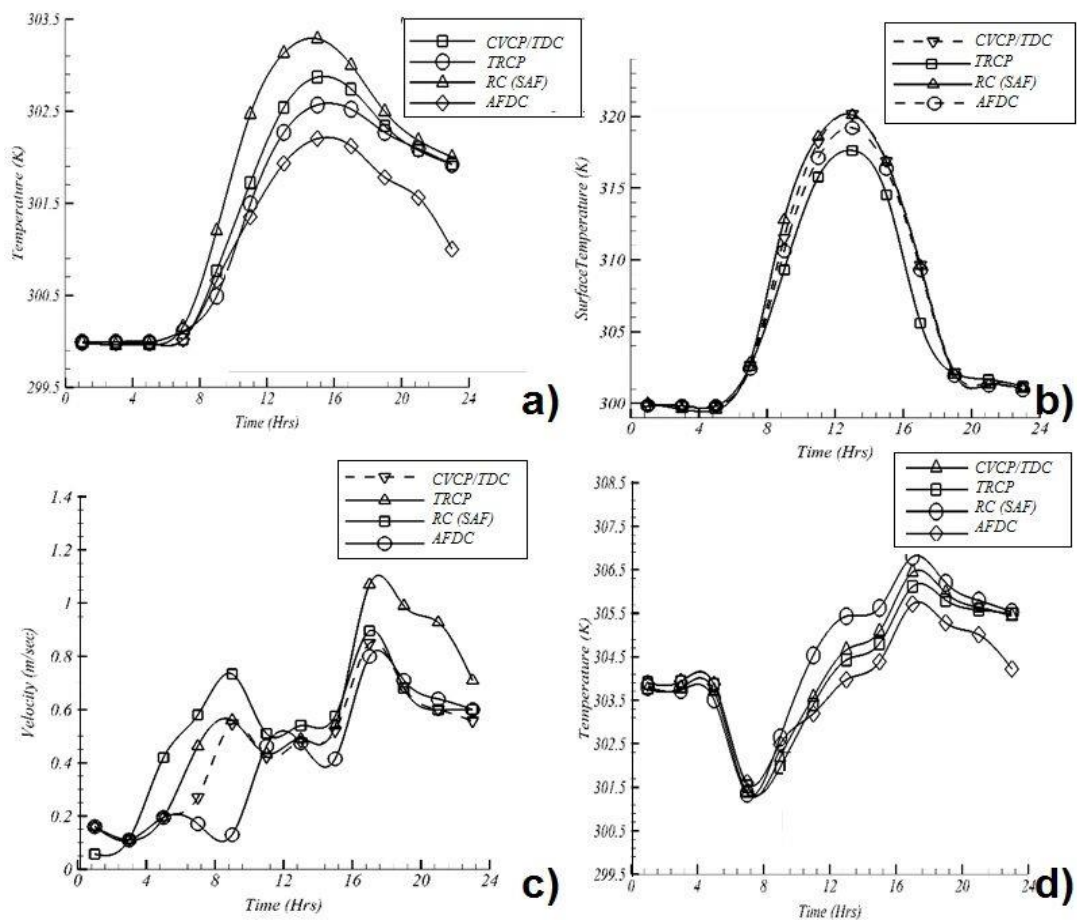
Figure 4.9: Effect of the modeling parameter; 24 hourly distribution of (a) air temperature (b) surface temperature (c) velocity (d) apparent temperature.

The graph in Figure 4.9 (c) shows the average hourly flow velocities with and without vegetation. It is evident from the graph that flow velocities decrease with the addition of vegetation. The actual form drag coefficient has the highest impact in reducing velocity. This lower velocity leads to improper ventilation and heat accumulation

below the canopy zone and windward/downward sides of vegetation and buildings. Among the studied cases, the largest decrease occurred with AFDC, followed by CVCP and CR.

To represent vegetation effect on thermal comfort, the result has been presented in another bioclimatic index called apparent temperature (Figure 4.9 (d). The comparison results show that vegetation modeled with actual drag coefficient provides better thermal comfort as it results in low apparent temperature i.e., 1.0 °C reduction. The cooling power has a relatively low effect on the apparent temperature owing to a small difference in air temperature and velocity as shown in Figure 4.9(a and c). It is also evident from Figure 4.9 (d) that the average apparent temperature reduction is 0.7 °C with the use of transpirational volumetric cooling power during the sunshine period.

Tree Case	Air Temperature (K)	Rank	Velocity (m/sec)	Rank	Apparent Temperature (K)	Rank
CVCP/ TDC		3		2		3
TRCP		2		3		2
RC (SAF)		4		4		4
ACDC		1		1		1
	302 304 306 308 310 312		0.0 0.4 0.8 1.2 1.6 2.0		302 303 304 305 306 308	
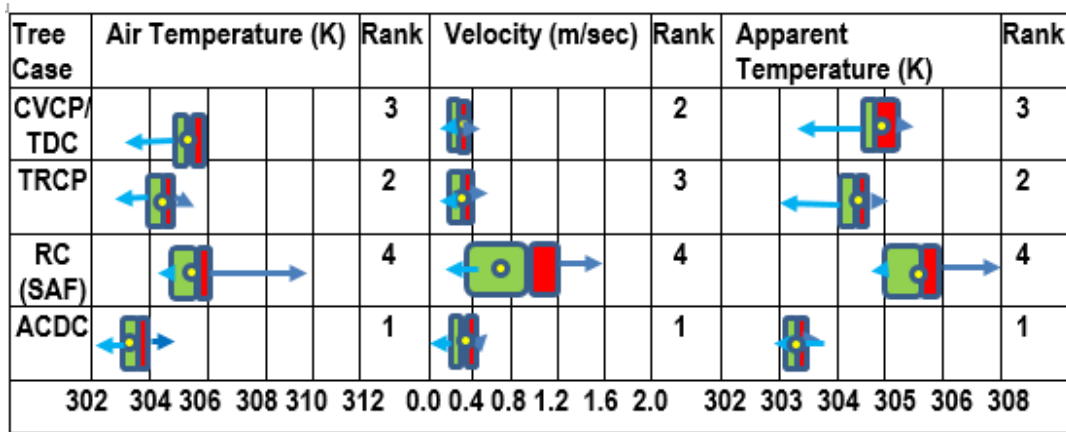
Figure 4.10: Boxplots for each scenario summarizing the maximum, minimum, median, average, and interquartile ranges of air temperature, flow velocity, and apparent temperature values simulated at 3 pm. Rank orders represent the cooling potential of scenarios based on TAVG values.

Figure 4.10 presents the boxplots for each scenario summarizing the maximum, minimum, median, average, and interquartile ranges of air temperature, flow velocity, and apparent temperature values simulated at 3 pm. This box plot is based on the data of discrete points, located only near or on the vegetation zones. The cooling potential of each scenario on in-canyon apparent temperature reductions is expressed as the difference between the reference case and the scenario in the same spot. When comparing rank orders (based on TAVG) from 1 (coolest) to 10 (warmest) (Figure 4.10); it is observed that the scenario with actual form drag shows the best thermal comfort improvement followed by transpiration rated cooling power scenario.

4.6 Impact of Morphological Characteristics of Tree Species

In this section, the potential of the tree species characterized by their morphological characteristics toward improving the comfort conditions of the urban area is investigated. Five scenarios have been modeled to simulate the impact of various tree configuration parameters (trunk height (TH), crown width (CW), crown height (CH), and leaf area density (LAD)) and are given in Table 4.3 as these parameters are highly correlated to the cooling capacity of trees [31].

4.6.1 Tree Classification Characterization Scheme

A generalized classification scheme based on four important structural parameters, assessed mainly by the landscape tree databank, is adapted [82]. Based on this scheme, five cases were compiled to model trees in Fluent. Each of the morphological parameters is subdivided into two classes: Foliage density (Sparse <=3, and Dense); Crown Height (Short vs Tall); Crown width (Narrow and wide <=9); and Trunk Height (High and Low<=2). For the selected species, a representative tree was sampled for direct measurement of their morphological characteristics (HT, TH, CH, and CW) and are mentioned in Table 4.2.

Table 4.2: Physical configuration of the studied tree species.

Sr. No	Species Name	Leaf Type	H_T (m) Avg	TH (m) Avg	CW (m) Avg	CH (m) Avg	LAD m^2/m^3	Canopy Shape
1	Guaiacum Offinate	Evergreen /	10	1.6	9	8.5	3.0	Spherical
2	Azadirachta indica	Evergreen	20	4	11	16	3.0	Paraboid
3	Peltophorim Paterocarpum	Evergreen	20	2	12	20	3.0	Paraboid
4	Bauhinia Blakeana	Evergreen	8.8	1.8	9.1	7	4.41	Spherical

In addition to common species, the effect of the Bauhinia Blakeana tree was also simulated with its improved LAD and has been proposed for plantation in Karachi for its capability of reducing temperature. The spatial variability of LAD along its crown

height for Bauhinia Blakeana tree is 0, 0.17, 0.30, 0.52, 0.87, 1.27, 1.28, 0.03, and 0 respectively. In Ansys FLUENT, vegetation is modeled as a porous zone incorporated with canopy shape correction i.e., form drag coefficient and heat transfer occur through its interaction with the surroundings through energy absorption and evapotranspiration.

Table 4.3: Description of tree species study cases.

Tree Case	Description	H_T (m) Avg	TH (m) Avg	CW (m) Avg	CH (m) Avg	LAD m^2/m^3	Cd
TC-1	Sparse LAD, Short Crown Height, Narrow Crown Width, low Trunk Height	9	2	9	7	3.0	0.2
TC-2	dense LAD, Short Crown Height, Narrow Crown Width, low Trunk Height	8.8	2	9	7	4.41	0.2
TC-3	Low LAD, Tall Crown Height, Narrow Crown Width, low Trunk Height	16	2	9	14	3.0	0.45
TC-4	Low LAD, Short Crown Height, Wide Crown Width, low Trunk Height	9	2	13	7	3.0	0.45
TC-5	Low LAD, Short Crown Height, Narrow Crown Width, high Trunk Height	11	4	9	7	3.0	0.35

It is pertinent to mention that Guaiacum Offinate is recognized with sparse foliage density, low trunk height, short crown height, and narrow crown width (TC1) while Bauhinia Blakeana is characterized with dense foliage density, low trunk height, short crown height, and narrow crown width (TC2). On the contrary, Azadirachta Indica is attributed to sparse foliage density, high trunk height, tall crown height, and narrow crown width (TC5) while Peltophorim Paterocarpum is recognized with sparse foliage density, low trunk height, tall crown height, and wide crown width (TC3/TC4).

4.6.2 Evaluation Results

The cooling potential is presented as 24-hourly average data (average over the whole circular domain) and discrete data (located on or near vegetation zones in the urban streets to exactly evaluate the localized effects of the vegetation) for the tree morphological scenarios at 3 PM. These time conditions are selected as the flow conditions are relatively stable at this time. The pattern almost follows the same trend for other periods.

It can be seen from the average data (Figure 4.11) that TC-2 characterized by the highest LAD provides the largest reduction in air temperature i.e. 1.2 °C followed by TC-3 (a reduction of 0.8 °C) when compared with TC-1 with the smallest LAD. Whilst TC-4 and TC-5 provide the smallest reduction in temperature (0.7 °C). The tree effectiveness varies throughout the day, owing to continuous change in shading and evapotranspiration rate.

A reduction of up to 4.0 °C in surface temperature occurs with street trees. This reduction results in low heat admittance by reducing the accumulation of solar energy in the urban area. This relatively small decrease relative to previous studies [97] owes to the use of single tree canopies and their comparatively small area relative to its surrounding. This relatively small temperature decrease is due to the modeling of a single line tree arrangement [106]. Such arrangement causes sharp advection of the warm air within the tree boundary layer forcing the cool air to penetrate surrounding environments [105]. LAD and crown height is the most influential in reducing the actual surface temperature which is due to the interception of large solar radiation rays by tree foliage as evident from diurnal variation in Figure 4.11 (b). There is a temperature difference of 3 °C to 4 °C between the tress having lower LAD and crown height (TC-1) and trees with greater height and higher LAD (TC-2) for 2 PM on 19th June. In reducing the surface temperature, Guaiacum Offinate appears to be the least effective. The tree species having high trunk height (TC-5) and crown width (TC-4) are least effective when compared with Bauhinia Blakeana (TC-2).

The density of vegetation inhibits wind flow affecting the aerodynamic performance of the trees. This has already been buttressed by study results of [97,115]. This lower velocity leads to improper ventilation and heat accumulation phenomenon below the canopy zone and windward/downward sides of vegetation and buildings. This decrease is due to increased roughness of urban surface with the addition of trees and its drag on airflow, which cause a smooth change in wind flow owing to pressure difference created as a result of porous trees [116]. Tree species with large LAD offer more resistance to the flow while a tree with a tall trunk offers the least (Figure 4.11 (c)). This provides better ventilation at all the monitoring locations due to low obstruction to wind flow at the pedestrian height, thus causing a significant improvement in thermal comfort. Tree species with large crown height (TC-3) and low LAD (TC-1) provides the intermediate ventilation.
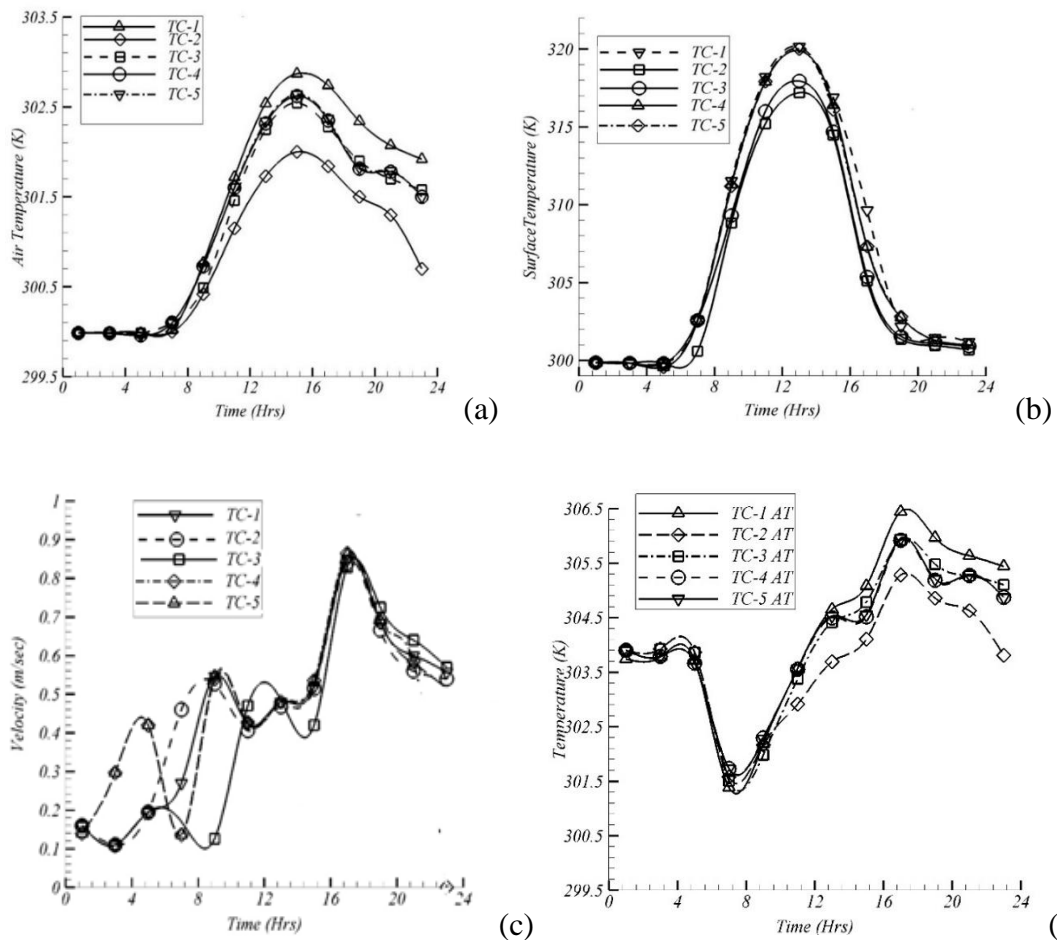
Figure 4.11: Results for species morphological characteristics, 24 Hourly distribution of (a) air temperature (b) surface temperature (c) velocity (b) apparent temperature.

Vegetation can be favorable for the urban microclimate since it tends to improve its thermal comfort [117] due to its ability to reduce radiation and promote air cooling despite decreasing the wind speed. Figure 4.11 (d) shows the thermal comfort improvement potential of different tree species in terms of apparent temperature variation. Bauhinia Blakeana (TC-2) is most influential in reducing the actual apparent temperature decrease at the pedestrian height when compared with Guaiacum Offinate (TC-1), owing to its great leaf area index and low height. Thus, irrespective of urban density, crown height and width are least effective for the improvement of thermal comfort.
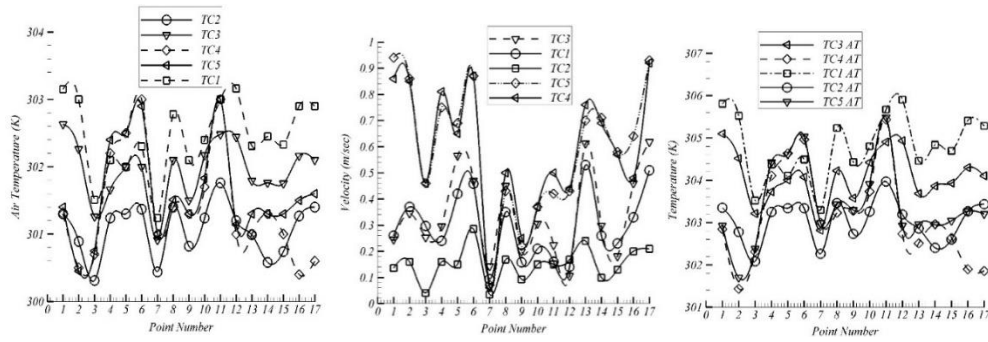
Figure 4.12: Results at discrete monitoring locations for species morphological characteristics, (a) air temperature (b) apparent temperature.

Figure 4.12 (a) shows the distribution of air temperature, velocity, and apparent temperature for the five aforesaid scenarios at various evaluation points. At the downwind located points (P4 to P7), the smallest temperature is observed with TC-2, followed by TC-3 and TC-1 while TC-4 and TC-5 provide the highest air temperature. At locations present on the downward side of the vegetation zones and surrounded by the nearby buildings (Points P8 to P15), TC-2 provides the largest decrease in air temperature followed by TC-4 and TC-3. TC-5 gives the largest increase in air temperature after TC-1 which shows the influence of H/W ratio (SVF) besides morphological characteristics of the tree. Overall, it can be observed that LAD is most influential in reducing the actual air temperature at the pedestrian height due to its solar offsetting capacity, as the ambient air temperature significantly decreases with the increase in LAD. However, this may not be an optimal solution as this also results in increased obstruction to the outgoing longwave radiation and the wind flow which can cause an increased loss of longwave radiation and a decrease in the heat removal through convection causing a rise in ambient air temperature [100,101].

Bauhinia Blakeana (TC-2), characterized by high LAD largely affects the flow velocity in downward and windward directions of the vegetation zone that is surrounded by low-rise and high-rise buildings (Figure 4.12 (b)). This is due to its obstructive nature, resulting in reduced ventilation across the area. This reduced wind speed causes heat accumulation (Figure 4.12 (b)). On the contrary, tree species with large crown width (TC-4) and large trunk height (TC-5) provide better ventilation at all the monitoring locations due to low obstruction to wind flow at the pedestrian height, thus causing a significant improvement in thermal comfort. Tree species with large crown height (TC-3) and low LAD (TC-1) provide intermediate ventilation.

The effectiveness of various tree species is different across the different densities of the studied microclimate and the trend of temperature variation is depicted in Figure 4.12 (c). Bauhinia Blakeana (TC-2) and Peltophorim Paterocarpum (TC-3) provide large comfort improvement at the pedestrian height in windward and downward directions which are surrounded by high-rise and low-rise buildings when compared to other tree species (Figure 4.12). At such locations, building shade outweighs the tree shading effect as witnessed in other previous studies [6,73]. In comparison, Guaiacum Offinate (TC-1) provides the least thermal comfort caused by a small decrease in air temperature due to its small canopy area. The apparent temperature at some spaces having low SVF is even lower than that of open spaces [118] which represents the dominant influence of shading over the effects of reduced wind speed. Likewise, in open areas which are considered as a suitable option for tree placement due to the absence of building shadowing effect, Bauhinia Blakeana (TC-2), Azadirachta Indica (TC-4), and Peltophorim Paterocarpum (TC-5) having large LAD, large crown width, and large trunk height are most effective in improving thermal comfort. This is due to their better ventilation capacity and shading as observed from monitoring points located in between the two vegetation zones (P 15 to P17). This observation is corresponding to studies of [6,73,119]. This suggests the planting of tall trees having large LAD irrespective of the urban density inside the studied microclimate.

Figure 4.13: Boxplots for each scenario summarising the maximum, minimum, median, average, and interquartile ranges of air temperature, flow velocity, and apparent temperature values simulated at 3 pm. Rank orders represent the cooling potential of scenarios based on TAVG values.

Figure 4.13 presents the boxplots for each scenario summarizing the maximum, minimum, median, average, and interquartile ranges of air temperature, flow velocity, and apparent temperature values simulated at 3 pm. This box plot is based on the data of discrete points, located only near or on the vegetation zones. The impact or cooling potential of each mitigation scenario on in-canyon apparent temperature reductions is expressed as the difference between the reference case and each mitigation scenario in the same spot. Table 4.4 summarize the maximum and average cooling potential for each mitigation scenario with respect to the existing conditions. When comparing ΔT_{MAX}, ΔT_{AVG} (Table 4.4), and rank orders (based on TAVG) from 1 (coolest) to 5 (warmest) (Figure 4.13); it is observed that the scenario of large LAD and large crown width shows the best thermal comfort improvement.

Table 4.4: Apparent temperature differences between each modeling parameter and the reference case representing the cooling potential of the implemented parameter.

	TC-1/ Vegetation base case	TC-2/ Large LAD	TC-3/ Crown Height	TC-4/ Crown Width	TC-5/ Large Trunk Height
Tavg	Reference	1.2	0.82	0.7	0.76
$\Delta T_{30, Daytime}$	4.1	10.4	7.7	6.68	6.82
Energy Saving W/m2	0.679	1.74	1.65	1.12	1.29

Equations 3.37 – 3.38 are adopted to access the energy-saving potential of street trees on 19 June 2015. The daytime period considered is 7 AM to 6 PM. It is evident from Table 4.4 that a reduction in average air temperature of up to 10.4 °C was observed, saving the cooling energy by about 1.74 W/m2 (1340 KWh) with representative isolated street trees. Air temperature reduction impacts the urban energy systems as lower temperature discourages the electricity demand, especially at peak time in terms of air-conditioning usage and building quality [18]. Such results however quite less than that of previous study results of [31,87] which is due to different morphological characteristics of trees and coverage ratio.

4.7 Discussion

The study demonstrates that thermal comfort conditions can be improved by reducing air temperature and surface temperature with the integration of street trees into the

urban environment. In this regard, comprehensive CFD analysis using finite volume method with and without applying vegetation is performed by solving URANS equations and by coupling heat transfer with wind flow for heatwave period (18-22 June 2015). The vegetation model used in this study is validated using the sub-configuration method as per CFD guidelines of Blocken [75] i.e. by replicating a previous experimental study [85] through a numerical approach for accessing the cooling effectiveness of street trees. The sub-configuration method is a widely used technique in urban physics as adopted by various authors in their studies [32,47,66]. The simulated air temperature is then compared with measurements and a good agreement is found with an average absolute temperature difference of 0.5 °C. Moreover, the unmitigated scenario is also modeled without proposed intervention to simulate the existing conditions and used as a reference case. The results of the reference case are validated against the Moderate-resolution Imaging Spectroradiometer (MODIS) satellite data as has been widely adapted to validate simulation results in urban microclimates [10,114,120,121].

The study has manifested that the application of street trees can effectively reduce the vulnerability of heat experienced by pedestrians along single streets. The results show that increment of street trees inside urban areas can reduce air temperature by 1.2 °C. This reduction is due to the blockage of sun shortwave radiation by the tree foliage and absorption of longwave radiation of the ground, a reason for decreasing the air temperature. This reduction is also due to the solar radiation interception through tree foliage and replacement of the surface with the shaded region below the tree canopy, thus having high moisture content and a higher surface water evaporation rate when compared with conventional materials. Similar to our results, previous researchers also showed air temperature reductions of up to 1.2 °C [46,97,117]. Street trees has also potential to improve thermal comfort conditions in real urban settings. The cooling effect is observed to be highly localized and found only in the immediate surroundings of tree zones [47]. The tree effectiveness varies throughout the day, owing to continuous change in shading [45,104] and evapotranspiration rate [45,47]. It is quite clear that air temperature reduction of 1.2 °C occurs with vegetation case when compared with built case and this maximum difference occurs in the early afternoon. On the contrary, a reduction is of 0.7 °C only with vegetation case as compared to open-space case. This decrease of temperature, then, impacts the urban energy systems as lower temperature discourages the electricity demand, especially at

peak time in terms of air-conditioning usage and building quality [18]. Urban heat mitigation also helps in savings of energy [8,31].

A reduction of about 4.0 °C in surface temperature occurs with the inclusion of vegetation as it results in low heat admittance by reducing the accumulation of solar energy in the urban area. This relatively small decrease relative to previous studies [88] owes to the use of single tree canopies and their comparatively small area relative to its surrounding [106]. Such arrangement causes sharp advection of the warm air within the tree boundary layer forcing the cool air to penetrate surrounding environments [105]. On the contrary, only a surface temperature reduction of 0.9 °C occurs with the vegetation case minus the built case and this maximum difference occurs in the early afternoon.

The cooling effect reverses at nighttime and is replaced with a warming effect close and in the vicinity of the vegetation zone for the case with vegetation and open space. At nighttime, cooling power becomes zero for all scenarios and all such cases receive the same amount of solar irradiance. When wind approaches vegetation zone and buildings, it gets obstructed by these elements, resulting in an alteration of flow characteristics. This change in flow variables then affects the heat transfer coefficient of the area as the result of the trapping of the dominant longwave radiations. This further affects the spatial exchange of heat which results in thermal discomfort [123,124]. This gives the beneficial effect of heating in vegetation wake if it is designed for such a purpose. This effect, however, does not appear when a comparison is made between the vegetation case and the built case. The reduction of air temperature, in this case, would be more apprehensive if it was simulated with the inclusion of longwave radiation between buildings and tree foliage as it might cause additional trapping of heat below the modeled canopy structure, especially at nighttime; thus, resulting in amplification of air temperature near to the vegetation zone. Unobstructed approach flow in the case with no representative buildings and vegetation results in greater heat transfer coefficient in street surface, thereby causing greater convective cooling owing to faster heat transfer rate so leading to lower nighttime temperature compared to build or vegetation case.

Vegetation also causes a decrease the flow velocities. This has already been buttressed by study results of [97,115,117]. This lower velocity leads to improper ventilation and heat accumulation phenomenon below the canopy zone and windward/downward

sides of vegetation and buildings. This decrease is due to increased roughness of urban surface with the addition of trees and its drag on airflow, which cause a smooth change in wind flow owing to pressure difference created as a result of porous trees [116].

Vegetation can be favorable for the urban microclimate since it improves its thermal comfort [117,125] due to its ability to reduce radiation and promote air cooling despite decreasing the wind speed. However, the UHI intensity by the vegetation coverage link to climatic zones and seasons [125].

4.8 Summary

Climate change and urban heat island (UHI) effects are increasing heat stress and adversely impacting outdoor thermal comfort in urban areas. Vegetation is one of the most effective strategies to alleviate the adverse effects of rising outdoor temperatures. However, trees, depending on their morphological characteristics, have the variable potential for the regulation of thermal comfort. Therefore, a holistic understanding of tree planting with respect to the particular climate is necessary for urban sustainability. In this chapter, computational fluid dynamics (CFD) simulations have been performed to analyze the effect of two vegetation modeling parameters and four morphological parameters of different tree species on the overall cooling potential in a real urban area. The thermal comfort conditions are examined at pedestrian height by evaluating four climatic parameters: the reduction of ambient air temperature, surface temperature, and apparent temperature; the alteration of airflow velocity. The results are compared for the aforementioned scenarios; vegetation case, built case, and open space case; effect of vegetation modeling parameters; and effect of different morphological characteristics. Moreover, validation study for vegetation model is carried out with a sub-configuration method based upon previous experimental studies.

The study shows that consideration of more realistic values of these parameters yields significant variation in the determination of cooling potential and flow characteristics developed by the applied vegetation. The vegetation modeled with actual form drag coefficient and transpiration rate provides better thermal comfort as it results in low apparent temperature. Of all morphological characteristics, leaf area density (LAD), crown width, and trunk height are found to be most influential in providing thermal comfort, irrespective of the type of climate and urban density

Effectiveness of Water Bodies

5.1   Introduction

Water bodies are among the most effective means to alleviate UHI and improve the thermal comfort of urban microclimates. In this study, the cooling effect of water bodies in isolated streets has been analyzed using computational fluid dynamics (CFD) under real urban hot humid climatic conditions. The water body model used in this simulation is first validated with experimental data from a previously published study. Before simulating the water bodies' effectiveness, a base case simulating the existing conditions is modeled which serves as a reference case for predicting the water effectiveness and for identification of locations to propose representative water bodies. The cooling effect is analyzed in the form of contours at pedestrian height ($z =1.5$) and as 24-hourly average data. The average data is selected based on the finding of previous studies rather than maximum and minimum values. This is attributed to a variety of canyon characteristics inside urban areas where shades of the buildings and exposure to direct solar radiation affect the temperature reduction/increase in different magnitudes [122,123]. Water bodies, in the context of sustainable urban development, have shown significant potential towards alleviating the UHI due to its high thermal and evaporative cooling capacity.

5.2   Validation of the evaporation from a small-scale water surface

The validation study for modeling the thermal effect of water on the surrounding environment was also performed by employing heat flux at the water surface The wind tunnel experiment data of Kato and Nakane [126] is taken as reference. He examined the basic mechanism of evaporation from the water surface in the wind tunnel by maintaining steady-state conditions. For this validation, steady-state simulations were performed and compared with the measured data. The computational domain is modeled as per the actual wind tunnel domain which has a dimension of 3 m x 1 m x 0.98 m along streamwise, lateral, and vertical sides respectively. The water depth is 20 cm. The domain discretization contains a structured mesh with 50, 20, and 60 cells along x, y, and z dimensions (Figure 5.1 (a and b), and meshing was performed in the

Pointwise [93] . The wall adjacent cell height was kept at 0.005 m. The computational domain has one inlet, one outlet, and symmetry at the top and lateral sides. The bottom of the ground was assigned as a wall with water at a temperature of 16 °C. At the inlet, the profile of turbulent properties and velocity was assigned according to equations 3.39-3.41 with U_{ref} as 3 m/s and h_{ref} as 0.3 m. The air inlet temperature and humidity of 20 °C and 8 g/kg respectively were used. The results are compared in normalized form with these values as reference.

Figure 5.1 (c and e) shows the comparison of CFD results with wind tunnel data in terms of air temperature and mass fraction while Figure 5.1 (d and f) shows the regression analysis results for these two variables. The comparisons have been made for two different heights above the water surface. The results show a gradual decrease in temperature and a gradual increase in humidity along with the flow directions. Ansys and ENVI-met tend to overestimate the temperature and under-evaluate the humidity. Such behavior of CFD tools has also been highlighted by [127,128]. This effect is profound near the water surface owing to relatively low velocity near the surface. The CFD-based temperature profile is quite consistent with the results of a wind tunnel without a significant difference between the two approaches at certain points. However, the CFD simulation showed only a moderate agreement for humidity. However, the primary focus is on the temperature computation for which a reasonable/fair agreement between the measurement and simulated data is considered satisfactory for validation. It can be observed that a good agreement exists between the surface temperatures of the two approaches as R^2 value is quite close to 1 (Figure 5.1(d and f)).
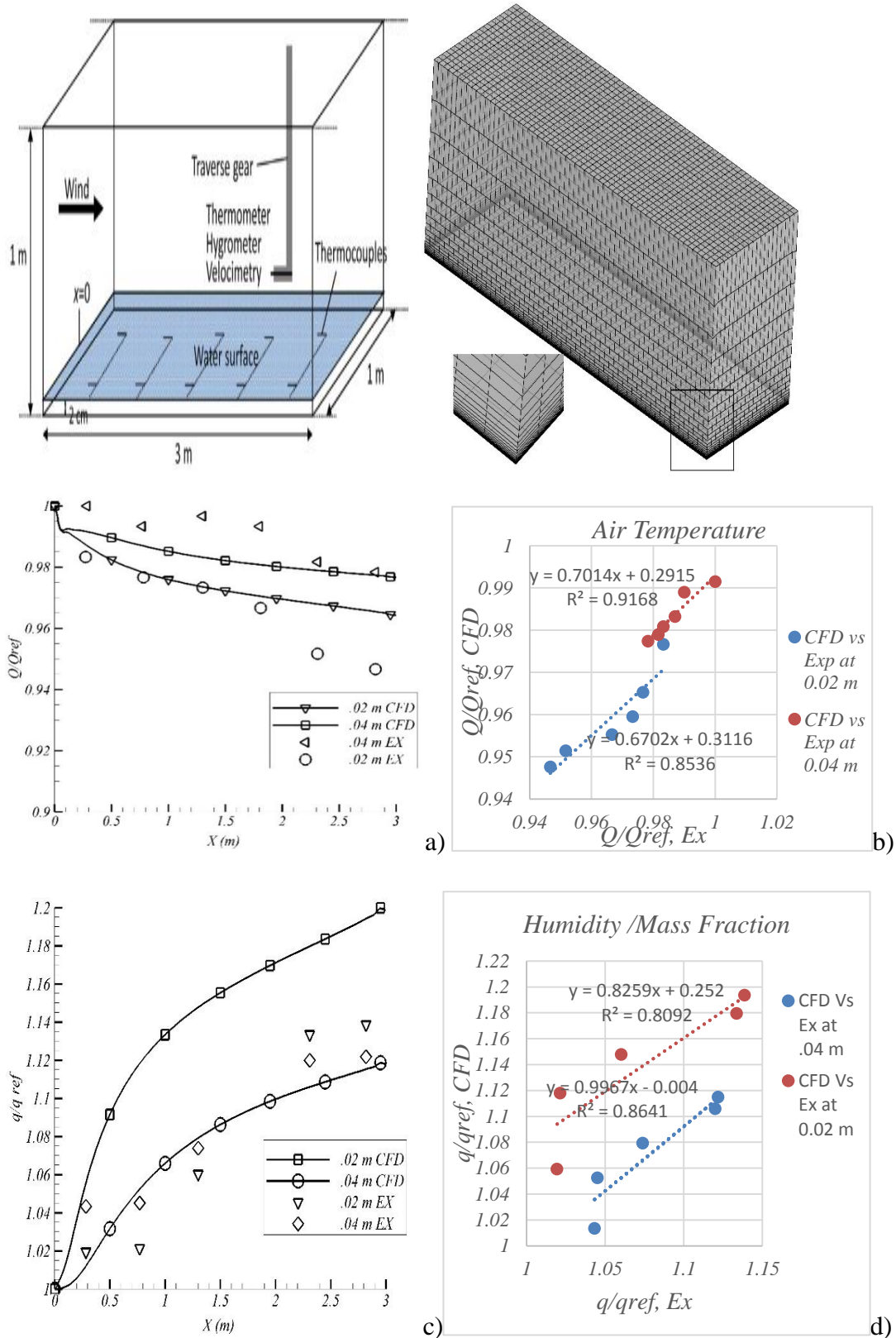
Figure 5.1: a) Original model b) discretized model (c and d) Comparison of air temperature between CFD and Tominaga study along with regression analysis. (e and f) Comparison of relative humidity along with regression analysis.

5.3   Impact of Water Bodies

5.3.1   24-hourly Distribution

The impact of water bodies on their cooling potential inside the studied microclimate is presented and discussed here. Figure 5.2 illustrates the 24-hourly distribution of air and surface temperature for the two cases. From Figure 5.2 (a), it can be observed that applied water intervention provides a large decrease in ambient air temperature when compared with simple flow calculation. Moreover, the cooling effect is prominent throughout the day and is at its peak at midday when the sun is overhead i.e., the solar radiations are abundant. It causes more energy for evaporation, latent heat generation instead of sensible heat thus causing more cooling effects [64].
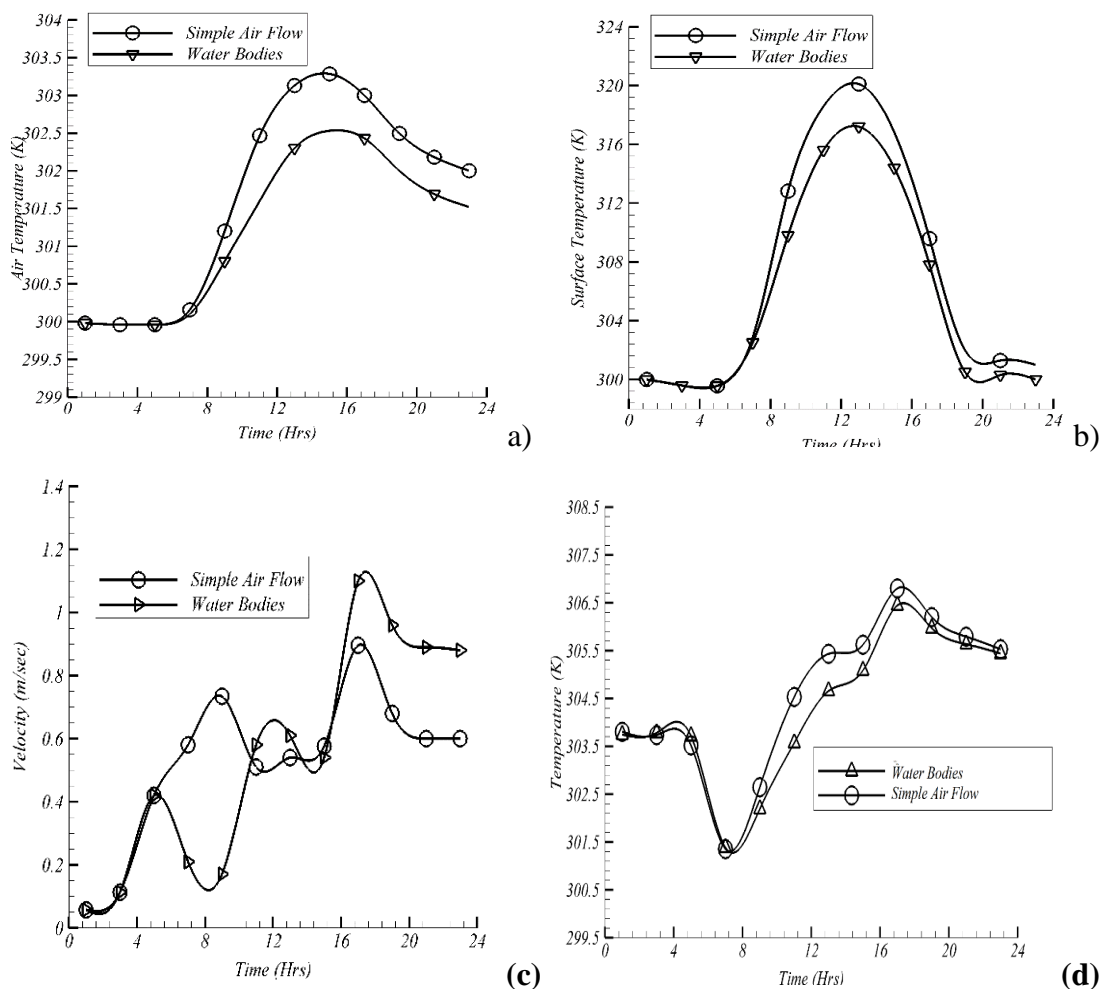
Figure 5.2: 24 hourly distribution of (a) air temperature (b) surface temperature c) flow velocity d) apparent temperature.

The air temperature increases gradually without water from 7 AM to 2 PM then gradually decreases after reaching a peak of 30.25 °C at 2 PM. With water, the average

temperature decreases from 30.25 °C to 29.15 °C. This is because the water causes the rise in airflow velocity promoting the heat convection between air and surroundings, thus resulting in evaporative thermal dissipation. This causes temperature gradient to develop between the water surface and air along with atmospheric turbulence causing negative sensible heat flux which promotes the cooling effect. Such a decrease in water bodies has also been reported in previous studies [22,64,129]. Figure 5.2 (b) shows that surface temperature decreases due to the presence of water bodies. This decrease of up to 3.8 °C temperature is attributed to water thermal capacity which promotes the absorption of the incoming solar radiation. This increases the latent heat by reducing the sensible heat for the surrounding. Figure 5.2 (c) shows that flow velocities increase with the addition of water bodies.

It is evident from Figure 5.2 (d) that water contributes to providing greater thermal comfort conditions inside the studied microclimate despite the increase in humidity values. The greater effect is at its peak at the time of higher solar irradiance. The largest effect is observed in terms of apparent temperature reduction of 1.2 °C and 1.0 °C when compare with simple airflow for LST 1100 and 1200 hrs respectively.

On the contrary, a reduction is of 0.7 °C only with vegetation case as compared to open-space case, which impacts the urban energy systems as lower temperature discourages the electricity demand, especially at peak time in terms of air-conditioning usage and building quality [18]. Urban heat mitigation also helps in savings of energy [8,31].

5.3.2 Temperature Distribution (Horizontal and Vertical)
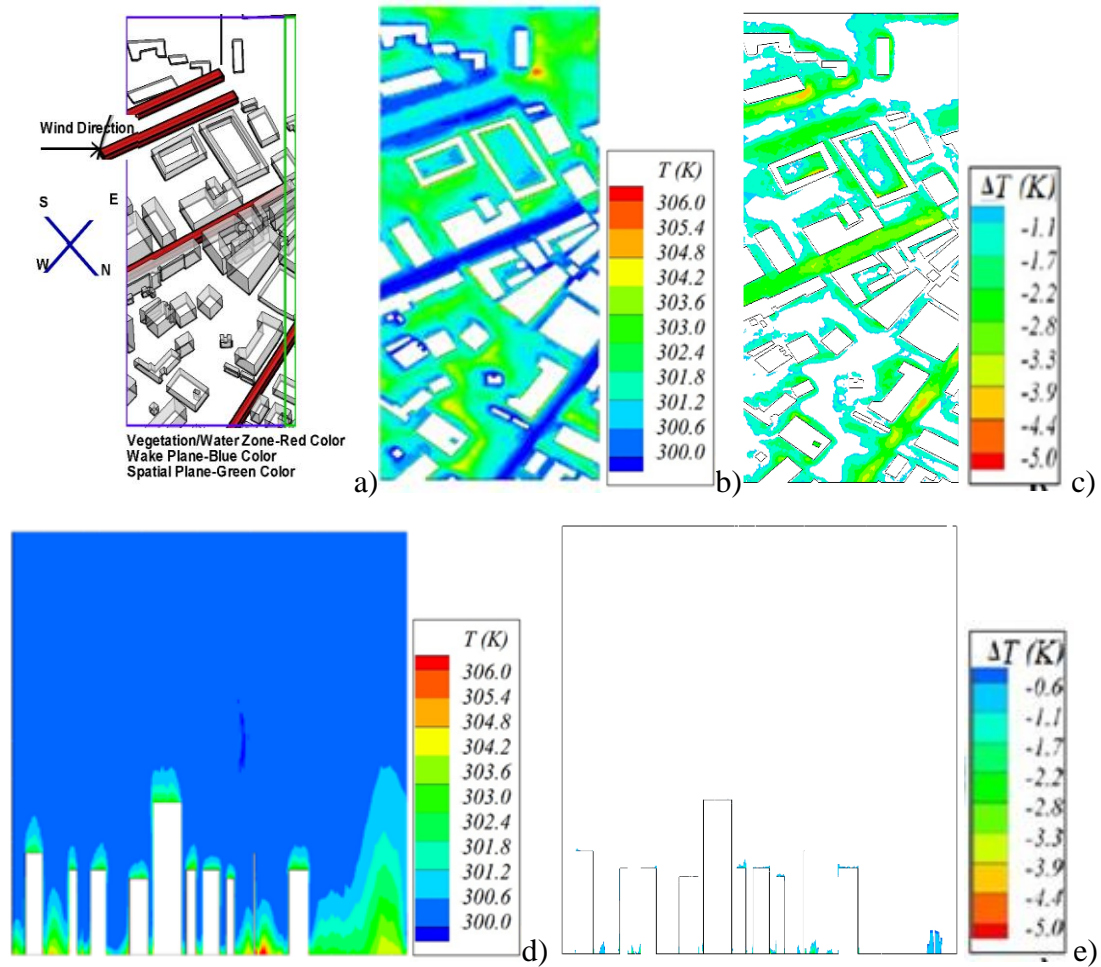
Figure 5.3: a) Representation of wake and vertical plane b) Contours of air temperature at wake plane for water bodies, 1500 LST, 19 June 2015 c) Contours of air temperature difference, water minus SAF at wake plane (d) Contours of air temperature for water bodies at vertical plane e) Contours of air temperature difference, water minus SAF at the vertical.

The horizontal and vertical distribution of the cooling effect of water is reported for 1500 LST, 19 June 2015 (Figure 5.3). The water area possesses a bit lower temperature as compared to the surroundings due to its thermal capacity as shown in Figure 5.3 (b). This causes the development of a slight water surface to air temperature gradient causing negative sensible heat flux to grow. Moreover, in such isolated streets, advection and urban geometry have considerable effects on the mitigation effectiveness (temperature reduction) at such locations. This attributes to hot air channeling through these street aisles/canyons from surrounding areas owing to temperature and pressure differences [25,130]. With water, the intensity of cooling is 1.1 °C (Figure 5.3 (c)). The results are quite comparable with those of [131–134]. This

effect is insignificant in crosswind spatial direction as evident from Figure 5.3 (d and e). As the wind direction is along the water zone direction, the effect attributes to lateral dispersion of cooling effect which is quite lesser than advection in crosswind direction. Also, the water bodies with their slimline arrangement are too small to disperse the cooled air to their surroundings.

5.3.3 Flow Velocity

Figure 5.4 (a) shows the diurnal variation of the average flow velocities on an hourly basis for the cases with and without water. It is evident from the graph that flow velocities increase with the addition of water bodies. This large velocity leads to proper ventilation and results in a low heat accumulation phenomenon. The velocity increase only appears over the water region (Figure 5.4 (b and c) and is attributed to a temperature difference between the water and waterless ground due to its high thermal capacity which promotes wind flow. Velocity also increases due to the blockage of wind by the building surfaces owing to their larger roughness than water. This increase in velocity is consistent with the study results of a previous study [22,135]. However, the velocity increase effect is quite less in crosswind directions as clear from Figure 5.4 (d and e).
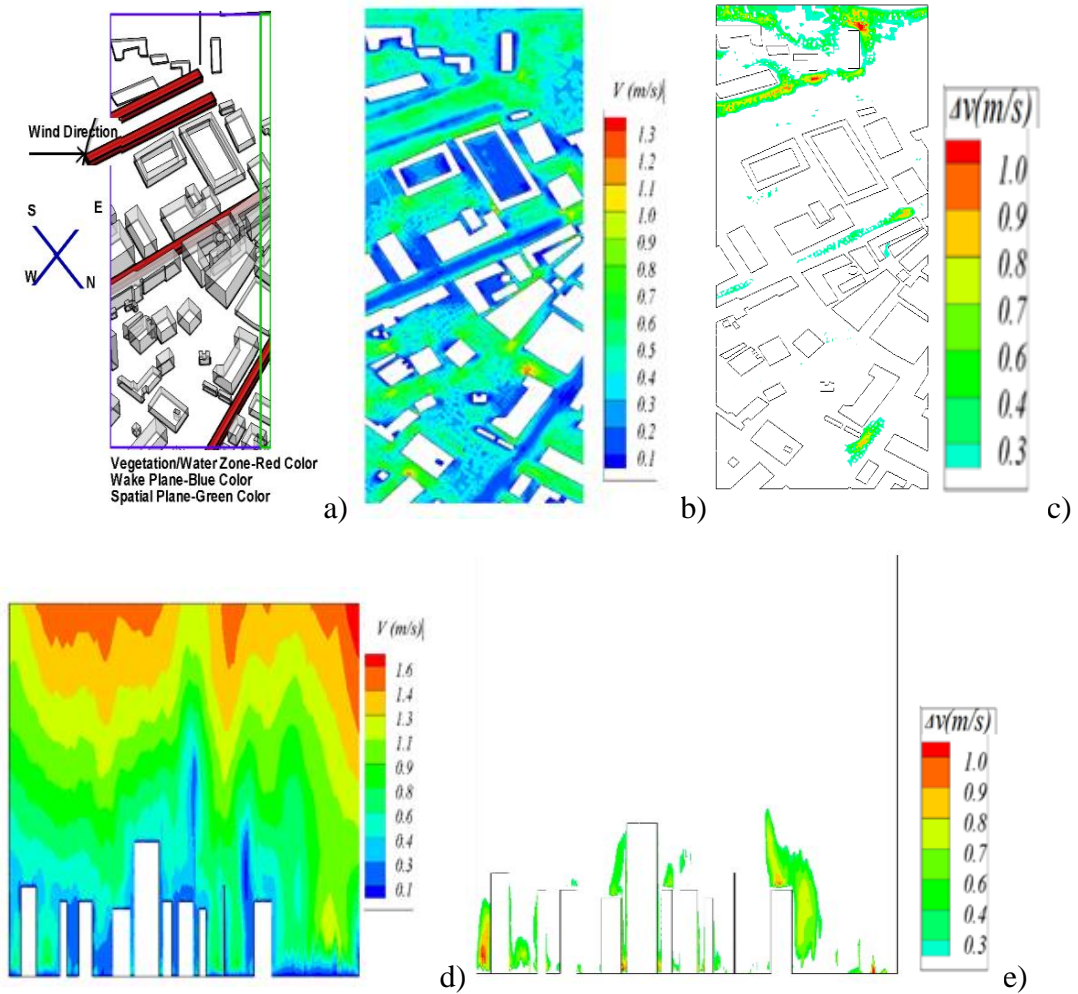
Figure 5.4: a) 24 hourly distribution of velocity b) a) Representation of wake and vertical plane b) Contours of wale velocity with water bodies, 1500 LST, 19 June 2015 c) Contours of wake velocity difference, water minus SAF d) Contours of velocity with water bodies at vertical plane e) Contours of velocity difference, water minus SAF at the vertical plane.

5.4 **Summary**

Climate change and urban heat island (UHI) effects are increasing heat stress and adversely impacting outdoor thermal comfort in urban areas. Water bodies are among the most effective means to alleviate UHI and improve the thermal comfort of urban microclimates. In this study, the cooling effect of water bodies in isolated streets has been analyzed using computational fluid dynamics (CFD) under real urban hot humid climatic conditions. The thermal comfort conditions are examined at pedestrian height and diverse vertical levels by evaluating three climatic parameters: reduction of ambient air and surface temperatures, change in air velocity; and reduction of apparent temperature.

Two different scenarios (one with a realistic setting and the other with a representative water body) were studied and the results show that, for isolated streets, the water bodies can effectively improve thermal comfort conditions by reducing ambient air temperature (i.e. a reduction of 0.9 °C), surface temperature by 3.5 °C, and apparent temperature by 1.2 °C respectively. Moreover, a significant increase in the wind velocity was also observed reaching its maximum value at the time of high solar irradiance. The water bodies considered have almost similar properties across the globe. This suggests that even though the case study is local, the findings and recommendations can be applied to other parts of the world having a blue landscape of any physical configuration and urban climate. The magnitude of thermal impact, however, may vary due to differences in prevailing weather conditions and urban morphology. Moreover, the study is expected to inform architects regarding retrofitting mitigation of UHI with the blue landscape.

Chapter-6

Effectiveness of Cool Materials

6.1   Introduction

To evaluate the effectiveness of the mitigation measures toward UHI alleviating and improving the urban thermal environment, cool material strategies in single and in combination are explored and results are compared with a "Reference Case (RC)" which is modeled without incorporating any bioclimatic interventions. In this regard, the cases tabulated in Table 6.1 were studied.

Table 6.1: Retrofitting Mitigation Simulation Cases.

Sr. N	Scenario	Materials	Bioclimatic Interventions	Case Name
1	Cool Materials only	Cool Material on Buildings only	Cool Materials	CMB
		Cool Material on Grounds only		CMG
		Cool Material on Both Buildings and Ground		CM
2	Combined Cool Materials and Vegetation	Cool/Reflective Materials	Vegetation	CMCV
3	Combined Cool Materials and Water Bodies	Cool/Reflective Materials	Water Bodies	CMCW

First, cool materials as an individual strategy are explored in which conventional materials are replaced with cool ones. The entire urban surface is split into streets, roofs, and vertical envelopes. After careful consideration, one value for each component is selected, giving a variety of albedo values for possible urban surface materials. The literature also reports a homogenous value for cool surfaces, usually ranging from 0.6 to 0.8. However, we selected 0.67 for all components as an average value among the gathered ones to incorporate a possible realistic value, as adapted by [71]. Simulations involving cool materials scenarios were carried out with their application on grounds (CMG), buildings (CMB), and ground and buildings (CMGB). Since Cool materials present a high reflectance in the visible, near infra-red (NIR), or

the global solar spectrum, combined with a high thermal emissivity so some materials (white clay) also can contribute to increased intensity of reflected UV radiation [136]. Such UV radiation is usually detrimental to the living cells; thus often causes sunburn and a fast rate of skin aging (Canadian Center for Occupational Health and Safety. 2008.). Therefore this study assumes to model proper advanced cool materials which can absorb visible part of the spectrum but with high reflection in the near-infrared part to vouchsafe no health risk [138]. Optical degradation/aging due to dust/atmospheric constituents deposition on their surfaces (limitation of this study) may affect significantly their cooling/mitigation performance [139].

Next, the effectiveness of combined cool materials and representative vegetation is examined using computational settings as described in sections 3.1, 3.2 and user-defined functions for vegetation source terms (given in Appendix-B.)

In the last, the combined thermal performance of the representative water bodies with cool materials reflectance is examined by incorporating water heat flux (given in Appendix-B).

6.2 Impact of Cool Materials

6.2.1 Hourly Distribution of Air and Surface Temperature

Applying cool materials on both ground and building surfaces provides large ambient air temperature and surface temperature decrease when compared with reference case results due to their ability to reflect large solar radiation and emit thermal heat into the environment (Figure 6.1).
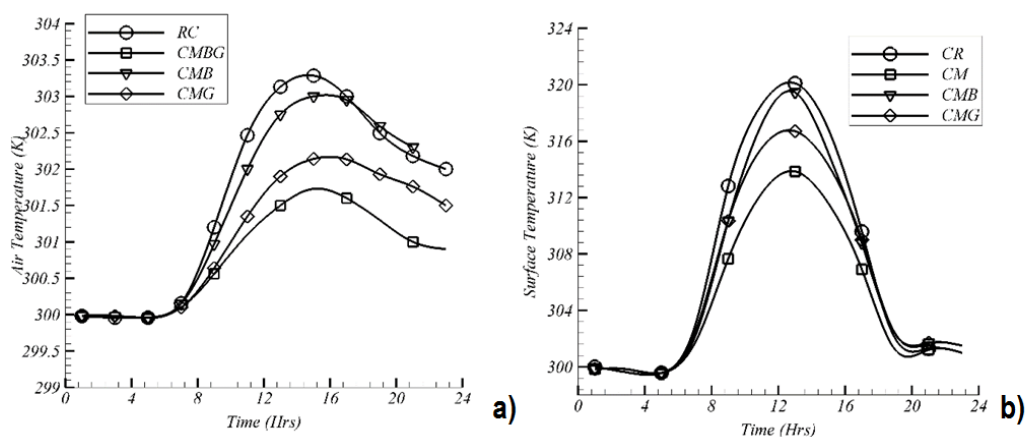
Figure 6.1: Impact of cool materials on area-averaged twenty-four hourly distribution of (a) air temperature (b) surface temperature.

In the "reference case-CR" (Figure 6.1(a), the air temperature increases gradually from 7 AM to 2 PM then gradually decreases after reaching a peak of 30.25 °C at 02 00 PM. After the application of cool materials either on the ground (CMG) or building (CMB) or both (CM), the trend of the air temperature is consistent with that of conventional materials (CR) but its severity decreases. This is attributed to the reason that conventional materials absorb more amount of solar radiation which would greatly increase the air and surface temperature. The largest reduction in air temperature achieved with all cool surfaces is about 1.5 °C as compared to typical conventional materials. This reduction is then followed by cool grounds (a reduction of 1 °C) and cool building only (a reduction of 0.3 °C) as shown in Figure 6.1 (a). These temperature reductions are in agreement with the study results of [12,69,71,140].

Figure 6.1 (b) shows that cool materials are also helpful in countering surface temperature increase and this mitigation effect (reduction of about 8 °C) becomes more pronounced when they replace both buildings and ground materials as they possess high reflectance which modulates the heat gains which results in low surface temperature. Moreover, cool materials cause a small release of sensible heat which causes cooling through the convection process. This reduction of surface temperature with cool materials is in line with previous study results [69,140].

6.2.2 Spatial Distribution of Mitigation Intensity
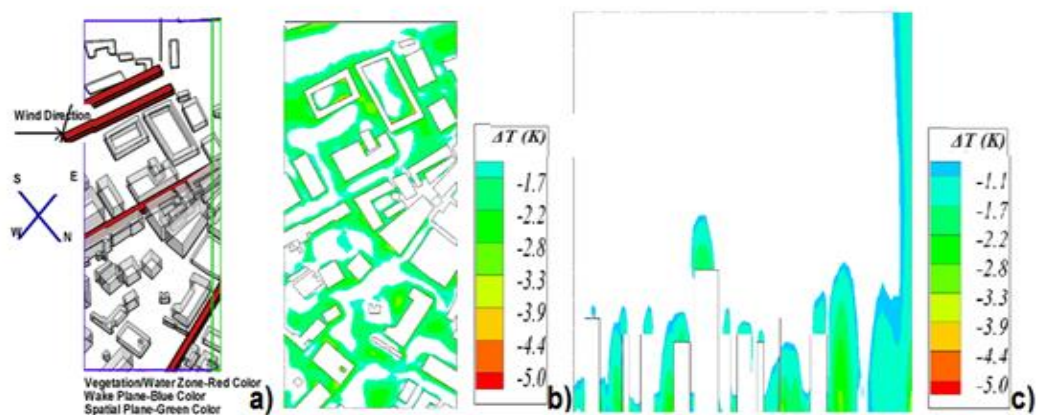
Figure 6.2: a) representative wake/vertical plane; Contours of air temperature difference for 15 00 hrs, between CM and CR (b) horizontal (c) vertical.

Figure 6.2 (a) depicts the horizontal and vertical distribution of mitigation intensity caused by cool materials. It has been observed from Figure 6.2 (b) that the cool

material case causes a larger reduction in air temperature at the pedestrian height as compared to the reference case owing to large solar reflectivity and high emission of accumulated heat because of their high emissivity. The intensity of the temperature reduction at pedestrian height by using both cool materials is 2 °C. This reduction in air temperature with all cool surfaces is less explicit in vertical directions as shown in Figure 6.2 (c).
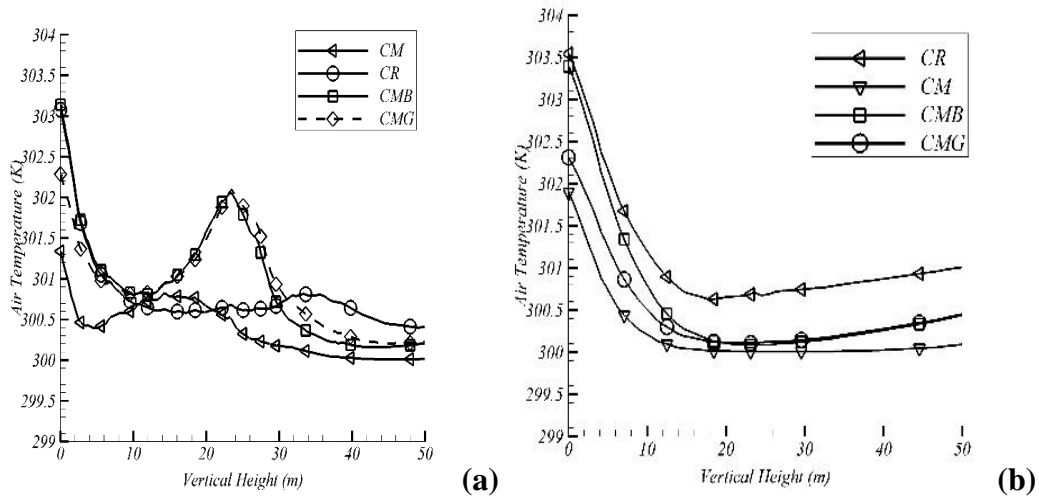
Figure 6.3: Vertical distribution of air temperature at (a) P-2 b) P-6.

The vertical distribution of the mitigation effectiveness of cool materials is also investigated at different monitoring points (Figure 6.3) to monitor the effect of urban morphology on the material albedo for 15 00 hrs, 19 June 2015. The effect has been examined at four different locations and a comparison has been made between all cool material scenarios. It is observed that at Point P-6 and P-7 as shown in Figure 6.3 (b), replacing both conventional materials with cool ones provides the highest heat reduction followed by ground cool materials and then building cool materials. Cool materials often cause an increase in ambient air temperature due to the trapping of radiations at a certain dense location such as point P-2 (surrounded by low-density high-rise buildings) as depicted in Figure 6.3 (a). To make cool/reflective materials more effective for all urban densities, it is suggested to implement them in combination with other measures such as street trees to counteract the increased ambient temperature resulting from simple cool materials.

6.2.3 Flow Velocity
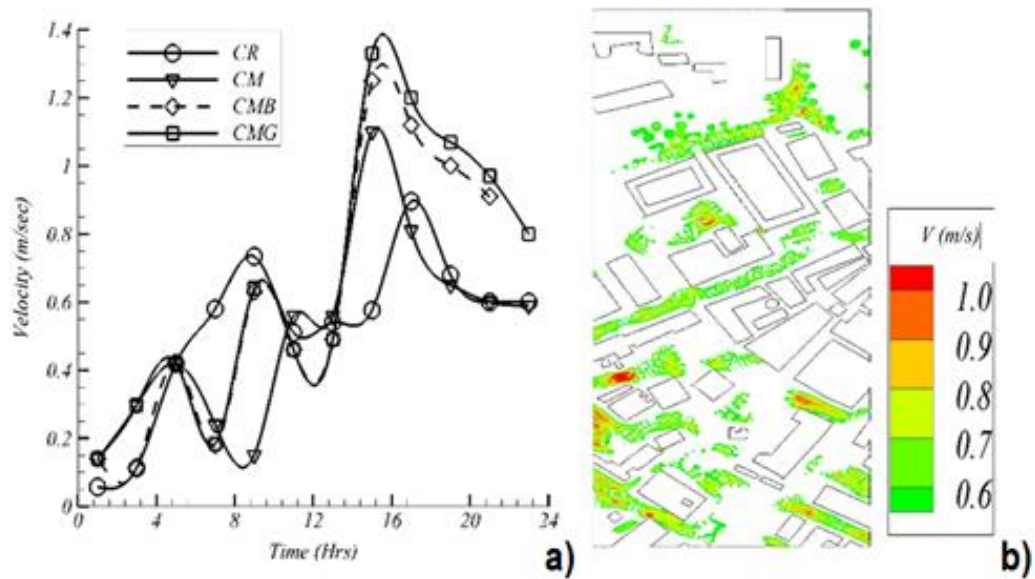
Figure 6.4: a) Twenty-four-hourly distribution of velocity 19 June 2015 b) contours of velocity difference, CM minus CR.

The graph in Figure 6.4 (a) provides the twenty-four hourly variations of average flow velocities for the case with and without cool materials. It is well evident from the graph that flow velocities increase with the addition of cool materials. Since the surface roughness of the element is the same, but a higher temperature gradient-lead to pressure difference between air masses so the resulting velocity results are higher. For the wake velocity contours difference Figure (6.4 b), there is a difference is of 0.5 m/sec for CM minus CR. Wind velocity is significantly increased in spacious areas rather than building vicinity which is because of large temperature difference in these areas which effectively promotes wind flow.

6.3   Impact of Cool Materials Combined with other Interventions

6.3.1   Twenty-Four Hourly Distribution of Air and Surface Temperature

Cool materials when combined with other interventions are more effective in promoting the thermal environment as they provide a large reduction in ambient air temperature when compared with reference case as depicted from Figure 6.5 (a). Combined cool materials with vegetation (CMCV) provide the largest reduction in ambient air temperature as clear from Figure 6.5 (a). This is due to their combined mitigation effect as the vegetation provides the shade/moisture content and interception of solar radiation which together with low absorption of solar radiation

and low heat storage due to cool materials, results in lower emission of longwave radiation to the surroundings thus reducing the large air temperature. This decrease in air temperature is in agreement with the study result of [125,141] involving cool materials combined with vegetation. CM is the second-best scenario.

Combined cool materials with water bodies (CMCW) are then the next best scenario as cause a substantial reduction of 2 °C when compared with conventional materials. This is due to their combined effect as the cool materials absorb fewer radiations resulting in a decrease of surface temperature which lowers sensible heat transfer to air, which together with less storage reduces vertical temperature gradient. This reduction of temperature gradient increases more latent heat caused by water evaporation which further decreases the sensible heat and storage flux, resulting in more decrease in air temperature. Moreover, the temperature reduction is prominent at Noon. It causes more energy for evaporation, latent heat generation instead of sensible heat thus causing more mitigation effects [64].
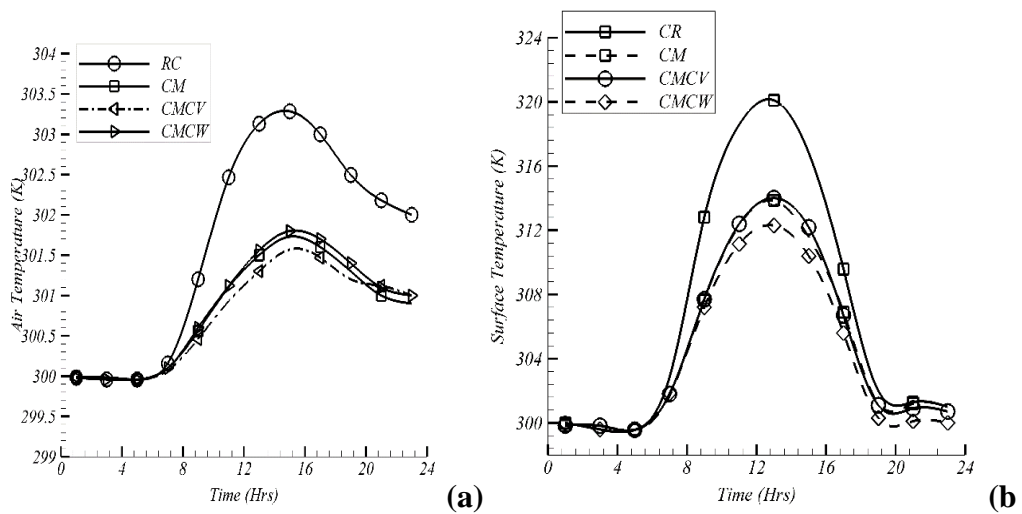
Figure 6.5: Twenty-four-hourly distribution for (a) air temperature (b) surface temperature.

A decrease of about 9 °C in surface temperature is observed with CMCW and this occurred at 12 00 hrs (Figure 6.5 (b). The second-highest reduction of 6 °C each observed is observed with CM and CMCV.

6.3.2 Spatial Distribution of Cooling Effect
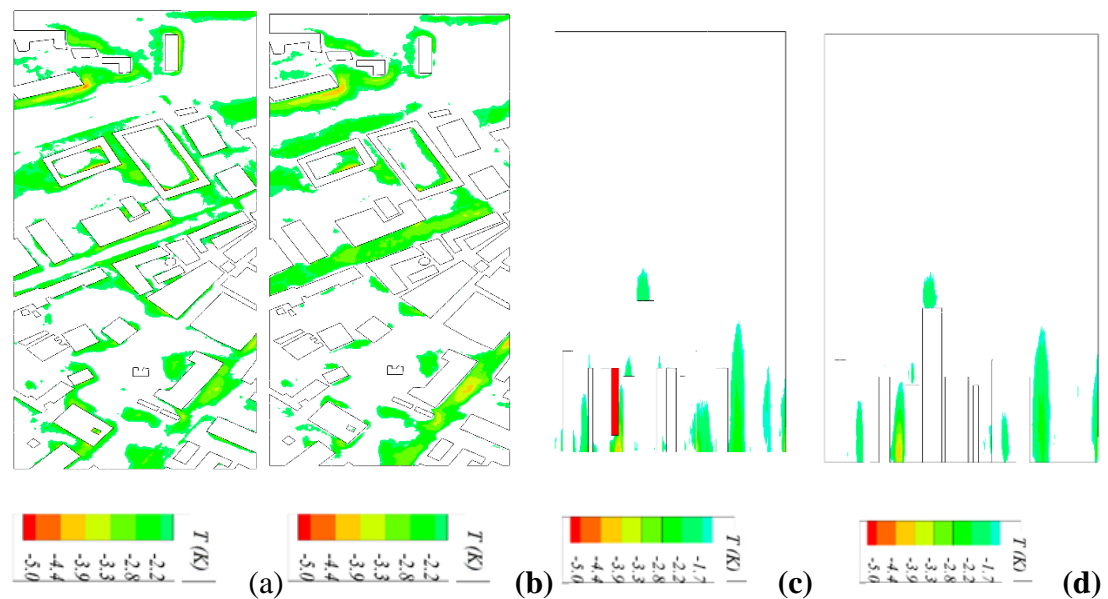
Figure 6.6: The contour of air temperature difference in horizontal and vertical directions for 15 00 between, (a and c) CMCV-CR (b and d) CMCW-CR.

The intensity of the cooling (mitigation) effect is appraised at a pedestrian height which is based on the highest difference of air temperature present outside of the vegetation zone (Figure 6.6). In the case of cool materials combined with vegetation (CMCV), the mitigation effect is more abundant near the vegetation zone and in the region fenced by the buildings as clearly depicted in Figure 6.6 (a and c). It is more intense in the area which is surrounded by the medium/high rise buildings owing to low wind velocities in these regions and high reflectance of solar radiation as high albedo materials were used. The intensity of the cooling effect with vegetation with and without cool materials is 2 °C at pedestrian height. The study results in the form of a maximum average reduction in air temperature obtained with tree vegetation echo with the results of previous CFD studies by [125,141] and the measurement study by [142,143]. Nevertheless, this potential of vegetation for mitigating the UHI depends on climatic zones and seasons [125].

For the case of water with and without cool materials, the mitigation/cooling effect is only present at isolated streets from Figure 6.6 (b) which is usually attributed to higher wind velocities, resulting in swift lowering of the surface temperature because of the large spatial exchange of heat. The intensity of the mitigation effect with CMCW is 2.5 °C. The heat mitigation intensities with all these proposed measures prove their effectiveness toward improving the thermal comfort of urban microclimate [117,125].

However, the intensity of the mitigation effect in the vertical direction is 1.5 °C as shown in Figure 6.6 (d). This very insignificant effect in crosswind spatial direction attributes to lateral dispersion of mitigation effect which is quite lesser than advection in crosswind direction as the wind is along the water zone direction. Also, the water bodies with their slimline arrangement are too small to disperse the cooled air to their immediate surroundings.
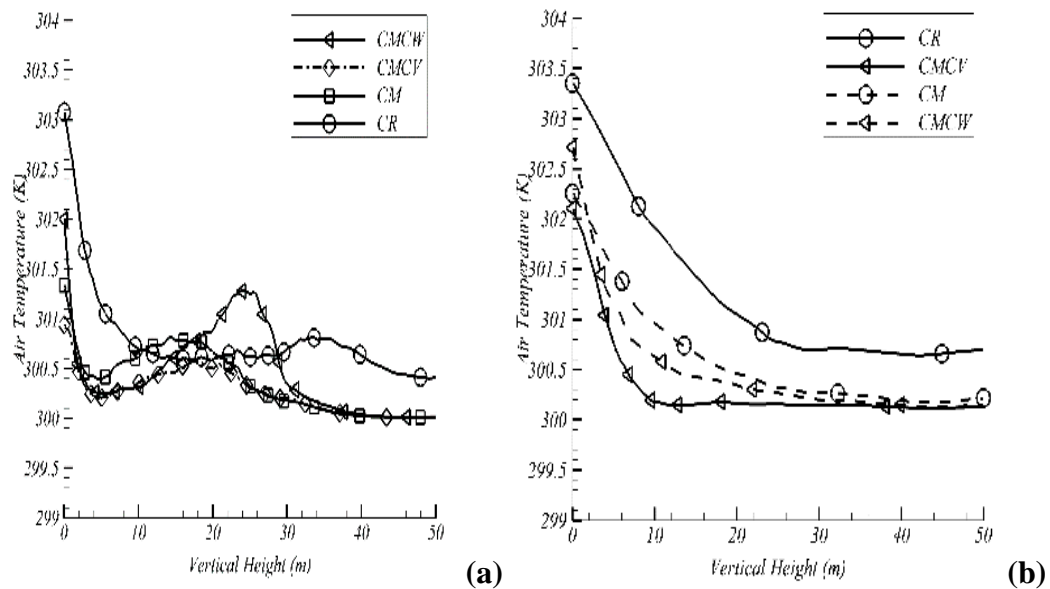
Figure 6.7: Vertical distribution of air temperature (a) P-2 b) at P-3.

The vertical distribution of the cooling effect of cool materials with and without other interventions is also investigated for 15 00 hrs, 19 June 2015 at two evaluation locations (P-3 and P-2) (Figure 6.7). The mitigation (cooling) effect is more pronounced at lower height i.e., near to ground due to the presence of cooler and denser air due to convection and long resident time of this comparatively concentrated air due to low wind velocities near to the ground. On the contrary, cooler air becomes diluted at higher heights and various types of source terms affect the transpiration cooling vertically. It is clear from Figure 6.7 (b) that at Point P-3 (in between two water zones), CMCW provides the highest reduction followed by CM while the least reduction is observed with CR. The mitigation effect increased sharply with the application of a water body at a lower height. This is due to the water surface temperature gradient causing negative sensible heat flux at a lower height.

At Point P-2 (in between the vegetation/water zone and the buildings), the ambient temperature for all cases except CMCV starts increasing after decreasing up to a height of 10 m due to trapping of reflected radiation (Figure 6.7 (a)). This is also due to the

low sky view fraction of urban area at this location and the small deflection of solar radiations (building shading effect). More it can be seen from Figure 6.7 (a) that CMCV can be able to reduce air temperature which was increased by using cool materials only at the P-2 location. Thus, cool materials combined with vegetation (CMCV) are helpful in significantly reducing the ambient air temperature and in managing the increased reflected solar radiation caused by materials having high albedo values. The foliage of trees also provides shade besides increasing latent heat through the evapotranspiration process, which shields the incoming solar radiation, thus regulating the microclimate by controlling both direct and reflected shortwave radiation.

6.3.3   Flow Velocity

The density of vegetation inhibits wind flow [47,97] causing a decrease of an average of 0.5 m/sec. This decrease is due to increased roughness of urban surface with the addition of trees and its drag on airflow, which cause a smooth change in wind flow owing to pressure difference created as a result of porous trees [116]. This lower velocity leads to improper ventilation and heat accumulation phenomenon below the canopy zone and windward/downward sides of vegetation and buildings. This lower wind velocity and deficit ventilation cause the flow rate to increase for upstream urban heat island circulation [144]. The average velocity is at its peak at Noon for cool materials and combined measures as observed in Figure 6.8 (a and b).

Flow velocities increase with the addition of water bodies [22] in the cool materials scenario, increasing from 0.4 - 0.8 m/sec (Figure 6.8 (c)). This large velocity leads to proper ventilation and results in a low heat accumulation phenomenon. Water promotes the wind velocity due to two possible reasons one because of its lower roughness compared to the surrounding elements, which may block the airflow slightly leading to high airflow speed, and second due to the temperature difference of water relevant to surroundings due to its high thermal capacity due to which air pressure gap could create in the micro-environment refers to as land water breeze develops.
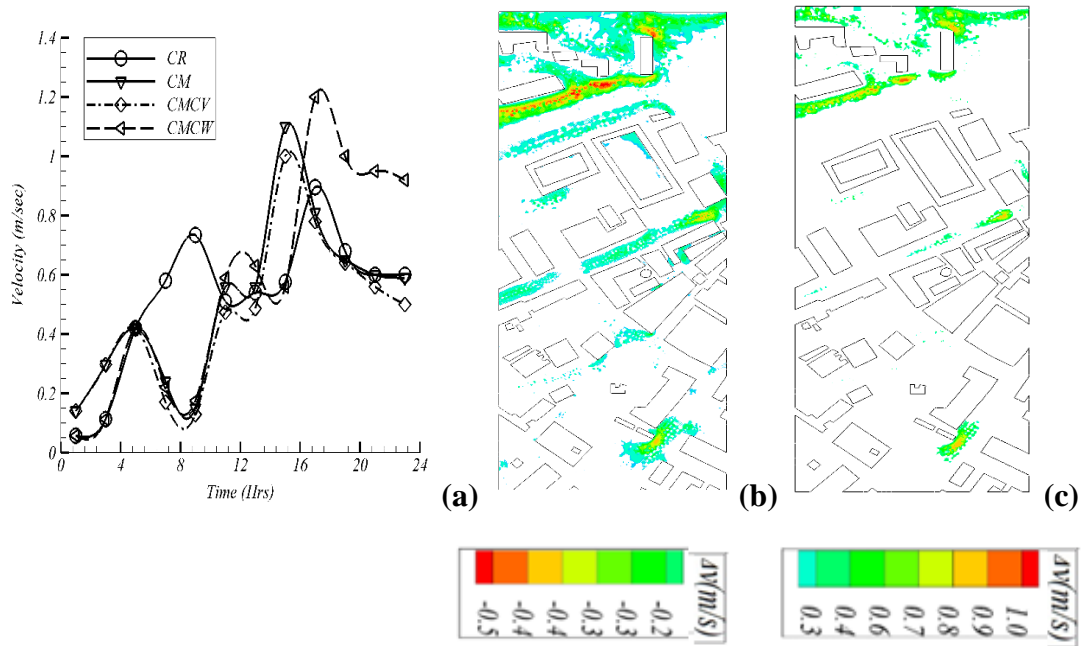
Figure 6.8: a) Twenty-four-hourly distribution of velocity b) contours of wake velocity difference between CMCV and CM, 1500hrs (c) contours of wake velocity difference between CMCW and CM, 1500hrs.

6.4   Summary

The urban heat island (UHI) phenomenon has become a major concern for city sustainability in the wake of global warming and rapid urbanization. This has resulted in increased heat stress and worsened outdoor thermal comfort in urban microclimates. The study demonstrates that heat stress can be mitigated by reducing air temperature and surface temperature with the integration of cool materials into the urban environment using computational fluid dynamics (CFD), applied individually and in combination with vegetation and water bodies under representative climatic conditions. The thermal comfort conditions are examined at pedestrian height and the diverse vertical levels by evaluating two climatic parameters: firstly, the reduction of ambient air temperature and surface temperature characterizing the mitigation (cooling) intensity, and secondly the alteration of airflow velocity. The analysis shows that the proposed interventions can effectively decrease surrounding temperature and promote airflow. Cool materials, when applied simultaneously on both buildings and ground, generate a more pronounced mitigation effect than on only the ground or the buildings as it results in a large reduction of air and surface temperature i.e. of 2 °C and 6 °C respectively. Furthermore, the impact is more significant for combined cool materials with vegetation and water as a large reduction of 2.2 °C and 1.9 °C in air

temperature; and 5.9 °C and 9 °C in surface temperature was observed respectively compared to the reference case. For airflow velocity, it is highest for combined cool materials with water, with maximum effect at the time of highest solar irradiance. Moreover, the study is expected to inform architects regarding retrofitting mitigation of UHI with these measures.

Chapter-7

Conclusions and Recommendations for Future Work

7.1   Conclusions

Computational fluid dynamics (CFD) has established itself as a valuable tool to model various urban physics phenomena and develop climate change and UHI mitigation/adaptation strategies; and urban microclimate studies using CFD are increasingly gaining scientific attention in wake of increased urbanization and urban warming, the major threat in urban sustainability. The present study aimed to perform a comparative assessment of various climate adaptation measures for improving outdoor thermal comfort. In this regard, a comprehensive CFD analysis using URANS approach was carried out by considering the application of these measures to a real hot and humid microclimate under a heatwave condition. The climate adaptation measures included the vegetation, water bodies and the cool materials.

First, the effect of using more realistic vegetation modeling terms along with different vegetation morphological characteristics used in the CFD simulations was studied. Next, separate simulations were then performed with vegetation base case, water bodies and cool materials in single and in combination. Following main conclusions can be drawn:

- First, vegetation can be effectively applied to reduce air and surface temperature. In all the studied scenarios, the cooling effect of vegetation is highly localized and is only observed in the vicinity of vegetation and more profound near to the ground. Different from daytime cooling, vegetation produces nocturnal heating at nighttime.

- Moreover, vegetation, when stimulated with different modeling parameters i.e., realistic values of canopy drag and transpiration rate, yields different micro

climatological results. The highest reduction of average 1.2 °C in air temperature at pedestrian height has been observed when vegetation is modeled with actual form drag coefficient. The tree modeled with variable transpiration rate coupled with humidity effect produces a reduction of 0.9 °C while only 0.4 °C was observed with a tune drag coefficient as compared with the reference case. In terms of surface temperature.

• The largest reduction of about 4 °C occurred with the inclusion of the transpiration rate of vegetation and only1.8 °C is with actual canopy drag.

• The use of an actual form drag coefficient and transpiration rated cooling power instead of a tuned drag and constant cooling power provides more pronounced thermal comfort conditions. For the case studied, the application of the actual form drag coefficient and variable transpiration rate resulted in the average reduction in the apparent temperature of 0.8 °C and 0.4 °C when compared to the simulation results which used the tuned drag coefficient.

• The tree model with the actual form drag coefficient has the highest impact in reducing the flow velocity i.e up to 0.5 m/sec while transpiration-rated vegetation decreases it up to 0.1 m/sec when compared with the reference case.

• For the considered climate, Bauhinia Blakeana is most influential in reducing the apparent temperature at the pedestrian height owing to its great leaf area index and small height while Guaiacum Offinate proves to be the least effective. The Bauhinia Blakeana resulted in a 1.2 °C decrease in the average temperature and 1.0 °C decrease in the apparent temperature respectively.

• The effectiveness of various tree species varies with urban morphology within the microclimate.

• It is also observed that an increase in low-level porosity and vegetation porosity are the most effective ways to reduce thermal stress because these produce a well-ventilated environment.

• Among all the individual strategies, water bodies provide the largest reduction in air temperature at pedestrian height (2°C) and cool materials provide a larger reduction in surface temperature (6 °C). Vertically, cool materials are more effective among the individual measures with UHI mitigation intensity of 1.5 °C which is then followed by vegetation i.e., 1. 0°C.

- The water bodies help in reducing the thermal stress of pedestrians but possess local effects i.e., only in the immediate surroundings.

- Combining cool materials with vegetation is helpful in significantly reducing the ambient air temperature and in managing the increased reflected solar radiation caused by materials having high albedo values as it results in a reduction of 2.2 °C in the air temperature and 5.9 °C in the surface temperature compared to the reference case.

- For the combined cool materials and water bodies' case, a relative reduction of 1.9 °C and 9 °C in air and surface temperature respectively, is observed. The maximum effect in terms of temperature reduction occurs at the time of high solar irradiance.

- The simulations result of all three combined measures showed further a greater mitigation effect as it results in a reduction of 2.2 °C in the air temperature and 9 °C in the surface temperature compared to the reference case. The maximum effect in terms of temperature reduction occurs at the time of high solar irradiance.

- The increase in the wind velocity is the highest for combined cool materials and water bodies case, reaching the peak value at the time of highest solar irradiance. The presence of vegetation decreases the wind velocity.

The tree species and water bodies considered, are not only native to Pakistan or Asia but also very common across the globe. This suggests that even though the case study is local, the findings and recommendations can be applied to other parts of the world having these tree species and water bodies of similar physical configuration and urban climate. The resulting level of thermal comfort, however, may vary due to differences in prevailing weather conditions and urban morphology. Moreover, the study is expected to inform architects regarding retrofitting mitigation of UHI with proposed adaptation measures. The study furnishes important information to analysts and researchers regarding the realistic numerical assessment of street trees by modeling their realistic canopies and parameters. Also, our findings provide enhanced knowledge to policymakers, urban planners, and other stakeholders for the planning and design of green spaces and blue landscape, maintenance of urban areas, and protection for the environmental quality at both building and city scales. Based upon the findings of this study, we propose that incorporation of adaptation measures should

be subjected to performance-based approach in different sky view fraction (SVF) locations for site specific measure under any representative climatic conditions. This will afford optimized heat mitigation inside city's landscape at city/building scale

7.2   Limitation and Future Work

There are some limitations to this study which are mainly related to the numerical setting in FLUENT flow solver: first, each building, grounds, and pavement is modeled with same material i.e., concrete, earth, and asphalt whereas, there are always mixed in the city domain. Optical degradation/aging due to dust deposition on their surfaces may significantly affect their cooling performance. Secondly, although the study includes four important morphological characteristics (CH, TH, CW, HT) along with LAD but leaf color/shape and texture also contributes to comfort improvement; thus, should be considered as is necessary to draw meaningful conclusions regarding vegetation and its effectiveness. Moreover, dominant wind directions during the heatwave period are kept constant for the whole simulation period which differs from with real atmospheric conditions; thus, varying hourly wind directions should be considered. Lastly, the anthropogenic heat source's contribution is not incorporated which can affect the accuracy of the study results. The major limitation of this study or CFD tool is of Fluent, which ignore emitted longwave radiation from porous zone to surrounding buildings and its simplified approach toward modeling solar radiation. Another limitation of this study is that wind gusts have not been modelled explicitly.

Various aspects of the study can be considered for future work. The inlet flow profiles for parameters (velocity, turbulent kinetic energy, and turbulence dissipation rate) considered in this study are usually applicable to neutrally stratified boundary layers. Similarly, a constant uniform hourly temperature has been used at the inlet side. Therefore, to account for different atmospheric conditions, relevant profiles should be used to predict flow inhomogeneity if it exists. Vegetation and water bodies also contribute to increasing the humidity inside the microclimate which also impacts the comfort conditions of the pedestrians alongside nocturnal heating.

The effectiveness of different climate change adaptation measures, in this study, are strongly the function of climate, size of measure and prevailing flow conditions. Hence the effect of variation with these parameters can also be studied. Thus, essential

knowledge for retrofitting mitigation of these adaptation measures is required for other cities having the same urban density, climate, and morphology.

References

[1] U. Nations, World urbanization prospects, (2018). https://population.un.org/wup/.

[2] UN, Sustainable development and climate action, (2019). http://www.un.org/en/development/desa/population/theme/urbanization/.

[3] U. Nation, World Urbanization Prospects., 2018.

[4] U. Nations, , Transforming our world: The 2030 agenda for sustainable development, New York, (2015). https://www.undp.org/sustainable-development-goals.

[5] D. Lai, W. Liu, T. Gan, K. Liu, Q. Chen, A review of mitigating strategies to improve the thermal environment and thermal comfort in urban outdoor spaces, Sci. Total Environ. 661 (2019) 337–353. https://doi.org/https://doi.org/10.1016/j.scitotenv.2019.01.062.

[6] T.E. Morakinyo, W. Ouyang, K.K.L. Lau, C. Ren, E. Ng, Right tree, right place (urban canyon): Tree species selection approach for optimum urban heat mitigation - development and evaluation, Sci. Total Environ. 719 (2020). https://doi.org/10.1016/j.scitotenv.2020.137461.

[7] M. Santamouris, Energy and climate in the urban built environment, changes., London: James and James Science Publishers, 2001.

[8] H. Akbari, C. Cartalis, D. Kolokotsa, A. Muscio, A.L. Pisello, F. Rossi, M. Santamouris, A. Synnefa, N.H. Wong, M. Zinzi, Local climate change and urban heat island mitigation techniques - The state of the art, J. Civ. Eng. Manag. 22 (2016) 1–16. https://doi.org/10.3846/13923730.2015.1111934.

[9] T.R. Oke, The energetic basis of the urban heat island, Q. J. R. Meteorol. Soc. 108 (1982) 1–24. https://doi.org/10.1002/qj.49710845502.

[10] Y. Toparlar, B. Blocken, P. Vos, G.J.F. Van Heijst, W.D. Janssen, T. van Hooff, H. Montazeri, H.J.P. Timmermans, CFD simulation and validation of urban microclimate: A case study for Bergpolder Zuid, Rotterdam, Build. Environ. 83 (2015) 79–90. https://doi.org/10.1016/j.buildenv.2014.08.004.

[11] U.S.A.R. IPCC, 2021. Cambridge University Press, Cambridge, United Kingdom and New York, NY, Climate Change 2021; The basic science report, 2021. https://doi.org/https://doi.org/10.1017/CBO9781107415324.

[12] M. Santamouris, S. Haddad, F. Fiorito, P. Osmond, L. Ding, D. Prasad, X. Zhai, R. Wang, Urban heat island and overheating characteristics in Sydney, Australia. An analysis of multiyear measurements, Sustain. 9 (2017). https://doi.org/10.3390/su9050712.

[13] O. Mazdiyasni, M. Sadegh, F. Chiang, A. AghaKouchak, Heat wave Intensity Duration Frequency Curve: A Multivariate Approach for Hazard and Attribution Analysis, Sci. Rep. 9 (2019) 1–8. https://doi.org/10.1038/s41598-019-50643-w.

[14] S.L. Harlan, G. Chowell, S. Yang, D.B. Petitti, E.J.M. Butler, B.L. Ruddell, D.M. Ruddell, Heat-related deaths in hot cities: Estimates of human tolerance

to high temperature thresholds, Int. J. Environ. Res. Public Health. 11 (2014) 3304–3326. https://doi.org/10.3390/ijerph110303304.

[15] K.T. Huang, S.R. Yang, A. Matzarakis, T.P. Lin, Identifying outdoor thermal risk areas and evaluation of future thermal comfort concerning shading orientation in a traditional settlement, Sci. Total Environ. 626 (2018) 567–580. https://doi.org/10.1016/j.scitotenv.2018.01.031.

[16] M.M. Sheikh, N. Manzoor, J. Ashraf, M. Adnan, D. Collins, S. Hameed, M.J. Manton, A.U. Ahmed, S.K. Baidya, H.P. Borgaonkar, N. Islam, D. Jayasinghearachchi, D.R. Kothawale, K.H.M.S. Premalal, J. V. Revadekar, M.L. Shrestha, Trends in extreme daily rainfall and temperature indices over South Asia, Int. J. Climatol. 35 (2015) 1625–1637. https://doi.org/10.1002/joc.4081.

[17] A.Q. Aslam, S.R. Ahmad, I. Ahmad, Y. Hussain, M.S. Hussain, Vulnerability and impact assessment of extreme climatic event: A case study of southern Punjab, Pakistan, Sci. Total Environ. 580 (2017) 468–481. https://doi.org/10.1016/j.scitotenv.2016.11.155.

[18] M. Santamouris, C. Cartalis, A. Synnefa, D. Kolokotsa, On the impact of urban heat island and global warming on the power demand and electricity consumption of buildings - A review, Energy Build. 98 (2015) 119–124. https://doi.org/10.1016/j.enbuild.2014.09.052.

[19] E. Commission, Adaptation to climate change, (2021). https://doi.org/https://ec.europa.eu/clima/eu-action/adaptation-climate-change_en.

[20] S. Kovats, R. Akhtar, Climate, climate change and human health in Asian cities, Environ. Urban. 20 (2008) 165–175. https://doi.org/10.1177/0956247808089154.

[21] A. Bhaduri, Climate Change, 2012. https://doi.org/10.1177/103530461202300301.

[22] L. Yang, X. Liu, F. Qian, Research on water thermal effect on surrounding environment in summer, Energy Build. 207 (2020) 109613. https://doi.org/10.1016/j.enbuild.2019.109613.

[23] C. Bartesaghi-Koc, S. Haddad, G. Pignatta, R. Paolini, D. Prasad, M. Santamouris, Can urban heat be mitigated in a single urban street? Monitoring, strategies, and performance results from a real scale redevelopment project, Sol. Energy. 216 (2021) 564–588. https://doi.org/10.1016/j.solener.2020.12.043.

[24] S. Haddad, R. Paolini, G. Ulpiani, A. Synnefa, G. Hatvani-Kovacs, S. Garshasbi, J. Fox, K. Vasilakopoulou, L. Nield, M. Santamouris, Holistic approach to assess co-benefits of local climate mitigation in a hot humid region of Australia, Sci. Rep. 10 (2020) 1–17. https://doi.org/10.1038/s41598-020-71148-x.

[25] A. Ahmadi Venhari, M. Tenpierik, M. Taleghani, The role of sky view factor and urban street greenery in human thermal comfort and heat stress in a desert climate, J. Arid Environ. 166 (2019) 68–76. https://doi.org/10.1016/j.jaridenv.2019.04.009.

[26] S. Thorsson, T. Honjo, F. Lindberg, I. Eliasson, E.M. Lim, Thermal comfort

and outdoor activity in Japanese urban public places, Environ. Behav. 39 (2007) 660–684. https://doi.org/10.1177/0013916506294937.

[27] I. Saito, O. Ishihara, T. Katayama, Study of the effect of green areas on the thermal environment in an urban area, Energy Build. 15 (1990) 493–498. https://doi.org/10.1016/0378-7788(90)90026-F.

[28] B. Blocken, 50 years of Computational Wind Engineering: Past, present and future, J. Wind Eng. Ind. Aerodyn. 129 (2014) 69–102. https://doi.org/https://doi.org/10.1016/j.jweia.2014.03.008.

[29] I. Lun, A. Mochida, R. Ooka, Progress in numerical modelling for urban thermal environment studies, Adv. Build. Energy Res. 3 (2009) 147–188. https://doi.org/10.3763/aber.2009.0306.

[30] P. Moonen, T. Defraeye, V. Dorer, B. Blocken, J. Carmeliet, Urban Physics: Effect of the micro-climate on comfort, health and energy demand, Front. Archit. Res. 1 (2012) 197–228. https://doi.org/10.1016/j.foar.2012.05.002.

[31] T.E. Morakinyo, K.K.L. Lau, C. Ren, E. Ng, Performance of Hong Kong's common trees species for outdoor temperature regulation, thermal comfort and energy saving, Build. Environ. 137 (2018) 157–170. https://doi.org/10.1016/j.buildenv.2018.04.012.

[32] C. Gromke, B. Blocken, W. Janssen, B. Merema, T. van Hooff, H. Timmermans, CFD analysis of transpirational cooling by vegetation: Case study for specific meteorological conditions during a heat wave in Arnhem, Netherlands, Build. Environ. 83 (2015) 11–26. https://doi.org/10.1016/j.buildenv.2014.04.022.

[33] A.M. Rizwan, L.Y.C. Dennis, C. Liu, A review on the generation, determination and mitigation of Urban Heat Island, J. Environ. Sci. 20 (2008) 120–128. https://doi.org/10.1016/S1001-0742(08)60019-4.

[34] A. Revi, D. Satterthwaite, F. Aragón-Durand, J. Corfee-Morlot, R.B.R. Kiunsi, M. Pelling, D. Roberts, W. Solecki, S.P. Gajjar, A. Sverdlik, Towards transformative adaptation in cities: The IPCC's Fifth Assessment, Environ. Urban. 26 (2014) 11–28. https://doi.org/10.1177/0956247814523539.

[35] D.E. Bowler, L. Buyung-Ali, T.M. Knight, A.S. Pullin, Urban greening to cool towns and cities: A systematic review of the empirical evidence, Landsc. Urban Plan. 97 (2010) 147–155. https://doi.org/10.1016/j.landurbplan.2010.05.006.

[36] K. Perini, A. Magliocco, Effects of vegetation, urban density, building height, and atmospheric conditions on local temperatures and thermal comfort, Urban For. Urban Green. 13 (2014) 495–506. https://doi.org/10.1016/j.ufug.2014.03.003.

[37] E. Jamei, P. Rajagopalan, M. Seyedmahmoudian, Y. Jamei, Review on the impact of urban geometry and pedestrian level greening on outdoor thermal comfort, Renew. Sustain. Energy Rev. 54 (2016) 1002–1017. https://doi.org/10.1016/j.rser.2015.10.104.

[38] M. Santamouris, Using cool pavements as a mitigation strategy to fight urban heat island - A review of the actual developments, Renew. Sustain. Energy Rev. 26 (2013) 224–240. https://doi.org/10.1016/j.rser.2013.05.047.

[39] H.K. T. Sato, S. Murakami, R. Ooka, S. Yoshida, K. Harayama, Numerical study on effects of countermeasures for urban heat island in summer and winter : The characteristic of urban climate and effects of greening and high albedo surface, J. Environ. Eng. (Transactions AIJ). 69 (2004) 55–62. https://doi.org/10.3130/aije.69.55_1.

[40] C. O'Malley, P. Piroozfar, E.R.P. Farr, F. Pomponi, Urban Heat Island (UHI) mitigating strategies: A case-based comparative analysis, Sustain. Cities Soc. 19 (2015) 222–235. https://doi.org/10.1016/j.scs.2015.05.009.

[41] S.A. Shiflett, L.L. Liang, S.M. Crum, G.L. Feyisa, J. Wang, G.D. Jenerette, Variation in the urban vegetation, surface temperature, air temperature nexus, Sci. Total Environ. 579 (2017) 495–505. https://doi.org/10.1016/j.scitotenv.2016.11.069.

[42] J.F. Barlow, Progress in observing and modelling the urban boundary layer, Urban Clim. 10 (2014) 216–240. https://doi.org/10.1016/j.uclim.2014.03.011.

[43] J. Lu, Q. Li, L. Zeng, J. Chen, G. Liu, Y. Li, W. Li, K. Huang, A micro-climatic study on cooling effect of an urban park in a hot and humid climate, Sustain. Cities Soc. 32 (2017) 513–522. https://doi.org/10.1016/j.scs.2017.04.017.

[44] S. Zheng, L. Zhao, Q. Li, Numerical simulation of the impact of different vegetation species on the outdoor thermal environment, Urban For. Urban Green. 18 (2016) 138–150. https://doi.org/10.1016/j.ufug.2016.05.008.

[45] M. Zhang, W. Bae, J. Kim, The effects of the layouts of vegetation and wind flow in an apartment housing complex to mitigate outdoor microclimate air temperature, Sustain. 11 (2019). https://doi.org/10.3390/su11113081.

[46] M.A. Rahman, A. Moser, A. Gold, T. Rötzer, S. Pauleit, Vertical air temperature gradients under the shade of two contrasting urban tree species during different types of summer days, Sci. Total Environ. 633 (2018) 100–111. https://doi.org/10.1016/j.scitotenv.2018.03.168.

[47] Y. Toparlar, B. Blocken, B. Maiheu, G.J.F. van Heijst, The effect of an urban park on the microclimate in its vicinity: a case study for Antwerp, Belgium, Int. J. Climatol. 38 (2018) e303–e322. https://doi.org/10.1002/joc.5371.

[48] N. Meili, J.A. Acero, N. Peleg, G. Manoli, P. Burlando, S. Fatichi, Vegetation cover and plant-trait effects on outdoor thermal comfort in a tropical city, Build. Environ. 195 (2021) 107733. https://doi.org/10.1016/j.buildenv.2021.107733.

[49] N. Meili, G. Manoli, P. Burlando, J. Carmeliet, W.T.L. Chow, A.M. Coutts, M. Roth, E. Velasco, E.R. Vivoni, S. Fatichi, Tree effects on urban microclimate: Diurnal, seasonal, and climatic temperature differences explained by separating radiation, evapotranspiration, and roughness effects, Urban For. Urban Green. 58 (2021) 126970. https://doi.org/10.1016/j.ufug.2020.126970.

[50] K. Fabbri, A. Ugolini, A. Iacovella, A.P. Bianchi, The effect of vegetation in outdoor thermal comfort in archaeological area in urban context, Build. Environ. 175 (2020) 106816. https://doi.org/10.1016/j.buildenv.2020.106816.

[51] V.S. Duval, G.M. Benedetti, K. Baudis, The impact of street trees on the urban microclimate. Bahía Blanca, Argentina, Investig. Geogr. (2020) 171–188. https://doi.org/10.14198/INGEO2020.DBB.

[52] M. Detommaso, A. Gagliano, L. Marletta, F. Nocera, Sustainable urban greening and cooling strategies for thermal comfort at pedestrian level, Sustain. 13 (2021). https://doi.org/10.3390/su13063138.

[53] F. Zeng, C. Lei, J. Liu, J. Niu, N. Gao, CFD simulation of the drag e ff ect of urban trees : Source term modi fi cation method revisited at the tree scale, 56 (2020). https://doi.org/10.1016/j.scs.2020.102079.

[54] E. Ng, L. Chen, Y. Wang, C. Yuan, A study on the cooling effects of greening in a high-density city: An experience from Hong Kong, Build. Environ. 47 (2012) 256–271. https://doi.org/10.1016/j.buildenv.2011.07.014.

[55] L. Berry, R., Livesley, S. J., & Aye, Tree canopy shade impacts on solar irradiance received by building walls and their surface temperature, Build. Environ. 69 (2013) 91-100. https://doi.org/https://doi.org/10.1016/j.buildenv.2013.07.009.

[56] L.V. de Abreu-Harbich, L.C. Labaki, A. Matzarakis, Effect of tree planting design and tree species on human thermal comfort in the tropics, Landsc. Urban Plan. 138 (2015) 99–109. https://doi.org/10.1016/j.landurbplan.2015.02.008.

[57] M.Y. M. Fahmy, S. Sharples, LAI based trees selection for mid latitude urban developments: A microclimatic study in Cairo, Build. Environ. 45 (2010) 345–357. https://doi.org/https://doi.org/10.1016/j.buildenv.2009.06.014.

[58] S. Teshnehdel, H. Akbari, E. Di Giuseppe, R.D. Brown, Effect of tree cover and tree species on microclimate and pedestrian comfort in a residential district in Iran, Build. Environ. 178 (2020) 106899. https://doi.org/10.1016/j.buildenv.2020.106899.

[59] V.Z.A. Soultana K. Gianniou, Evaporation and energy budget in lake vegoritis, Greec, J. Hydr. 345 (2007) 212–223.

[60] M. Taleghani, D.J. Sailor, M. Tenpierik, A. van den Dobbelsteen, Thermal assessment of heat mitigation strategies: The case of Portland State University, Oregon, USA, Build. Environ. 73 (2014) 138–150. https://doi.org/10.1016/j.buildenv.2013.12.006.

[61] E.A. Hathway, S. Sharples, The interaction of rivers and urban form in mitigating the Urban Heat Island effect: A UK case study, Build. Environ. 58 (2012) 14–22. https://doi.org/10.1016/j.buildenv.2012.06.013.

[62] X.L. Chen, H.M. Zhao, P.X. Li, Z.Y. Yin, Remote sensing image-based analysis of the relationship between urban heat island and land use/cover changes, Remote Sens. Environ. 104 (2006) 133–146. https://doi.org/10.1016/j.rse.2005.11.016.

[63] N.E. Theeuwes, A. Solcerová, G.J. Steeneveld, Modeling the influence of open water surfaces on the summertime temperature and thermal comfort in the city, J. Geophys. Res. Atmos. 118 (2013) 8881–8896. https://doi.org/10.1002/jgrd.50704.

[64] N.I. Syafii, M. Ichinose, E. Kumakura, K. Chigusa, S.K. Jusuf, N.H. Wong, Enhancing the potential cooling benefits of urban water bodies, Nakhara J. Environ. Des. Plan. 13 (2017) 29–40.

[65] R. Sun, L. Chen, How can urban water bodies be designed for climate

adaptation?, Landsc. Urban Plan. 105 (2012) 27–33. https://doi.org/10.1016/j.landurbplan.2011.11.018.

[66] Y. Tominaga, Y. Sato, S. Sadohara, CFD simulations of the effect of evaporative cooling from water bodies in a micro-scale urban environment: Validation and application studies, Sustain. Cities Soc. 19 (2015) 259–270. https://doi.org/10.1016/j.scs.2015.03.011.

[67] M. Santamouris, R. Paolini, S. Haddad, A. Synnefa, S. Garshasbi, G. Hatvani-Kovacs, K. Gobakis, K. Yenneti, K. Vasilakopoulou, J. Feng, K. Gao, G. Papangelis, A. Dandou, G. Methymaki, P. Portalakis, M. Tombrou, Heat mitigation technologies can improve sustainability in cities. An holistic experimental and numerical impact assessment of urban overheating and related heat mitigation strategies on energy consumption, indoor comfort, vulnerability and heat-related m, Energy Build. 217 (2020) 110002. https://doi.org/10.1016/j.enbuild.2020.110002.

[68] J. Fahed, E. Kinab, S. Ginestet, L. Adolphe, Impact of urban heat island mitigation measures on microclimate and pedestrian comfort in a dense urban district of Lebanon, Sustain. Cities Soc. 61 (2020) 102375. https://doi.org/10.1016/j.scs.2020.102375.

[69] S. Tsoka, T. Theodosiou, K. Tsikaloudaki, F. Flourentzou, Modeling the performance of cool pavements and the effect of their aging on outdoor surface and air temperatures, Sustain. Cities Soc. 42 (2018) 276–288. https://doi.org/10.1016/j.scs.2018.07.016.

[70] C. Georgakis, S. Zoras, M. Santamouris, Studying the effect of "cool" coatings in street urban canyons and its potential as a heat island mitigation technique, Sustain. Cities Soc. 13 (2014) 20–31. https://doi.org/10.1016/j.scs.2014.04.002.

[71] S. Sen, J. Roesler, B. Ruddell, A. Middel, Cool pavement strategies for Urban Heat Island mitigation in Suburban Phoenix, Arizona, Sustain. 11 (2019) 1–21. https://doi.org/10.3390/su11164452.

[72] N.L. Alchapar, C.C. Pezzuto, E.N. Correa, L. Chebel Labaki, The impact of different cooling strategies on urban air temperatures: the cases of Campinas, Brazil and Mendoza, Argentina, Theor. Appl. Climatol. 130 (2017) 35–50. https://doi.org/10.1007/s00704-016-1851-5.

[73] T.E. Morakinyo, L. Kong, K.K. Lau, C. Yuan, E. Ng, A study on the impact of shadow-cast and tree species on in-canyon and neighborhood's thermal comfort., Build. Environ. 115 (2017) 1–7. https://doi.org/10.1016/j.buildenv.2017.01.005.This.

[74] A.M. Society;, AMS. Meteorological Glossary., (2014). http://glossary.ametsoc.org/wiki/Mesoscale.

[75] B. Blocken, Computational Fluid Dynamics for urban physics: Importance, scales, possibilities, limitations and ten tips and tricks towards accurate and reliable simulations, Build. Environ. 91 (2015) 219–245. https://doi.org/10.1016/j.buildenv.2015.02.015.

[76] P.A. Mirzaei, Recent challenges in modeling of urban heat island, Sustain. Cities Soc. 19 (2015) 200–206. https://doi.org/10.1016/j.scs.2015.04.001.

[77]   P.A. Mirzaei, F. Haghighat, Approaches to study Urban Heat Island - Abilities and limitations, Build. Environ. 45 (2010) 2192–2201. https://doi.org/10.1016/j.buildenv.2010.04.001.

[78]   ANSYS, ANSYS Fluent Theory/User Guide, Canonsburg: ANSYS, Inc, 2016., (2016).

[79]   C. Sanz, A Note On k-epsilon Modelling Of Vegetation Canopy Air-Flows, Boundary-Layer Meteorol. 108(1) (2003) 191–197.

[80]   J. Liu, J.M. Chen, T.A. Black, M.D. Novak, E - ε modelling of turbulent air flow downwind of a model forest edge, Boundary-Layer Meteorol. 77 (1996) 21–44. https://doi.org/10.1007/BF00121857.

[81]   S.R. Green, Modelling turbulent air flow in a stand of widely-spaced trees., J. Comput. Fluid Dyn. Its Appl. 5 (1992) 294–312.

[82]   National Parks Board (NParks), https://www.nparks.gov.sg, n.d.

[83]   Y.H. Mo, J.B.; Wang, L.M.; Qin, J.; Huang, J.; Hu, Study on temperature decreasing and humidification of ornamental plants in Shanghai., J. Anhui Agric. Sci. (2007).

[84]   B.. Amiro, comparison of turbulence statistics within three boreal forest canopies, Boundary-Layer Meteorol. 51 (1990) 99–121.

[85]   L. Shashua-Bar, D. Pearlmutter, E. Erell, The influence of trees and grass on outdoor thermal comfort in a hot-arid environment, Int. J. Climatol. 31 (2011) 1498–1506. https://doi.org/10.1002/joc.2177.

[86]   D.J. Nowak, Estimating leaf area and leaf biomass of open-grown deciduous urban trees, For. Sci. 42 (1996) 504–507.

[87]   F. Kong, C. Sun, F. Liu, H. Yin, F. Jiang, Y. Pu, G. Cavan, C. Skelhorn, A. Middel, I. Dronova, Energy saving potential of fragmented green spaces due to their temperature regulating ecosystem services in the summer, Appl. Energy. 183 (2016) 1428–1440. https://doi.org/10.1016/j.apenergy.2016.09.070.

[88]   M.A. Rahman, A. Moser, S. Pauleit, Within canopy temperature differences and cooling ability of Tilia cordata trees grown in urban conditions, Build. Environ. (2017). https://doi.org/10.1016/j.buildenv.2016.12.013.This.

[89]   R.G. Steadman, A universal scale of apparent temperature., J. Clim. Appl. Meteorol. 23 (1984) 1674–1687. https://doi.org/10.1175/1520-0450(1984)023<1674:AUSOAT>2.0.CO;2.

[90]   A.S. et al. Shih, W. Liou, Z.Y. and J. ZHU, A new kt eddy viscosity model for high Reynolds number turbulent flows, Compurers Fluids. 24 (1995) 227-238.199.

[91]   Y. Tominaga, A. Mochida, R. Yoshie, H. Kataoka, T. Nozu, M. Yoshikawa, T. Shirasawa, AIJ guidelines for practical applications of CFD to pedestrian wind environment around buildings, J. Wind Eng. Ind. Aerodyn. 96 (2008) 1749–1761. https://doi.org/10.1016/j.jweia.2008.02.058.

[92]   J. Franke, A. Hellsten, H. Schlünzen, B. Carissimo, The Best Practise Guideline for the CFD simulation of flows in the urban environment : an outcome of COST 732, Fifth Int. Symp. Comput. Wind Eng. (2010) 1–10.

[93] I. Pointwise, https://www.pointwise.com., (n.d.). https://doi.org/https://www.pointwise.com.

[94] B.J. Merema, Computational analysis of climate change adaptation measures at the building and street scale focused on vegetative measures, 2013.

[95] P.J Richard; R.P Hoxey, Appropriate boundary conditions for computational wind engineering models using k-e turbulence model, J. Wind Eng. Ind. Aerodyn. 46 (1993) 145–153.

[96] Y. Toparlar, B. Blocken, B. Maiheu, G.J.F. van Heijst, Impact of urban microclimate on summertime building cooling demand: A parametric analysis for Antwerp, Belgium, Appl. Energy. 228 (2018) 852–872. https://doi.org/10.1016/j.apenergy.2018.06.110.

[97] H. Lin, Y. Xiao, F. Musso, Y. Lu, Green façade effects on thermal environment in transitional space: Field measurement studies and computational fluid dynamics simulations, Sustain. 11 (2019) 1–21. https://doi.org/10.3390/su11205691.

[98] B.E. Launder, D.B. Spalding, The numerical computation of turbulent flows, Comput. Methods Appl. Mech. Eng. 3 (1974) 269–289. https://doi.org/10.1016/0045-7825(74)90029-2.

[99] T. Cebeci, P. Bradshaw, Momentum transfer in boundary layers. Wash DC Hemisphere Publ Corp N YMcGraw-Hill Book, 1977.

[100] S. Tsoka, Investigating the Relationship Between Urban Spaces Morphology and Local Microclimate: A Study for Thessaloniki, Procedia Environ. Sci. 38 (2017) 674–681. https://doi.org/10.1016/j.proenv.2017.03.148.

[101] J. Yuan, K. Emura, C. Farnham, Is urban albedo or urban green covering more effective for urban microclimate improvement?: A simulation for Osaka, Sustain. Cities Soc. 32 (2017) 78–86. https://doi.org/10.1016/j.scs.2017.03.021.

[102] S. Sajjad, N. Blond, R. Batool, S. Shirazi, K. Shakrullah, M. Bhalli, Study of Urban Heat Island of Karachi by Using Finite Volume Mesoscale Model, J. Basic Appl. Sci. 11 (2015) 101–105. https://doi.org/10.6000/1927-5129.2015.11.13.

[103] M.A. Rahman, C. Hartmann, A. Moser-Reischl, M.F. von Strachwitz, H. Paeth, H. Pretzsch, S. Pauleit, T. Rötzer, Tree cooling effects and human thermal comfort under contrasting species and sites, Agric. For. Meteorol. 287 (2020) 107947. https://doi.org/10.1016/j.agrformet.2020.107947.

[104] L. Massetti, M. Petralli, M. Napoli, G. Brandani, S. Orlandini, D. Pearlmutter, Effects of deciduous shade trees on surface temperature and pedestrian thermal stress during summer and autumn, Int. J. Biometeorol. 63 (2019) 467–479. https://doi.org/10.1007/s00484-019-01678-1.

[105] D. Armson, M.A. Rahman, A.R. Ennos, A comparison of the shading effectiveness of five different street tree species in Manchester, UK, Arboric. Urban For. 39 (2013) 157–164.

[106] J. Konarska, F. Lindberg, A. Larsson, S. Thorsson, B. Holmer, Transmissivity of solar radiation through crowns of single urban trees-application for outdoor

thermal comfort modelling, Theor. Appl. Climatol. 117 (2014) 363–376. https://doi.org/10.1007/s00704-013-1000-3.

[107] AIAA, Guide Guide for the Verification and Validation of Computational, Am. Inst. Aeronaut. Astronaut. 2002 (2002) 1–29.

[108] C.J. Roy, W.L. Oberkampf, Verification and validation in computational fluid dynamics, 2016. https://doi.org/10.1201/b19031-50.

[109] W.L. Oberkampf, T.G. Trucano, C. Hirsch, Verification, validation, and predictive capability in computational engineering and physics, Appl. Mech. Rev. 57 (2004) 345–384. https://doi.org/10.1115/1.1767847.

[110] K.I. of Technology, CODASC database, (2008).

[111] A.I. of Japan, data sets, (2007).

[112] U. of Hamburg, CEDVAL database, (1999). (www.mi.uni-hamburg.de/cedval).

[113] M. NASA, "MODIS," 18 June 2015., (2015). https://doi.org/Available: https://modis.gsfc.nasa.gov/data/dataprod/mod11.php.

[114] N. Antoniou, H. Montazeri, M. Neophytou, B. Blocken, CFD simulation of urban microclimate: Validation using high-resolution field measurements, Sci. Total Environ. 695 (2019). https://doi.org/10.1016/j.scitotenv.2019.133743.

[115] M. Park, A. Hagishima, J. Tanimoto, K. ichi Narita, Effect of urban vegetation on outdoor thermal environment: Field measurement at a scale model site, Build. Environ. 56 (2012) 38–46. https://doi.org/10.1016/j.buildenv.2012.02.015.

[116] J.A. Oke, T.R., Mills, G., Christen, A., Voogt, Urban Climates., Cambridge University 8 Press, Cambridge, United Kingdom, 2017.

[117] C. Yan, Q. Guo, H. Li, L. Li, G.Y. Qiu, Quantifying the cooling effect of urban vegetation by mobile traverse method: A local-scale urban heat island study in a subtropical megacity, Build. Environ. 169 (2020) 106541. https://doi.org/10.1016/j.buildenv.2019.106541.

[118] Lai, D., Liu, W., Gan, T., Liu, K., and Chen, Q. 2019. "A review of mitigating strategies to improve the thermal environment and thermal comfort in urban outdoor spaces," (2019) 337–353.

[119] Z. Tan, K.K.L. Lau, E. Ng, Planning strategies for roadside tree planting and outdoor comfort enhancement in subtropical high-density urban areas, Build. Environ. 120 (2017) 93–109. https://doi.org/10.1016/j.buildenv.2017.05.017.

[120] S. Liu, X. Yang, H. Yang, P. Gao, J. Hang, Q. Wang, Numerical investigation of solar impacts on canyon vortices and its dynamical generation mechanism, Urban Clim. 39 (2021). https://doi.org/10.1016/j.uclim.2021.100978.

[121] H. Montazeri, Y. Toparlar, B. Blocken, J.L.M. Hensen, Simulating the cooling effects of water spray systems in urban landscapes: A computational fluid dynamics study in Rotterdam, The Netherlands, Landsc. Urban Plan. 159 (2017) 85–100. https://doi.org/10.1016/j.landurbplan.2016.10.001.

[122] S. Tsoka, K. Tsikaloudaki, T. Theodosiou, Urban space's morphology and microclimatic analysis: A study for a typical urban district in the Mediterranean

city of Thessaloniki, Greece, Energy Build. 156 (2017) 96–108. https://doi.org/10.1016/j.enbuild.2017.09.066.

[123] F. Ali-Toudert, H. Mayer, Numerical study on the effects of aspect ratio and orientation of an urban street canyon on outdoor thermal comfort in hot and dry climate, Build. Environ. 41 (2006) 94–108. https://doi.org/10.1016/j.buildenv.2005.01.013.

[124] N.E. Theeuwes, G.J. Steeneveld, R.J. Ronda, B.G. Heusinkveld, L.W.A. van Hove, A.A.M. Holtslag, Seasonal dependence of the urban heat island on the street canyon aspect ratio, Q. J. R. Meteorol. Soc. 140 (2014) 2197–2210. https://doi.org/10.1002/qj.2289.

[125] W. Yue, X. Liu, Y. Zhou, Y. Liu, Impacts of urban configuration on urban heat island: An empirical study in China mega-cities, Sci. Total Environ. 671 (2019) 1036–1046. https://doi.org/10.1016/j.scitotenv.2019.03.421.

[126] T. Kato, T., Nakane, K., & Yamada, Fundamental experiment of evaporation mechanism on small scale water surface., Proc. Hydraul. Eng. Japan Soc. Civ. Eng. 53 (2009) 343–348 (in Japanese).

[127] H. Lee, H. Mayer, L. Chen, Contribution of trees and grasslands to the mitigation of human heat stress in a residential district of Freiburg, Southwest Germany, Landsc. Urban Plan. 148 (2016) 37–50. https://doi.org/10.1016/j.landurbplan.2015.12.004.

[128] X. Yang, L. Zhao, M. Bruse, Q. Meng, Evaluation of a microclimate model for predicting the thermal behavior of different ground surfaces, Build. Environ. 60 (2013) 93–104. https://doi.org/10.1016/j.buildenv.2012.11.008.

[129] C. Jacobs, L. Klok, M. Bruse, J. Cortesão, S. Lenzholzer, J. Kluck, Are urban water bodies really cooling?, Urban Clim. 32 (2020) 100607. https://doi.org/10.1016/j.uclim.2020.100607.

[130] B.J. He, L. Ding, D. Prasad, Outdoor thermal environment of an open space under sea breeze: A mobile experience in a coastal city of Sydney, Australia, Urban Clim. 31 (2020) 100567. https://doi.org/10.1016/j.uclim.2019.100567.

[131] P. Ampatzidis, T. Kershaw, A review of the impact of blue space on the urban microclimate, Sci. Total Environ. 730 (2020) 139068. https://doi.org/10.1016/j.scitotenv.2020.139068.

[132] W. Triyuly, S. Triyadi, S. Wonorahardjo, Synergising the thermal behaviour of water bodies within thermal environment of wetland settlements, Int. J. Energy Environ. Eng. 12 (2021) 55–68. https://doi.org/10.1007/s40095-020-00355-z.

[133] G. Manteghi, H. Bin Limit, D. Remaz, Water bodies an urban microclimate: A review, Mod. Appl. Sci. 9 (2015) 1–12. https://doi.org/10.5539/mas.v9n6p1.

[134] T.F. Zhao, K.F. Fong, Characterization of different heat mitigation strategies in landscape to fight against heat island and improve thermal comfort in hot–humid climate (Part I): Measurement and modelling, Sustain. Cities Soc. 32 (2017) 523–531. https://doi.org/10.1016/j.scs.2017.03.025.

[135] A. Syafrina, M.D. Koerniawan, D. Novianto, H. Fukuda, Influence of Urban Water Body on Thermal Environment in Pontianak City, J. Asian Inst. Low Carbon Des. (2020) 163–166.

[136] R. Levinson, P. Berdahl, H. Akbari, W. Miller, I. Joedicke, J. Reilly, Y. Suzuki, M. Vondran, Methods of creating solar-reflective nonwhite surfaces and their application to residential roofing materials, Sol. Energy Mater. Sol. Cells. 91 (2007) 304–314. https://doi.org/10.1016/j.solmat.2006.06.062.

[137] Canadian Center for Occupational Health and Safety., Skin Cancer and Sunlight, (n.d.).

[138] H. Taha, Urban surface modification as a potential ozone air-quality improvement strategy in California: A mesoscale modelling study, Boundary-Layer Meteorol. 127 (2008) 219–239. https://doi.org/10.1007/s10546-007-9259-5.

[139] E. Mastrapostoli, M. Santamouris, D. Kolokotsa, P. Vassilis, D. Venieri, K. Gompakis, On the ageing of cool roofs: Measure of the optical degradation, chemical and biological analysis and assessment of the energy impact, Energy Build. 114 (2016) 191–199. https://doi.org/10.1016/j.enbuild.2015.05.030.

[140] S. Tsoka, A. Tsikaloudaki, T. Theodosiou, Analyzing the ENVI-met microclimate model's performance and assessing cool materials and urban vegetation applications–A review, Sustain. Cities Soc. 43 (2018) 55–76. https://doi.org/10.1016/j.scs.2018.08.009.

[141] J. Gilabert, S. Ventura, R. Segura, A. Martilli, A. Badia, C. Llasat, J. Corbera, G. Villalba, Abating heat waves in a coastal Mediterranean city: What can cool roofs and vegetation contribute?, Urban Clim. 37 (2021) 100863. https://doi.org/10.1016/j.uclim.2021.100863.

[142] K. Perini, M. Ottelé, A.L.A. Fraaij, E.M. Haas, R. Raiteri, Vertical greening systems and the effect on air flow and temperature on the building envelope, Build. Environ. 46 (2011) 2287–2294. https://doi.org/10.1016/j.buildenv.2011.05.009.

[143] C.Y. Jim, Thermal performance of climber greenwalls: Effects of solar irradiance and orientation, Appl. Energy. 154 (2015) 631–643. https://doi.org/10.1016/j.apenergy.2015.05.077.

[144] Q. Wang, Y. Fan, J. Hang, Y. Li, Interacting urban heat island circulations as affected by weak background wind, Build. Environ. 160 (2019) 106224. https://doi.org/10.1016/j.buildenv.2019.106224.

Appendices

Appendix A: Meteorological Data

Date	Duration (Hrs)	Sea Pressure Level (hpa)	Average DBT °C	Average Relative Humidity (%)	Average Wind Speed (m.sec^{-1})
18-6-15	0-5AM	999	32.5	69	1.4
18-6-15	6-14 AM	999	37.6	48.8	5.35
18-6-15	15-23 AM	999	33.2	62	3.43
19-6-15	0-5AM	997	34	58	1.54
19-6-15	6-14 AM	997	38.6	43.1	5.21
19-6-15	15-23 AM	997	32.8	71.1	2.75
20-6-15	0-5AM	994	34	61.3	2.16
20-6-15	6-14 AM	994	40.5	39	4.23
20-6-15	15-23 AM	994	35.2	58.7	1
21-6-15	0-5AM	995	35	53.1	1.33
21-6-15	6-14 AM	995	40.6	32.4	3.78
21-6-15	15-23 AM	995	37	44.7	3.1
22-6-15	0-5AM	995	35.3	54.3	3.1
22-6-15	6-14 AM	995	39.46	46.2	3.61
22-6-15	15-23 AM	995	34.9	58.3	2.73

Appendix B: User Defined Function

User-Defined Functions for real transpiration rate and cooling power

//*For shading effect, alpha shaded=alpha open (1-SF), SF is typically 0.88.

#include "udf.h"

#define lambda 0.35

#define zo 0.5

real A1 = 1; /*Betap*/

real A2 = 5.1; /*Betad*/

```c
real A3 = 0.4; /*closure constant cepsilon4*/

real A4 = 0.4; /*closure constant cepsilon5*/

real kvon = 0.41;

real uref = 2.75;

real href = 250;

real h=9;

real cu =0.09;

real Rw =810;//*unts g.m^-2.day^-1

DEFINE_PROFILE(inlet_x_velocity, thread, nv)

{ real x[ND_ND]; /* position vector */

real z, ustar;

face_t f;

begin_f_loop(f, thread)

{ F_CENTROID(x,f,thread);

z = x[2];

ustar= kvon*uref/log((href+zo)/zo);

if (z<=href)

{F_PROFILE(f, thread, nv) = ustar/kvon*log((z+zo)/zo);}

else

{F_PROFILE( f , thread , nv )= uref;}

end_f_loop(f, thread) }}
```

/* calculation of the profile for turbulent kinetic energy */

```c
DEFINE_PROFILE(tke, thread, nv) /* function name, thread and variable number */

{ face_t f;

real x[ND_ND];

real z, ustar;

begin_f_loop (f,thread)

{ F_CENTROID(x,f,thread);

z=x[2];

ustar= kvon*uref/log((href+zo)/zo);

if (z<=href)

{F_PROFILE(f,thread,nv) =((ustar*ustar)/sqrt(cu));}
```

else

{F_PROFILE(f,thread,nv) = 0;}

end_f_loop(f,thread) } }

/* calculation of the profile for turbulence dissipation rate */

DEFINE_PROFILE(eps, thread, nv) /* function name, thread and variable number */

{ face_t f;

real x[ND_ND];

real z, ustar;

begin_f_loop (f,thread)

{ z=x[2];

F_CENTROID(x,f,thread);

ustar= kvon*uref/log((href+zo)/zo);

if (z<=href)

{ F_PROFILE(f,thread,nv) = (ustar*ustar*ustar)/(kvon*(z+zo));}

else

{F_PROFILE(f,thread,nv) = 0;}

end_f_loop(f,thread)}}

Source Term for Momentum

DEFINE_SOURCE(x_mom_source,c,t,dS,eqn)

{ real x[ND_ND];

real source, LAD;

real znorm;

real U = C_U(c,t);

real V = C_V(c,t);

real W = C_W(c,t);

real VEL = sqrt(C_U(c,t)*C_U(c,t)+C_V(c,t)*C_V(c,t)+C_W(c,t)*C_W(c,t));

real k = C_K(c,t);

real e = C_D(c,t);

real rho = C_R(c,t);

C_CENTROID(x,c,t);

{ znorm = x[2]/h;

if (znorm>0 && znorm<=0.22)

```c
{LAD=0; }
if ( znorm>0.22 && znorm<=0.33)
{LAD=0.17; }
if ( znorm>0.33 && znorm<=0.44)
{LAD=0.30; }
if ( znorm>0.44 && znorm<=0.55)
{LAD=0.52; }
if ( znorm>0.55 && znorm<=0.66)
{LAD=0.87; }
if ( znorm>0.66 && znorm<=0.77)
{LAD=1.27; }
if ( znorm>0.77 && znorm<=.88)
{LAD=1.28; }
if ( znorm>.88 && znorm<=.99)
{LAD=0.03; }
if ( znorm>.99)
{LAD=0; }
source = -1*lambda*LAD*rho*VEL*U;
dS[eqn] = -1*lambda*LAD*rho*(U*U/VEL + VEL);}
return source;}
DEFINE_SOURCE(y_mom_source,c,t,dS,eqn)
{ real x[ND_ND];
real source, LAD;
real znorm;
real U = C_U(c,t);
real V = C_V(c,t);
real W = C_W(c,t);
real VEL = sqrt(C_U(c,t)*C_U(c,t)+C_V(c,t)*C_V(c,t)+C_W(c,t)*C_W(c,t));
real k = C_K(c,t);
real e = C_D(c,t);
real rho = C_R(c,t);
C_CENTROID(x,c,t);
```

```
{ znorm = x[2]/h;
if ( znorm>0 && znorm<=0.22)
{LAD=0; }
if ( znorm>0.22 && znorm<=0.33)
{LAD=0.17; }
if ( znorm>0.33 && znorm<=0.44)
{LAD=0.30; }
if ( znorm>0.44 && znorm<=0.55)
{LAD=0.52; }
if ( znorm>0.55 && znorm<=0.66)
{LAD=0.87; }
if ( znorm>0.66 && znorm<=0.77)
{LAD=1.27; }
if ( znorm>0.77 && znorm<=.88)
{LAD=1.28; }
if ( znorm>.88 && znorm<=.99)
{LAD=0.03; }
if ( znorm>.99)
{LAD=0; }
source = -1*lambda*LAD*rho*VEL*V;
dS[eqn] = -1*lambda*LAD*rho*(V*V/VEL + VEL);}
return source;}}
DEFINE_SOURCE(z_mom_source,c,t,dS,eqn)
{real x[ND_ND];
real source, LAD;
real znorm;
real U = C_U(c,t);
real V = C_V(c,t);
real W = C_W(c,t);
real VEL = sqrt(C_U(c,t)*C_U(c,t)+C_V(c,t)*C_V(c,t)+C_W(c,t)*C_W(c,t));
real k = C_K(c,t);
real e = C_D(c,t);
```

```
real rho = C_R(c,t);

C_CENTROID(x,c,t);

{ znorm = x[2]/h;

if ( znorm>0 && znorm<=0.22)

{LAD=0; }

if ( znorm>0.22 && znorm<=0.33)

{LAD=0.17; }

if ( znorm>0.33 && znorm<=0.44)

{LAD=0.30; }

if ( znorm>0.44 && znorm<=0.55)

{LAD=0.52; }

if ( znorm>0.55 && znorm<=0.66)

{LAD=0.87; }

if ( znorm>0.66 && znorm<=0.77)

{LAD=1.27; }

if ( znorm>0.77 && znorm<=.88)

{LAD=1.28; }

if ( znorm>.88 && znorm<=.99)

{LAD=0.03; }

if ( znorm>.99)

{LAD=0; }

source = -1*lambda*LAD*rho*VEL*W;

dS[eqn] = -1*lambda*LAD*rho*(W*W/VEL + VEL);}

return source;}
```

Source Term for Kinetic Energy

```
DEFINE_SOURCE(tkecrown_source,c,t,dS,eqn)

{real x[ND_ND];

real source, LAD;

real znorm;

real U = C_U(c,t);

real V = C_V(c,t);

real W = C_W(c,t);
```

```
real VEL = sqrt(C_U(c,t)*C_U(c,t)+C_V(c,t)*C_V(c,t)+C_W(c,t)*C_W(c,t));

real k = C_K(c,t);

real e = C_D(c,t);

real rho = C_R(c,t);

C_CENTROID(x,c,t);

{ znorm = x[2]/h;

if ( znorm>0 && znorm<=0.22)

{LAD=0; }

if ( znorm>0.22 && znorm<=0.33)

{LAD=0.17; }

if ( znorm>0.33 && znorm<=0.44)

{LAD=0.30; }

if ( znorm>0.44 && znorm<=0.55)

{LAD=0.52; }

if ( znorm>0.55 && znorm<=0.66)

{LAD=0.87; }

if ( znorm>0.66 && znorm<=0.77)

{LAD=1.27; }

if ( znorm>0.77 && znorm<=.88)

{LAD=1.28; }

if ( znorm>.88 && znorm<=.99)

{LAD=0.03;}

if ( znorm>.99)

{LAD=0; }

source = lambda*LAD*rho*(A1*pow(VEL,3) - A2*VEL*k);

dS[eqn] = lambda*LAD*rho*(- A2*VEL); /* derivative for tke */}

return source;}
```

Source Term for Dissipation Rate

```
DEFINE_SOURCE (eps_source,c,t,dS,eqn)

{real x[ND_ND];

real source, LAD;

real znorm;
```

```
real U = C_U(c,t);
real V = C_V(c,t);
real W = C_W(c,t);
real VEL = sqrt(C_U(c,t)*C_U(c,t)+C_V(c,t)*C_V(c,t)+C_W(c,t)*C_W(c,t));
real k = C_K(c,t);
real e = C_D(c,t);
real rho = C_R(c,t);
C_CENTROID(x,c,t);
{ znorm = x[2]/h;
if ( znorm>0 && znorm<=0.22)
{LAD=0; }
if ( znorm>0.22 && znorm<=0.33)
{LAD=0.17; }
if ( znorm>0.33 && znorm<=0.44)
{LAD=0.30; }
if ( znorm>0.44 && znorm<=0.55)
{LAD=0.52; }
if ( znorm>0.55 && znorm<=0.66)
{LAD=0.87; }
if ( znorm>0.66 && znorm<=0.77)
{LAD=1.27; }
if ( znorm>0.77 && znorm<=.88)
{LAD=1.28; }
if ( znorm>.88 && znorm<=.99)
{LAD=0.03; }
if ( znorm>.99)
{LAD=0; }
source = lambda*LAD*rho*(A3*A1*e/k*pow(VEL,3) - A4*A2*VEL*e);
dS[eqn] = lambda*LAD*rho*(A3*A1/k*pow(VEL,3) - A4*A2*VEL); /* derivative
for eps */}
return source;}
```

Vegetation Enegy Source

```
DEFINE_SOURCE (cooling,c,t,dS,eqn)

{real x[ND_ND];

real YTL, source;

real TL = C_T(c,t);

C_CENTROID(x,c,t); /* store cell center coordinates in vector x : x[0]=x , x[1]=y */

YTL=-2.226+0.108*TL; //*TL is leaf temp equivalent to canopy cell temp*/

{ source = -750.0*YTL;

dS[eqn] = 0;}

return source;}
```

Vegetation Humidity Source

```
DEFINE_SOURCE (water_source,c,t,dS,eqn)

{real x[ND_ND];

real source, LAD, znorm;

C_CENTROID(x,c,t); /* store cell center coordinates in vector x : x[0]=x , x[1]=y */

{ znorm = x[2]/h;

if ( znorm>0 && znorm<=0.22)

{LAD=0; }

if ( znorm>0.22 && znorm<=0.33)

{LAD=0.17; }

if ( znorm>0.33 && znorm<=0.44)

{LAD=0.30; }

if ( znorm>0.44 && znorm<=0.55)

{LAD=0.52; }

if ( znorm>0.55 && znorm<=0.66)

{LAD=0.87; }

if ( znorm>0.66 && znorm<=0.77)

{LAD=1.27; }

if ( znorm>0.77 && znorm<=.88)

{LAD=1.28; }

if ( znorm>.88 && znorm<=.99)

{LAD=0.03; }

if ( znorm>.99)
```

```
{LAD=0; }
source = Rw*LAD;
dS[eqn] = 0;}
return source;}
```

User-Defined function for Steady Cooling power:

```
DEFINE_SOURCE(cooling,c,t,dS,eqn)
{real x[ND_ND];
real source;
C_CENTROID(x,c,t); /* store cell center coordinates in vector x : x[0]=x , x[1]=y */
{source = -750.0;
dS[eqn] = 0;}
return source;}
```

User-Defined function for Vegetation Energy Source

```
DEFINE_SOURCE(cooling,c,t,dS,eqn)
{real x[ND_ND];
real PC, ETP, ETeq, LAD, source;
real znorm;
real Rh = 875;
real lhv=2260;
real lhvinwh=8136000;
real rhowater=1000;
real TL = C_T(c,t);
C_CENTROID(x,c,t); /* store cell center coordinates in vector x : x[0]=x , x[1]=y */
ETeq=Rh/(lhv*rhowater);
ETP=(0.0252*C_T(c,t)-0.078)*ETeq;
PC=ETP*rhowater*lhvinwh*LAD;
{ znorm = x[2]/h;
if ( znorm>0 && znorm<=0.22)
{LAD=0; }
if ( znorm>0.22 && znorm<=0.33)
{LAD=0.17; }
if ( znorm>0.33 && znorm<=0.44)
```

{LAD=0.30; }

if (znorm>0.44 && znorm<=0.55)

{LAD=0.52; }

if (znorm>0.55 && znorm<=0.66)

{LAD=0.87; }

if (znorm>0.66 && znorm<=0.77)

{LAD=1.27; }

if (znorm>0.77 && znorm<=.88)

{LAD=1.28; }

if (znorm>.88 && znorm<=.99)

{LAD=0.03; }

if (znorm>.99)

{LAD=0; }

source = -PC;

dS[eqn] = 0;}

return source;}}

User-Defined Function for water heat flux

#include "udf.h"

#define I 177

real gamma = 0.1;

real wz=2.7;

real epsw =0.95;

real gammaa =0.03;

real eps=0.97;

real sigma =0.0000000567;

real Ta=34;

Water Energy Source

DEFINE_SOURCE(energy_source, c, t, dS, eqn)

{real x[ND_ND];

real s, a, b, fw, e, ce, ew;

real source;

real P = C_P(c,t);

```
real Tw = C_T(c,t);
C_CENTROID(x, c, t);
{ s=I*(1-gamma);
a=(1-gammaa)*eps*sigma*(273+Ta);
b=sigma*epsw*(273+Tw);
fw=9.2+0.46*wz*wz;
ew=6.1094*exp((17.625*Tw)/(Tw+243.04));
e=fw*(ew-P);
ce=0.47*fw*(Tw-Ta);
{source = -1*(s+a-b-e-c);
dS[eqn] = 0;}
return source;}}
```